Improving the Resolution of Prosthetic Vision through Stimulus Parameter Optimization

by

Dorsa Haji Ghaffari

A dissertation submitted in partial fulfillment
of the requirements for the degree of
Doctor of Philosophy
(Biomedical Engineering)
in the University of Michigan
2021

Doctoral Committee:

Professor James D. Weiland, Chair
Associate Professor Tim M. Bruns
Associate Professor Cynthia A. Chestek
Professor Bret A. Hughes

Dorsa Haji Ghaffari

ghdor@umich.edu

ORCID iD: 0000-0002-9600-5628

Dedication

This dissertation is dedicated to my grandfather, Babaji. You have always inspired me by your intelligence, kindness, and love for knowledge. Thank you for always being there and encouraging me to never stop achieving more. I love you.

Acknowledgements

Thank you to my family for always being my rock. I want to thank my mom, dad, Mozhan, Omid, Mamahin, Babaji, Mehran, Marieh, Kati, and aunt Monir. You have given me unconditional love and support, and have loved me for who I am since day one. Thinking about each one of you has given me hope and motivation when I struggled, no matter how far apart we are. You have been my role models and shaped me into who I am today. I am beyond thankful for having you, I love you, and can't wait to hug you.

Thank you to my adviser, Dr. James Weiland. You have been very generous with your knowledge and support, while giving me the freedom to explore different avenues. You have taught me great work ethic, independence, patience, and open-mindedness. You have always guided me in the right direction, while caring about my mental health and being extremely understanding of my personal life. I couldn't have imagined a better adviser and PhD experience. Thank you for everything you have done for me. I would also like to thank my committee members Dr. Tim Bruns, Dr. Cynthia Chestek, and Dr. Bret Hughes. You have kindly offered your expertise and constructive feedback, and have helped me navigate through my research.

Thank you to my lab mates Elena, Muru, Kate, Beomseo, Negin, Hojun, Wennan, Faranak, and Swetha. You guys have kept me sane with our lunch breaks, Coco trips, birthday celebrations, and game nights. Each one of you are uniquely special to me. I couldn't have asked for a better group to spend every day with. I will miss working alongside you and laughing with you.

Thank you to my best friends Kimia, Mahta, Niloufar, and Parmiss. You have always been a big part of my life since childhood. You have made me laugh and listened to me when I cried. It warms my heart to think about our memories and the ever growing connections we have.

Thank you to my best friends in Michigan. Mahmood, Natalie, Soroush, Elissa, Hans, Richard, Daniella, Evran, Hisham, and Pouyan. You have been my second family here. Thank you for your unconditional support, kindness, and encouragement. I'm grateful for our friendships and I look forward to making more memories together.

Table of Contents

List of Tables

List of Figures

Abstract

Retinal prostheses have helped improve vision in patients blinded by photoreceptor degeneration. These electronic implants operate by electrically stimulating the remaining retinal cells. While retinal prosthesis users report improvements in light perception and performing basic visual tasks, their ability to perceive shapes and letters remains limited. Investigating stimulation strategies to reduce perceptual thresholds and create focal, non-overlapping phosphenes will increase the resolution of retinal prostheses and improve the overall patient outcomes. In this thesis I explore two main strategies for electrode-specific optimization of stimulation parameters: 1) a novel pulse paradigm for threshold reduction, and 2) an automated closed-loop method for adjusting stimulation parameters to create a focal retinal activation area.

I combined human subject testing and computational modeling to investigate the effect of waveform asymmetry on perception shapes and thresholds with epiretinal stimulation. Threshold measurement and phosphene shape analysis was performed on four Argus II users. A computational model of a retinal ganglion cell (RGC) was created in the NEURON simulation environment to allow for a more thorough parameter testing and to gain insight into the biophysical mechanisms. Our human subject results suggest that asymmetric waveforms could increase perception probabilities compared to a standard symmetric pulse, and this effect can be intensified by addition of an interphase gap (IPG). Our computational model predicts that the most effective pulse for threshold reduction is asymmetric anodic-first stimulation with small duration ratios ($\leq$ 5) and long IPGs ($\geq$ 2 ms). Phosphene shape analysis revealed no significant difference in percept

elongation with different pulse types. Average phosphene area was larger with asymmetric anodic-first stimulation compared to other pulse types.

Prosthetic vision quality is highly dependent on the capability to precisely activate target neurons and avoid off-target activation. However, studies show elongated and inconsistent responses to single electrode stimulation, indicating unintended stimulation of off-target neurons and electrode-specific activation patterns. While tuning stimulation parameters can transform the spatial RGC activity, a manual search for optimal parameters can be time consuming and tiring for patients. I developed a process for automatic optimization of stimulation parameters *in silico*, which involved training neural networks for quantifying the relationship between pulse parameters and spatial response descriptors, and a closed-loop algorithm to search for optimal parameters. Using this process, I was able to guide the parameter search effectively and converge to an optimal response within a few iterations.

Finally, I presented a process for automatic optimization of stimulation parameters *in vitro* using calcium imaging in mouse retina. This process involved training neural networks at each iteration based on a few images, using an interior point algorithm to find the optimal parameters, and classifying the resulting calcium images with a CNN trained on previous data. Our results indicate that we can converge to optimal stimulation parameters that create focal RGC activity by sampling less than 1/3 of the parameter space. This approach can shorten the exploration time significantly compared to a manual search, especially when the parameter space is large. Findings of this project could lead to the development of a clinically applicable system for electrode-specific optimization of stimulation protocol, improving the overall outcome of artificial vision.

Chapter 1 : Introduction

1.1. Retina

Vision is the most important and complex human sense. Major parts of the visual system include the eye, optic nerve, lateral geniculate nucleus, and primary visual cortex. The eye is the first component of this system (Fig. 1.1). Light passes through the cornea, lens, and vitreous humor to eventually form an image on the retina. The retina is a 200 μm thick structure that lines the back of the eye [1]. Light passes through the inner layers of the retina, reaches the photoreceptor layer and through a process called phototransduction is transformed to electrical signals. These neural signals then travel from the outer layers towards the inner layers of the retina and are modified before reaching the ganglion cells. Different layers of the retina from outer to inner include: retinal pigment epithelium (RPE) layer, photoreceptor layer, outer nuclear layer (ONL), outer plexiform layer (OPL), inner nuclear layer (INL), inner plexiform layer (IPL), retinal ganglion cell layer (GCL), and nerve fiber layer (Fig. 1.1). RPE absorbs the scattered light for a better image quality and to reduce the photo-oxidative effect on cells. It also provides metabolic support to the photoreceptors and is involved in phagocytosis of photoreceptor outer segments. The photoreceptor layer consists of the outer segments of two main types of cells: rods and cones. Rods operate at dim light conditions and are responsible for night vision. The human retina contains 92 million rods distributed mainly outside of the foveal region [2]. Cones are responsible for color vision in day light conditions. There are roughly 4.6 million cones in human retina, with the highest density in the foveal region. There are three types of cones in the primate retina: blue, green, and red cones which detect short, medium, and long wavelengths respectively. The ONL consists of

the cell bodies of rods and cones. The OPL is where rods and cones form synapses with bipolar cells and horizontal cells. The INL contains the cells bodies of bipolar, horizontal, and amacrine cells. The IPL contains synapses between bipolar, amacrine and RGCs. The GCL contains the cell bodies of ganglion cells (and displaced amacrine cells) and finally the nerve fiber layer consists of the RGC axons that travel towards the optic disc and carry information to the rest of the brain.

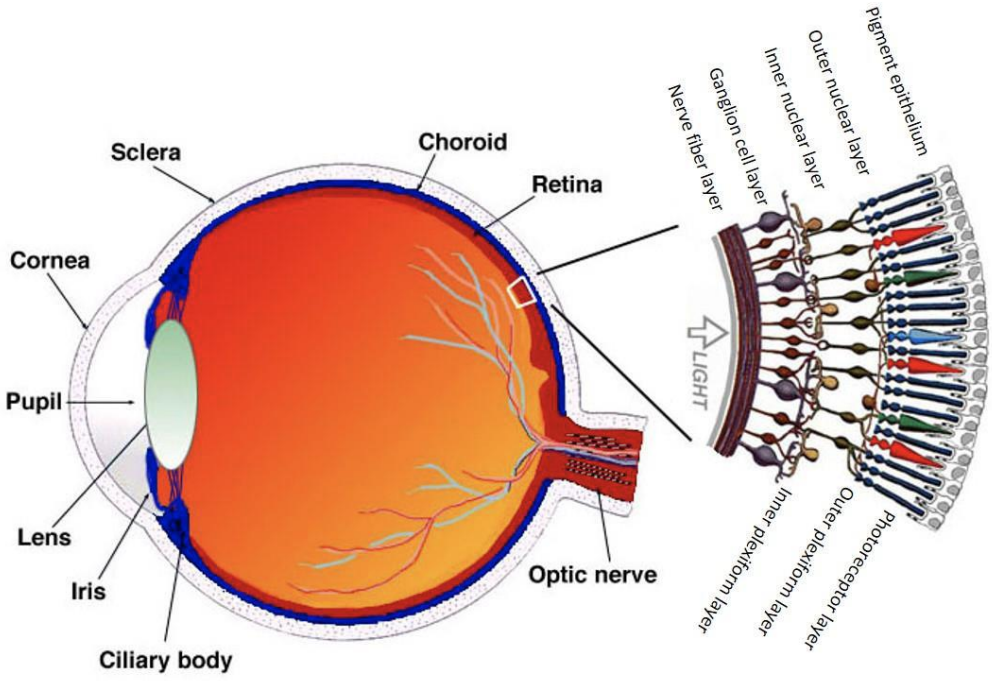

Figure 1. 1. Cross section of the human eye and retina. Light travels through the cornea, pupil and lens and is focused on the retina. Through phototransduction, light is converted into electrical signals which pass through layers of the retina for pre-processing and eventually get to retinal ganglion cells. The neural signals then travel to the brain through the nerve fiber layer and optic nerve. Image courtesy of http://webvision.med.utah.edu/.

1.2. **Retinal Degenerative Diseases**

In 2020 an estimated 49.1 million people were blind globally [3]. Photoreceptor degeneration is a major cause of vision loss. Retinitis pigmentosa (RP) and age-related macular degeneration (AMD) are two of the common retinal degenerative diseases that lead to loss of photoreceptor cells and eventual blindness [4], [5]. RP is progressive over many years. It causes

degeneration of rod photoreceptors in the periphery and tunnel vision in the early stages. In later stages, degeneration can progress to the central retina, affecting cones and the retinal pigment epithelium (RPE) , ultimately resulting in complete blindness. RP is estimated to affect 1.5 million people around the world, or 1 in 4,000 people in the United States and worldwide [6]. RP is a collective term used to describe inherited disorders with similar symptoms, but varying severity. Over 4000 distinct mutations in more than 70 genes can individually cause RP [7].

AMD primarily affects the macula, causing degeneration of mainly cone photoreceptors and central vision loss. The affected area can grow larger as the disease progresses. AMD is the main cause of vision loss in people 50 and older, and affected 196 million people worldwide in 2020. This number is expected to grow to 288 million by 2040 [8]. The exact cause of AMD is not known but it is linked to a number of risk factors including smoking, family history of the disease, high blood pressure, and age. Figure 1.2 demonstrates examples of vision loss for RP and AMD.

Figure 1. 2. Vision loss pattern with RP and AMD. *Left:* normal sight. *Middle*: peripheral vision loss with RP. *Right:* central vision loss with AMD. Image courtesy of https://www.nei.nih.gov/

1.2.1. Retinal degeneration therapies

RP is characterized by progressive degeneration and dysfunction of the retina, mainly photoreceptors and RPE. Although there is no cure for RP, there are treatments that can possibly manage the progression of the disease or control the symptoms [9]. Vitamin and supplement therapy is advantageous to a limited group of RP patients. A study has shown that patients who

were taking vitamins A and E had a slower decline in their electroretinogram (ERG) measurements [10]. However, dietary modification is the definitive treatment for only three rare forms of RP [11], [12]. Gene therapy has shown some progress in treating RP patients with mutations in the *RPE65* gene. In this method, a normal *RPE65* gene is delivered in the subretinal space by intraocular injection. In 2017, FDA approved the first gene therapy that uses an adeno-associated virus (AAV) that targets *RPE65,* which has successfully improved functional vision in the recipients [13]. Stem cell transplantation is another possible therapy for RP. Transplanted cells can substitute the degenerated cells, or release growth factors to improve cell growth, survival, and function. There is an ongoing clinical trial to test the safety of transplanting fetal retinal tissue and retinal pigment epithelium in patients with RP. Optogenetic therapy is another potential treatment for RP, aiming to induce light sensitivity to the remaining retinal cells by delivering a light-sensitive opsin protein [14], [15]. A major barrier to optogenetic therapies is the lack of evidence for sufficient gene expression in non-human primate and degenerated human retina [16].

AMD is an acquired disease of the macula characterized by neurodegeneration of the photoreceptors and retinal pigment epithelium. The presence of drusen – focal accumulation of yellow extracellular material beneath the RPE derived from incompletely digested fats and proteins – is the hallmark sign of AMD. Treatments for wet AMD or choroidal neovascularization (CNV) include photodynamic therapy (PDT) and anti-VEGF treatment [17], [18]. Dry AMD has no approved treatment currently. A study assessed the effectiveness of monthly intravitreal injection of lampalizumab for halting the progress of geographic atrophy (GA) in dry AMD patients [19], but the results showed that this drug was ineffective in treating GA [20].

Electronic retinal prostheses have been effective in improving vision for patients blinded by photoreceptor degeneration, and are discussed in more detail in the next section.

1.3. **Retinal Prostheses**

Retinal prosthetic implants have helped partially restore vision in patients blinded by photoreceptor degeneration through electrically stimulating the surviving cells in the inner retina [21][22][23]. In epi-retinal implants the visual information is gathered by a video camera,

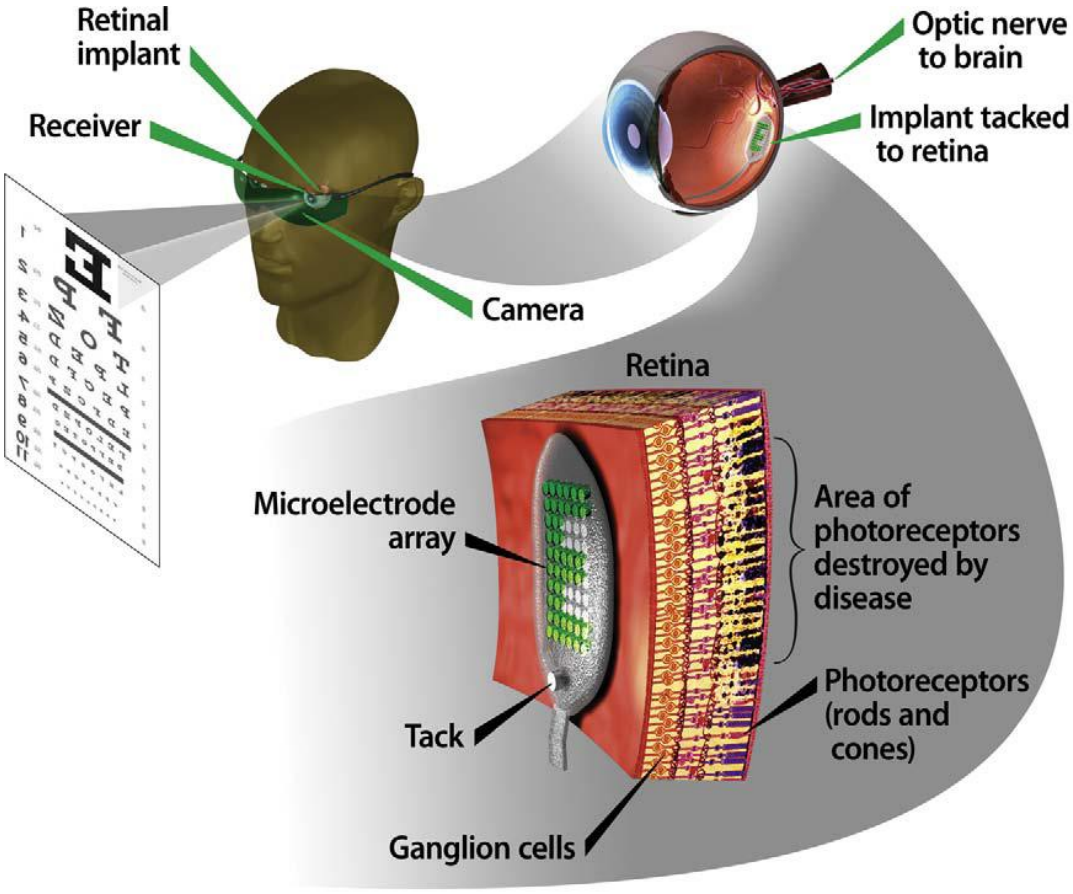

Figure 1. 3. Epiretinal prosthesis components. The camera gathers visual information and sends them to VPU for processing and transforming into electrical stimulation. Electrical signals are delivered to the MEA implanted on the retina, through external and implanted coils. (adapted from Chader et. al. 2009)

transformed into electrical stimulation through a video processing unit (VPU), external and implanted coils, and delivered to a microelectrode array (MEA) implanted on the retinal ganglion cell (RGC) side of the retina. Three main types of retinal implants, named according to the position of implantation, are epiretinal, placed on the inner surface (RGC side) of the retina, subretinal,

placed on the outer surface (photoreceptor side) of the retina, and suprachoroidal, placed between sclera and choroid [24].

1.3.1. Epiretinal prostheses

In epiretinal implants, the electrode array is positioned on the innermost layer of the retina. An advantage of epiretinal implants is familiarity of the surgery routine and lower risk of retinal detachment. Moreover, the fluid inside the vitreous cavity can help with heat dissipation (from electrical stimulation) and lower the thermal risks to the retina [25]. The close proximity of electrodes to the RGCs makes them the main target of direct stimulation. A disadvantage of this setting is that the nerve fiber layer is between the RGCs and electrodes in epiretinal stimulation, resulting in axonal stimulation and antidromic activation of off-target neurons. This can lead to perception of elongated percepts and a lower image resolution. However axonal activity can possibly be avoided by modifying stimulation parameters [26], [27]. Groups that have tested epiretinal implants in patients include Second Sight Medical Products (SSMP) Inc. (Sylmar, California USA), Intelligent Medical Implants (acquired by Pixium Vision, Paris, France), and EpiRet GmbH (Germany).

Argus I and II devices have been developed by SSMP, both consisting of the elements mentioned above. Argus I contains 16 electrodes of 260 μm and 520 μm diameter, and Argus II contains 60 electrodes of 200 μm diameter. Argus I was implanted in 6 subjects blinded by RP [28], [29]. All implant users reported light perception and the ability to perform visual tasks such as detecting and counting objects [30]. Argus II has a higher electrode density, increasing the theoretical resolution, and also covers a wider visual angle compared to Argus I (11°×19° vs. 10°×10°). Over 300 patients have been implanted with Argus II worldwide. The best reported visual acuity was improved from 20/ 3244 for Argus I to 20/ 1260 for Argus II [31], [32].

The Intelligent Medical Implants' (IMI) device has similar components as the Argus implant, with a difference in wireless transmission. The IMI implant uses two wireless links, an RF transmission for power and an infrared (IR) transmission for data [33]. The IR transmitter is positioned in front of the eye and the IR receiver is implanted inside the eye, as part of the implant. This prototype contained 49 iridium oxide electrodes. Data transmission is interrupted by closing the eyes, mimicking the response in normally sighted people. 19 out of 20 subjects with advanced RP tested with the IMI implant reported light perception, and were able to distinguish between two phosphenes elicited by adjacent electrodes and recognize simple shapes [34]. Pixium Vision has further refined the implant after acquiring IMI. Their Intelligent Retinal Implant System (IRIS) II contains 150 electrodes and a glass-mounted visual interface. This device uses a neuromorphic image sensor that detects the coordinates and light intensities of changing pixels. A unique feature of this implant is a learning retinal encoder, which calibrates individual pixels and assigns them as excitatory or inhibitory, mimicking the ON/OFF pathways in the retina [35], [36]. Clinical trials in 10 subjects over 6 months demonstrated improvements in square localization, picture recognition, and direction of motion tasks.

The EPI-RET3 implant from EpiRet GmbH differs from Argus and IRIS implants in that the internal components are entirely intraocular, eliminating the need for a transscleral cable and reducing the risk of complications. The external components include a video camera and visual processing unit which wirelessly transmits visual information to the internal components inside the eye [37]. The device allows for bidirectional stimulation and recording with microelectrodes, using ultrahigh-frequency-pulsed charge-controlled stimulation. This provides the possibility to modify stimulation protocols to deliver a more efficient stimulation based on the intrinsic activity of retinal neurons [38]. For clinical trials, 6 subjects were implanted with a basic 25 electrode

system. All patients reported pattern phosphenes with low stimulation thresholds, however, phosphene characteristics varied greatly between subjects [39].

1.3.2. Subretinal prostheses

Subretinal implants are positioned between sensory retina and the RPE, in the location where photoreceptors existed prior to degeneration. One rationale behind this placement is taking advantage of the signal processing capacity of inner retinal neurons to provide a more physiologically realistic form of vision. In addition, the implant is sitting closer to the target neurons (bipolar cells), requiring lower stimulation currents to elicit a response. However, the anatomical reorganization and degeneration of retinal interneurons can raise the stimulation thresholds [40], [41]. The surgical procedure for subretinal implants can be technically more challenging because of the adhesion of RPE to retina, and that surgeons are less familiar with this type of procedure. Leading groups that have focused on subretinal implants include the Boston Retinal Implant Project (BRIP), Optobionics (Naperville, IL, USA), Retina Implant AG (Reutlingen, Germany), and Pixium Vision.

The BRIP implant is similar in design to Argus II, but it is implanted subretinally. This group is performing pre-clinical trials for a 256 channel device. A unique feature of this device compared to other subretinal implants is the high count 256 ceramic feedthroughs in a titanium case. This can support a lifetime of 5-10 years in physiological environments [42], [43].

The Artificial Silicon Retina (ASR) developed by Optobionics was designed to use ambient light for retinal stimulation. The array is 2 mm wide, 25 μm thick, consisting of 5000 microphotodiodes associated with 9 μm diameter iridium microelectrodes and functions passively with no external power [44]. A total of 10 patients were implanted with the ASR. This device demonstrated good longevity and safety and a temporary improvement in visual function [45].

However, this improvement was attributed to the neurotrophic effect of the implant on the retina, and it was concluded that ambient light is unable to create sufficient photocurrent to stimulate an adequate population of neurons [44], [46], [47], [48].

The Alpha IMS implant developed by Retina Implant AG (Reutlingen, Germany), is the only subretinal implant that obtained CE marking (similar to FDA approval). This system uses a multiphotodiode array (MPDA) containing 1500 units, with each unit having a combined photodiode amplifier electrode. It differs from ASR is that it uses an external power source to amplify the signal. 21% of implanted subjects reported very good improvements, recognizing unknown objects and letters, and 28% reported no benefit in daily life. 86% of subjects reported light perception and significant improvement in light localization. The best reported visual acuity was 20/546 on contrast-reversal Landolt C-ring testing. Object recognition significantly improved within the first 3 months of the trial and fell below significance after 6 months [49], [50]. Alpha AMS was the new generation of this implant with 1600 photodiodes and they have reported substantial improvement in its functional longevity [51]. Retina Implant AG was shut down in 2019.

The Photovoltaic Retinal Implant (PRIMA) produced by Pixium Vision uses a novel method for photovoltaic stimulation. The implant is a hexagonal chip consisting of 378 pixels with 30 μm thickness and 2 mm width, inserted subretinally [52]. A near-infrared light source on the glasses sends visual information to each pixel and this photic energy is converted into electrical current that polarizes nearby neurons. Their preclinical results in animal models showed that the amplitude of the visual evoked potential (VEP) can be modulated by modifying the light intensity or pulse duration [53]. They also showed that by switching from cathodic-first to anodic-first pulses, the electrical stimulation thresholds can be reduced to a level that allow IR irradiance well

below the ocular safety limit while maintaining the spatial frequency [54]–[56]. Clinical trials for this device in 5 patients with atrophic age-related macular degeneration showed that all participants could perceive visual patterns with adjustable brightness. 3 subjects with optimal placement of the implant reported visual acuities between 20/460 and 20/550, which was 10% to 30% less than the expected acuity based on the electrode pitch [52].

1.3.3. Suprachoroidal prostheses

Suprachoroidal implants are placed between the choroid and sclera. The separation between the electrode and retina reduces the risks of retinal damage from surgery. In addition, the blood vessels in the choroid layer can dissipate the heat generated from stimulation [57], [58]. However, the increased distance leads to increased perceptual thresholds (higher current amplitudes needed for stimulation) and lower spatial resolution [59]. Main groups focusing on suprachoroidal implants area Bionic Vision Australia (BVA) and Japan's Artificial Vision Project.

The first prototype from the BVA group was a 24-channel containing 20 stimulating and 4 return electrodes. Three subjects with advanced RP were implanted in 2012, all of which developed subretinal and suprachoroidal hemorrhage after the operation [60]. All patients reported phosphene perception, but they were variable in thresholds, character, and location [61], [62]. Light localization was better than chance in all subjects. Only one subject completed the visual acuity task and averaged 20/8397, which was significantly better than the visual acuity with the device off. In all cases, a fibrous tissue capsule was developed around the implant after explantation [63]. The BVA group is developing a 44-channel device, and a 99-channel (Phoenix-99) device with quasi-monopolar stimulation patterns [64], [65].

The suprachoroidal-transretinal stimulation (STS) device is being developed by the Artificial Vision Project in collaboration with NIDEK. Unlike other implants, the STS implant is

a 3D, 49 microelectrode array, with electrodes protruding from the array by 0.3 mm. Visual information is gathered by the camera on the glasses and processed by a computer on within the glasses arm. The external coil relays signal via the secondary coil to the decoder which creates a biphasic pulse. In a pilot study involving 2 patients with 9 electrode implants, phosphenes were elicited and both patients were able to identify and discriminate between objects with head scanning. One patient was able to detect motion and complete grasping tasks better than by chance [66]. Both subjects were able to walk along a white line and recognize everyday objects better than by chance, but this was not reproducible at every follow up visit [67]. Results demonstrated that subjects detected objects more accurately using artificial vision and residual natural vision together compared to only natural vision [68]. Overall, there are greater limitations to the suprachoroidal approach compared to epiretinal and subretinal approaches, however, a greater number of subjects are required to draw a conclusion.

1.4. **Clinical findings with Argus II prosthesis**

My dissertation involved testing patients who received the Argus II implant, thus a description of the history of this device is provided. The Argus II retinal prosthesis system (Second Sight Medical Products, Sylmar, CA, USA) is an epiretinal implant approved for use in the European Union and the United States [69]. This device has three internal and three external components. Internal components include a coil and electronics case sutured to the sclera (outside the eye), a ribbon cable connecting the electronics case and the array, and an epiretinal microelectrode array consisting of 60 electrodes with 200 μm diameter and 520 μm pitch. The external components include a video camera mounted on a pair of glasses, a visual processing unit (VPU), and a coil for transmitting data wirelessly to the internal coil.

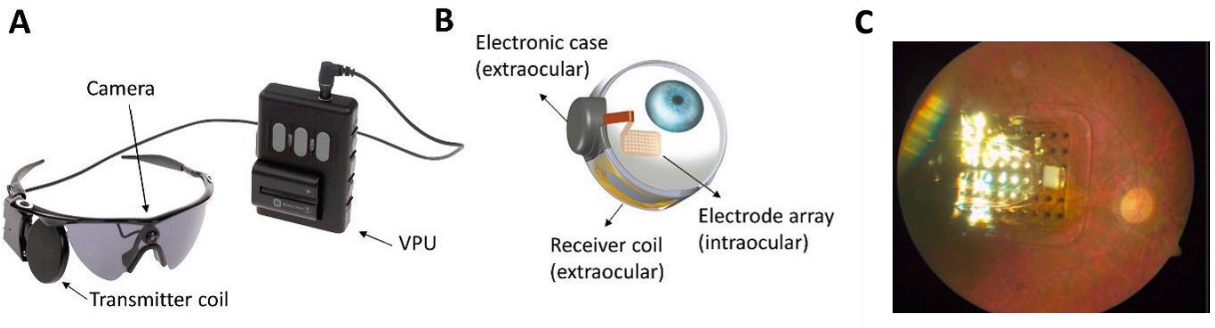

Figure 1. 4. Components of the Argus II retinal prosthesis. A) external components including the video camera, external coil, and VPU. B) internal components including the receiver coil and electronic case, ribbon cable, and microelectrode array. C) fundus image of a subject with Argus II implant.

Results from the initial acute experiments on human participants showed that perception thresholds in the macular region were lower than the extramacular regions, suggesting that arrays should be placed on the macular region [70]. Initial chronic studies (with Argus I) on 6 participants using a biphasic pulse showed that thresholds increase with the electrode-retina distance , but they do not change with electrode size (260 and 520 μm) [29], [71]. Single electrode experiments have demonstrated that phosphene brightness and thresholds can be controlled by modifying parameters such as pulse duration, amplitude, and frequency [72]. Clinical studies have shown that single electrode stimulation can lead to perception of elongated phosphenes in epiretinal implant users [73], [74]. Unintended activation of off-target RGCs due to stimulation of axons of passage [26], [27] is identified as an important contributing factor to elongated responses and therefore lower resolution of the perceived image. A study on Argus II implant users showed 86% and 73% improvements in door finding and line tracking tasks respectively after 6 months of implantation compared to when the device is turned off [75], suggesting that some functional vision is provided through the implant. In another study participants were able to point to a bright square on a dark background [32]. In addition, participants have been able to discriminate letters on a monitor by head scanning [76]. However, patients with implants who can recognize letters take an average of

more than 40 seconds to do so [77]. These results show that although shape and letter perception with retinal prosthesis is possible, forming high resolution meaningful images and efficient shape detection in a way that is similar to natural vision is still uncertain [78].

1.5. **Current Limitations of Retinal Prostheses**

The efficacy of neural stimulation is highly dependent on the capability to precisely activate the target neuronal population, while avoiding stimulation of the off-target populations. *In vitro* studies have demonstrated that electrical stimulation of the retina results in activation of the off-target ganglion cells [79][27], where off-target is defined as RGCs whose cell bodies are not near the electrode.

Clinical studies have also shown limitations in shape perception abilities of patients with retinal implants, confirming the in vitro results with respect to activation of RGCs outside the region of interest [77][80][73]. Off-target stimulation can result from a number of factors including unintended axonal activation [27][81], large size and low density of electrodes, electrode-retina distance which results in current spread [82][83][71], and spatiotemporal interactions between electrodes [84]. However, a computational study using rectangular electrodes with 10 μm diameter showed that a 50 μm electrode-retina seperation results in a more focal response compared to zero separation [85]. Desensitization of RGCs to repetitive stimulation is another factor that limits shape perception abilities of retinal implant users [86][87]. Studies have shown that a single electrode activation results in perception of streak-shaped responses in patients [88][73], which decreases the overall resolution of the implant. Stimulation of axon fibers passing under the electrode antidromically activates cell bodies and leads to elongated phosphenes [89]. In addition, phosphene shapes can be highly variable across electrodes and subjects (Fig. 1.5). Furthermore, activation of multiple electrodes along the same axonal tract does not result in two distinct

Figure 1. 5. Phosphene drawings for three subjects. Phosphene shapes are drawn for each active electrode (red circles). Blue squares mark the approximate location of fovea. (Nanduri 2011, Thesis)

phosphenes, which can greatly hinder the image resolution. A study has demonstrated improvement in avoiding axonal activation using sinusoidal stimulation as it causes a larger gap between soma and axon thresholds [90]. Our group has shown that focal activation can be attained with longer pulses (> 25 ms) through stimulation of bipolar cells [27]. Another study has demonstrated the possibility of avoiding axonal activation using very short (< 500 us) anodic-first biphasic pulses [79]; however, the threshold charge densities for long pulses are generally above the Argus II safety limits for both chronic and acute stimulation. Very short pulses are efficient with respect to charge, but they use high current amplitudes which generates a high voltage that might go beyond the capacity of the stimulator.

Another major problem with current retinal implants is the variable perception threshold both across different patients and with individual electrodes in the same patient. Multiple factors contribute to this variability including the morphological and functional differences between RGCs [1][91][92], non-uniform separation between electrodes and the retina [93][94], variations in blindness severity [95][96], and density and health of the surviving retinal neurons. Argus II stimulates with symmetric biphasic cathodic-first pulses. The cathodic phase causes a depolarization in cells to generate spikes, and the second phase balances the charge to reverse electrochemical reactions. Platinum gray coating on the electrodes has a charge injection safety

limit of 1 mC/ cm^2 and 0.35 mC/ cm^2 for acute and chronic stimulation respectively [97][88]. These limits are set by regulatory agencies and are based on historical studies of neural stimulation, which have determined the allowed amount of charge per phase without producing irreversible damage to the electrode and the tissue [98]. However, a clinical trial reported that among 30 patients with retinal prostheses, about half of the electrodes had activation thresholds above the acute stimulation safety limit [99]. Even with a direct contact between the macula and electrodes, an average of 10% of electrodes have thresholds above the acute stimulation safety limit [97][88]. As a result, it is critical to investigate stimulation parameters that lower activation thresholds as it provides a wider range of stimulus intensities to work with in retinal implants [100] and decreases charge and power consumption [100][101].

1.6. **Electrical Stimulation of the Retina**

Electrical stimulation of retina *in vitro* and *in vivo* in animal models can provide valuable information about the mechanisms of retinal activation. Clinical trials of retinal stimulation have provided mostly qualitative knowledge of retinal activation such as the shape, brightness, and size of phosphenes. Experiments with retinal implant users can also offer information on the current thresholds for inducing phosphenes. However, perceiving phosphenes is subject to inaccuracies such as background retinal activity, and residual retinal response to light in the environment. In addition, phosphene shapes and thresholds are highly variable across electrodes and patients [74], [102]. Non-uniform retinal degeneration [103], [104], disease stage, and variable separation between the electrodes and retina are some of the contributing factors to this variability [88], [105]. Therefore, to better understand and quantify retinal activity in response to electrical stimulation, it's critical to perform in vitro and in vivo studies. Biophysical modeling of the retina has also

provided important information on the mechanisms of retinal activation, however, these models are generally simplified and do not capture the complexity of retinal circuits [106]–[108].

1.6.1. Retinal ganglion cell response to electrical stimulation

Retinal ganglion cells (RGC) are the inner most layer of the retina, whose axons form the optic nerve and travel to the visual processing centers in the brain. RGCs collect electrical signals from bipolar cells and amacrine cells. These visual information is integrated in RGC dendrites and cell body, and digitized into action potentials. Ganglion cell axons terminate in the lateral geniculate nucleus and superior colliculus [109], [110]. RGC responses to electrical stimulation can be classified as direct and indirect, based on the origin of activation. Direct activation happens when RGCs spike directly in response to stimulation. A common feature of direct RGC activation is the short latency of elicited spike, usually within 5 ms of the stimulus onset [111]–[113], [100]. Both subretinal and epiretinal stimulation can result in direct RGC activation. Direct activation is thought to initiate in the sodium channel band near the axon hillock [114]–[116]. Indirect RGC activation occurs when inner retinal neurons respond to electrical stimulation first and subsequently activate RGCs via synaptic activity. Spike latency for indirect activation is longer than direct activation, peaking tens of milliseconds after the onset of stimulation [117], but indirect responses are generally not time-locked to the stimulus [118], [119], unlike direct responses. Indirect responses are typically paired with short-latency (direct) RGC spikes, indicating that direct and network activation can occur simultaneously. Recording methods including patch clamping, microelectrode recording, and calcium imaging can provide valuable information on the temporal and spatial properties of RGC response to electrical stimulation.

1.7. **Calcium imaging**

Calcium imaging is an optical method for measuring neuronal activity. The amount of intracellular calcium is an indirect measure of neural spiking. When a neuron fires, the membrane depolarization results in an influx of Ca^{2+} ions through ion channels on the membrane into the cell. Measuring this change in Ca^{2+} thus provides a tool for recording neuronal activity. Calcium dynamics within the neurons are generally slower than spiking rate, limiting the temporal resolution of calcium imaging [120], [121], [122], [123]. However, this method has proven effective in measuring spatial activity of RGCs. Calcium indicators include calcium dyes and genetically encoded calcium indicators (GECI). Oregon-Green BAPTA-1 and fluo-4 are two of the most prevalent calcium dyes with brightest indicators within visible wavelength. However, calcium dyes have several limitations such as leakage, compartmentalization, photobleaching, and lack of specificity.

1.7.1. Genetically encoded calcium indicators

GECIs overcome many of the limitations of synthetic dyes. Most GECIs contain one or two fluorescent molecules, a calcium binding domain, and a binding peptide. Cameleon was the first proposed GECI containing two GFP proteins with different emission wavelengths [124]. The first generation of cameleon has relatively low sensitivity of calcium for most applications [125]. Later generations of this indicator showed improved calcium sensitivity, however their performance lags behind the best synthetic dyes [126]. Development of GCaMP as a single wavelength sensor was a major breakthrough of calcium indicators. GCaMP contains a GFP fluorophore and the CaM-M13 calcium binding domain [127]. Various improvements to this indicator have been made through multiple generations of GCaMP variants (GCaMP1.6, GCaMP2, GCaMP3, GCaMP5, GCaMP6, and GCaMP7) to overcome limitations such as pH and

temperature sensitivity, low fluorescence intensity, and nonlinear bleaching [126]. In our previous studies we used GCaMP6 as the first GECI that outperformed the existing synthetic indicators in terms of sensitivity and kinetic speed [128]. For experiments in chapter 4 of this thesis we used jGCaMP7f, which has demonstrated improved detection of individual spikes, and tracking large populations of neurons using 2-photon and widefield imaging [129].

1.7.2. Delivery methods for GECIs

Intracellular expression of GECI relies on delivery of the foreign encoded DNA into target cells. DNA must be transported into the nucleus and translated to the consequent protein [130]. DNA delivery methods are categorized as viral and non-viral. Non-viral methods rely on transfection through mechanical, electrical, and chemical means, which can be less harmful to cells but also less effective than viral methods. In retina studies the most commonly used methods of transfection are electroporation, viral vectors, or using transgenic animals. Electroporation has been shown effective in transfecting RGC populations in vitro and in vivo, however with limited labeling of non-RGC populations [131], [132]. Transgenic animals have also been used for transfection of neurons with GECIs. Pvalb-2A-Cre: Ai38 is an example line with GCaMP3 expressed in RGCs, horizontal cells, and Muller glia [133]. Generating an animal line that exclusively expresses calcium indicators in RGCs is challenging due to lack of a pan-ganglion-cell-specific promoter [134]. In addition, forming a stable transgenic animal line requires multiple animal generations which makes it challenging to keep up with the new generations of GECIs over time. Viral vectors have overcome these limitations in productivity and specificity [135], [136]. Adeno-associated virus (AAV) vector is the most common vector used for retinal gene transduction [137]. AAV is a small (25 nm) non-enveloped, replication incompetent, single-stranded DNA virus [138]. The advantages of AAV include the ability to achieve long term gene

expression, lack of toxicity and pathogenicity. In addition, compared to other virus vectors, AAV has a greater ability to target specific retinal cell populations. An AAV vector incorporating GCaMP5G has been able to specifically target 85% of RGCs, and this has been validated by retrograde tracer dye loading from the optic nerve [139].

1.7.3. Previous calcium imaging studies

A previous study in our group used GCaMP6f to study RGC stimulation thresholds with various pulse parameters. We showed that thresholds for RGC activation can be significantly reduced using asymmetric anodic-first stimuli with duration ratios (ratio of the anodic to cathodic phase duration) higher than 10, and symmetric anodic-first stimulation can avoid axonal activation, resulting in a more focal response shape (Fig. 1.6). However, symmetric anodic-first stimulation increases RGC activation thresholds due to the hyperpolarizing effect of the anodic phase. This

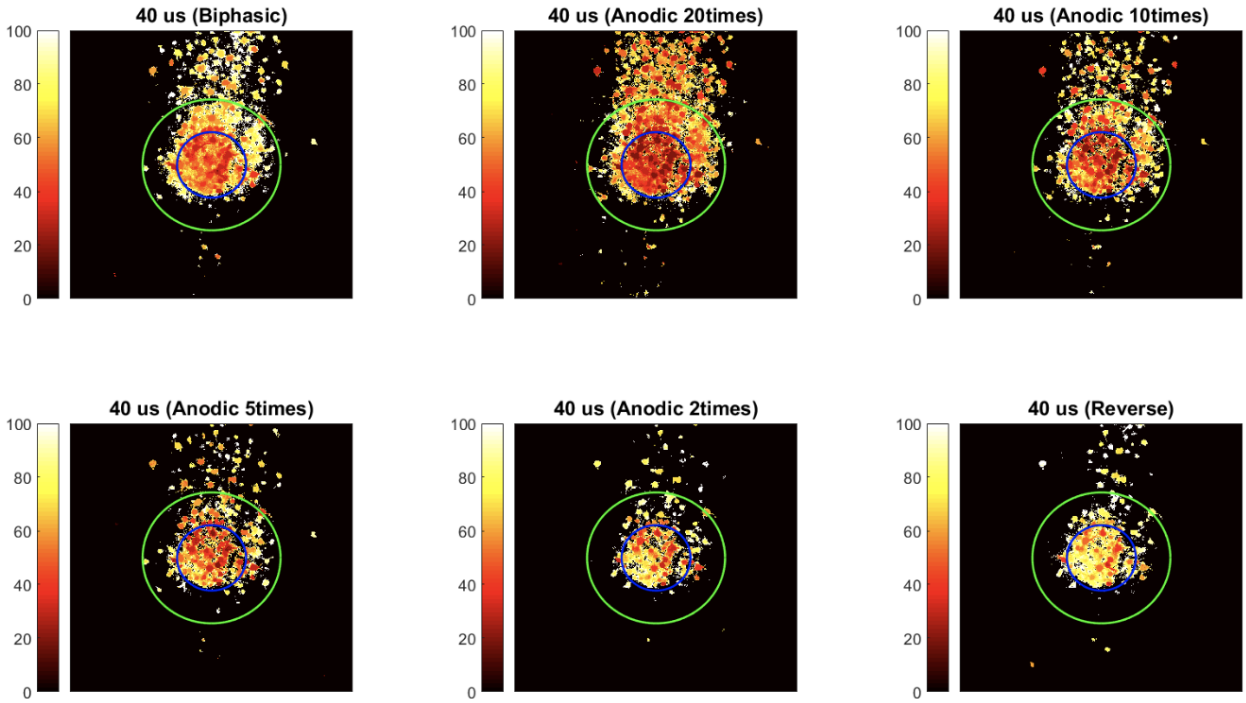

Figure 1. 6. Spatial threshold maps for RGCs in response to symmetric cathodic-first and anodic-first, and asymmetric anodic-first stimulation with different duration ratios (2, 5, 10, 20). Color bars show threshold in μm. Darker colors show lower thresholds and lighter colors show higher thresholds. (adapted from Chang et al. 2019)

hyperpolarization effect may be affecting axonal bundles more strongly compared to cell somas, which explains the focal RGC activity with this type of stimulation [140].

Another study demontrated that using longer pulse widths (≥25 ms) can create focal RGC responses and avoid axonal activation (Fig 1.7). This is due to indirect activation of RGCs through bipolar cells. Bipolar cells have longer time constants than RGCs and are activated by long-duration stimuli [90], [117], [119], [141]. They show that a 75 μm diameter electrode might be the optimal option for the highest selectivity of RGC somas over axons. Response size did not decrease

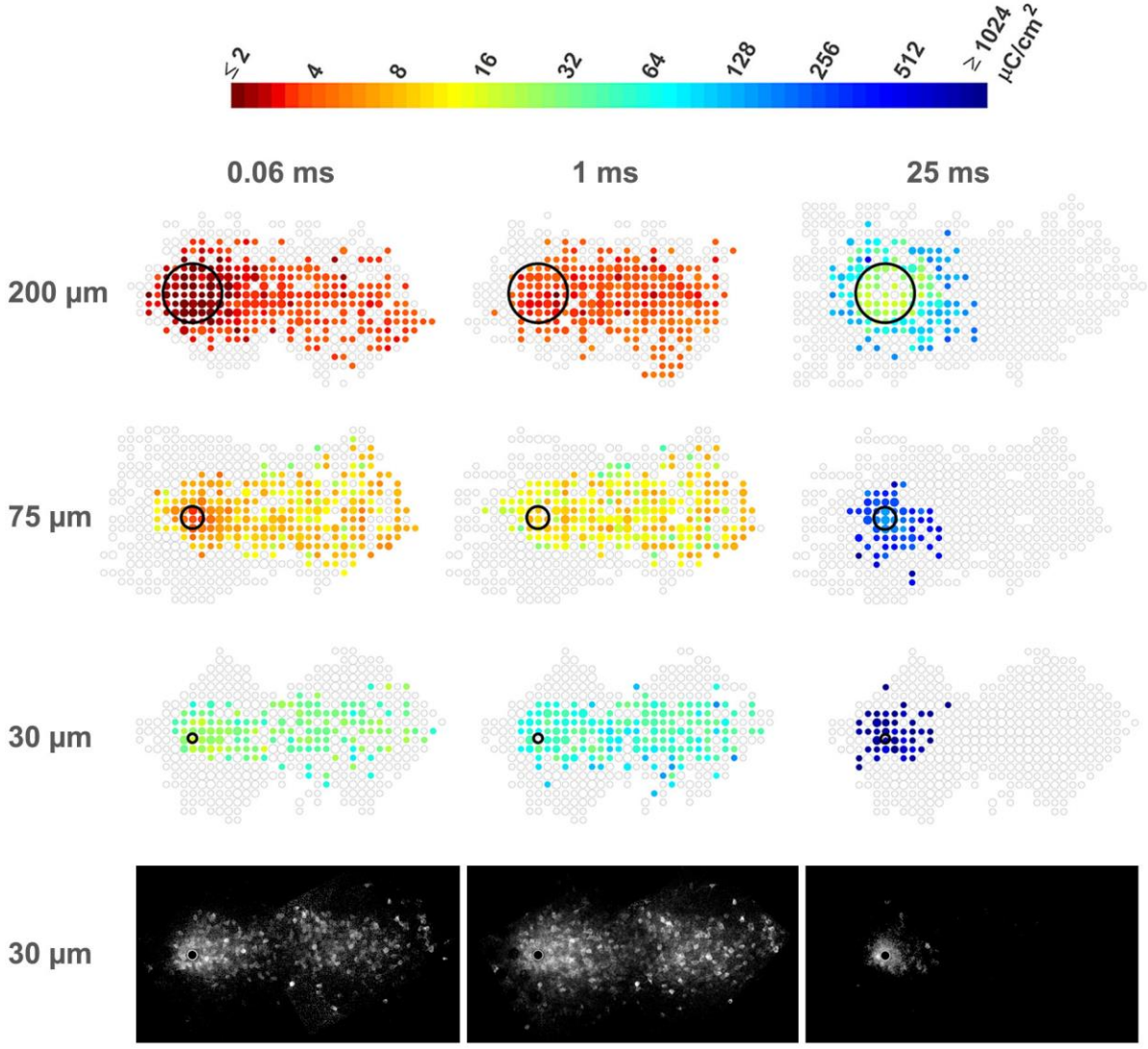

Figure 1. 7. RGC threshold maps for three electrode sizes and pulse widths. Corresponding calcium images for the 30 μm electrode are shown in the bottom row. (adapted from Weitz et al. 2015)

with electrode diameter for electrodes smaller than 75 μm, suggesting that there might be a lower limit to response size elicited by epiretinal stimulation [27].

1.7. Single cell and MEA recording findings

Patch clamp and MEA recordings from RGCs are other methods that provide insight into cell activation mechanisms. RGC desensitization to repetitive stimulation has been studied to provide a better understanding of visual percept fading [142]. Studies have found that electrical stimulation can cause feedback and feedforward inhibition in bipolar and ganglion cells that is induced by amacrine cells [143], [144]. Another study showed that some desensitization mechanisms are distinct from amacrine cell inhibition [87].

1.8. Biophysical modeling of the retina

One of the challenges for creating vision with electrical stimulation is the complexity of the retina. A simple grouping of cells into photoreceptor, bipolar, and RGC does not describe this complexity. The retina is an elaborate system of neurons connected together via synapses and gap junctions [145]. It consists of more than 50 types of neurons, arranged in three different neural layers. Although we have relatively sufficient understanding of the retinal cell types and anatomy, the underlying computation mechanisms of the retinal circuitry that result in high acuity vision are still poorly understood. Biophysical modeling of the retina allows for studying these mechanisms and developing a deeper understanding of retinal response dynamics. Neurons have been modeled with different complexities in previous studies. A single neuron can be characterized by a single-compartment model, a block compartment model, or a morphologically realistic model. Single compartment models have been used to model different types of RGCs, horizontal cells, bipolar cells, and photoreceptors [146]–[149]. In these models, the neuron membrane is approximated by a capacitance in parallel with different conductors that mimic ion channels. To capture the ion

channel kinetics of RGCs, Fohlmeister-Coleman-Miller modified the formulation of Hodgkin-Huxley model based on voltage clamp studies in tiger salamander RGCs [92], [150]. This model includes intracellular calcium dynamics as well as improved Na^+ and K^+ gating kinetics, to account for temporal spiking behaviors and provide flexibility in impulse encoding [151]. While single compartment models are simple and more efficient computationally, they have shortcomings in accurately predicting the biological behavior of RGCs due to lack of other neuronal compartments [152]. Block-compartment models are a good compromise between computational efficiency and model accuracy, as they are simplified versions of morphologically realistic models but include the essential anatomical compartments. The level of detail in these models depends on the specific study goals. Previous studies have shown that realistic RGC spiking behavior, comparable to electrophysiological recordings, can be achieved using only four neuronal compartments including soma, dendrites, thin segments, and axons [92]. Even simpler models (excluding dendrites) have been used to investigate axonal activation in epiretinal stimulation [153]. In this thesis, we use a block-compartment model of a RGC to study spiking behavior in response to asymmetric waveforms and interphase gaps.

1.9. Data-driven modeling of the retina

Data-driven models have the potential to provide insight into neural functions without relying on knowledge of biophysical and anatomical characteristics of the system under study. This method uses experimental data and defines linear or non-linear models that explain the relationship between the system's input and output variables. Some groups have taken this approach to predict retinal responses to electrical stimulation [154]–[156]. This method has been used on a single RGC to define the spiking behavior in response to electrical stimulation [155],

and on a network level to predict the overall retinal response based on electric fields in the retina [154]. Data-driven models have also been used to predict human perception from a visual scene and to multi-electrode electrical stimulation with the whole array [157]. In this thesis, we use calcium images to create data-driven models of RGC spatial activity and predict spatial response shapes to a range of stimulus parameters.

1.10. **Motivation**

A number of studies have focused on improving the resolution and image quality of retinal implants. There has been studies on reducing the electrode size and increasing pixel density [112][158], but implementation of these arrays is currently not feasible due to a high charge density requirement and packaging limitations [22]. Other groups have investigated using perforated membranes to promote cell proximity to the implant [159], but the long-term stability of migrated cells has not been confirmed. It has also been demonstrated that activation patterns can be affected by electrode interactions during multichannel stimulation and modifying the spatiotemporal patterns of stimulation can improve the resolution [81][84][160][161]. However, the factors that contribute to response variability among patients and electrodes, raise the crucial need to customize electrical stimulation parameters to each electrode in order to achieve focal activation and target neurons in a specific pattern [95][96][162]. To address this need, one of my works in this dissertation sought to implement an optimization algorithm to focally activate RGCs by iteratively modifying pulse amplitude, and type (symmetric cathodic-first, symmetric anodic-first, asymmetric anodic-first). The algorithm was tested on a data-driven model of RGC spatial activity and *in vitro* on the mouse retina using calcium imaging.

Another limitation of epiretinal implants is the high perception thresholds. A study of 30 patients with the Argus II retinal prosthesis demonstrated that about half of the electrodes had perception thresholds above the acute stimulation safety limit [99]. Those electrodes are used in groups with neighboring electrodes to allow for safe stimulation. This effectively creates larger electrodes, which further decreases the perceptual resolution. Investigating stimulation strategies to reduce perception thresholds has the potential to increase the resolution of retinal prostheses and improve the overall outcome for blind patients. In this thesis (Chapter 2), I performed human subject testing and computational modeling to examine the effect of pulse polarity order and asymmetry on perceptual thresholds and phosphene shape characteristics in Argus II patients. Psychophysical testing was done to determine the perecption probability using asymmetric anodic-first (AA) stimulation and, interphase gap (IPG), both individually and in combination. We also performed phosphene shape analysis to study the effect of symmetric anodic-first (SA) and AA stimuli on the shape of phosphenes.

As the mammalian retina is a complex system composed of more than 50 morphological types of neurons with different physiological functions [163][164], it is extremely difficult to predict the outcome of external electrical stimulation across this system. Computational modeling can help us better understand the statistical structure of RGC activation in response to stimulation, and study the effect of stimulus parameters such as pulse type, duration, and amplitude on the response of cells individually or in groups. Even though data-driven models do not account for the biophysical characteristics of cells, they have been successful in reconstructing and predicting the firing activity of neurons based on the spiking history [165][166]. A recent study demonstrated that a data-driven model of ON and OFF RGC responses to electrical stimulation can closely replicate the in vitro RGC activation map. The study also showed that a closed-loop algorithm can

identify optimal high frequency stimulation parameters for preferential activation of ON or OFF RGCs [167]. Recording the spatial activities of RGCs using calcium imaging allows real-time mapping of firing behavior in a large area [139]. The calcium imaging data that was previously collected in our lab [81] can provide insight into the statistical structure of spatial RGC activities. In Chapter 3 I developed data-driven models of spatial RGC activation in response to external stimulation based on the calcium imaging data. These models represented our *in vitro* experimental setup and were used as a test environment for the closed-loop optimization algorithm.

To study the spiking behavior of retinal neurons and optimize the performance of the retinal prosthetic implants, several groups have performed in vitro experiments to record from neuronal populations [117]. MEAs have been typically used for this purpose [112][168]; although MEA-based electrophysiology recording is appropriate for studying the temporal properties of RGC response, the spatial resolution is limited due to a number of factors such as the spacing between electrodes, the gap between RGCs and the electrodes, and the area covered by the MEA. Calcium imaging overcomes these limitations by allowing the recording of RGC activity in a large area [139]. Previous studies in our group have used an adeno-associated viral (AAV) vector to transduce RGCs with GCaMP5G [27] and GCaMP6f [79] from the family of genetically encoded calcium indicators (GECIs). Building on this prior work, I explored using the jGCaMP7f family with faster kinetics and higher detection sensitivity compared to the GCaMP6 family [129]. Using this technique, I mapped the spatial activity of RGCs via calcium imaging and modified stimulation parameters real-time to evoke activation in the region of interest.

Chapter 2 : The Effect of Waveform Asymmetry on Perception with Epiretinal Prostheses

A version of this chapter has been published in the Journal of Neural Engineering

Dorsa Haji Ghaffari, Kathleen E. Finn, V.Swetha E. Jeganathan, Uday Patel, Varalakshmi Wuyyuru, Arup Roy, and James D Weiland

2.1. Abstract

Retinal prosthetic implants have helped improve vision in patients blinded by photoreceptor degeneration. Retinal implant users report improvements in light perception and performing visual tasks, but their ability to perceive shapres and letters is limited due to the low precision of retinal activation, which is exacerbated by axonal stimulation and high perceptual thresholds. A previous *in vitro* study in our lab used calcium imaging to measure the spatial activity of mouse retinal ganglion cells (RGCs) in response to electrical stimulation. Based on this study, symmetric anodic-first (SA) stimulation effectively avoided axonal activation and asymmetric anodic-first stimulation (AA) with duration ratios (ratio of the anodic to cathodic phase) greater than 10 reduced RGC activation thresholds significantly. Applying these novel stimulation strategies in clinic may increase perception precision and improve the overall patient outcomes. We combined human subject testing and computational modeling to further examine the effect of SA and AA stimuli on perception shapes and thresholds for epiretinal stimulation of RGCs. Threshold measurement in three Argus II participants indicated that AA stimulation could increase perception probabilities compared to a standard symmetric cathodic-first (SC) pulse, and this effect can be intensified by addition of an interphae gap (IPG). Our in silico RGC model predicts lower thresholds with AA and asymmetric cathodic-first (AC) stimuli compared to a SC pulse. This

effect was more pronounced at shorter pulse widths. The most effective pulse for threshold reduction with short pulse durations (≤ 0.12 ms) was AA stimulation with small duration ratios (≤ 5) and long IPGs (≥ 2 ms). For the 0.5 ms pulse duration, SC stimulation with IPGs longer than 0.5 ms, or asymmetric stimuli with large duration ratios (≥ 20) were most effective in threshold reduction. Phosphene shape analysis did not reveal a significant change in percept elongation with SA stimulation. However, there was a significant increase in percept size ($P < 0.01$) with AA stimulation compared to the standard pulse in one participant. Including asymmetric waveform capability will provide more flexible options for optimization andn personalized fitting of retinal implants.

2.2. **Introduction**

Retinitis pigmentosa and age-related macular degeneration are prevalent retinal degenerative diseases that can lead to severe visual impairment or blindness [169], [170]. Retinal prosthetic implants have helped improve vision in people blinded by these conditions through electrically stimulating the remaining cells in the inner retina [21], [40], [70]. Patients with these implants report improvements in light perception and performing visual tasks [30], [32], [69], [75], [171], but their ability to perceive shapes and letters is currently limited [77], [80]. The best visual acuity (reported in peer-reviewed journals) is 20/1260 for epiretinal [99] and 20/460 for subretinal implants [52]. These acuity values do not yet demonstrate a level of restored vision that is better than legal blindness (20/200).

Clinical studies have shown that single electrode activation can lead to perception of elongated phosphenes in epiretinal implant users [73], [74]. Unintended activation of off-target retinal ganglion cells (RGC) due to stimulation of axons of passage [26], [27] is identified as an important contributing factor to elongated responses and therefore lower precision of retinal

activation. A study of 30 patients with the Argus II retinal prosthesis demonstrated that about half of the electrodes had perception thresholds above the acute stimulation safety limit [99]. To allow safe stimulation, such electrodes are used in unison with neighboring electrodes, effectively creating a larger electrode, which further decreases the perceptual resolution. Investigating stimulation strategies to reduce perception thresholds and create focal phosphenes has the potential to increase the resolution of retinal prostheses and improve the overall outcome for blind patients.

Our previous in vitro calcium imaging study [26] showed that asymmetric anodic-first stimulation with duration ratios (ratio of the anodic to cathodic phase) greater than 10 reduces RGC activation thresholds significantly, compared to a standard cathodic-first pulse. We also demonstrated that symmetric anodic-first stimulation with short durations (< 120 μs) results in a more focal response confined to the area near the electrode and presumably avoids stimulating axons of passage; however this type of stimulation also increases activation thresholds significantly.

In this study, we combined human subject testing and computational modeling to further examine the effect of pulse polarity order and asymmetry on perceptual thresholds and phosphene shape characteristics in Argus II patients. Psychophysical testing was done to determine how probability of generating a percept was effected by use of asymmetric anodic-first (AA) stimulation and, interphase gap (IPG), both individually and in combination. We also performed phosphene shape analysis to study the effect of symmetric anodic-first (SA) and AA stimuli on the shape of elicited percepts.

2.3. **Methods**

2.3.1. Human Subject Testing

Four eligible participants with the Argus II retinal prosthesis were recruited from the W.K. Kellogg Eye Center (University of Michigan, Ann Arbor, MI). Informed consent was obtained from each participant, following approval from the University of Michigan's Institutional Review Board (IRB). The study adhered to the tenets of the Declaration of Helsinki and the national regulations for medical device clinical trials (Clinicaltrials.gov identifier: NCT03635645).

Stimulation was delivered to patient implants using a research Video Processing Unit (VPU), controlled with the Clinician Fitting System (CFS) and the Asymmetric Waveform Research Tool (Second Sight Medical Products, Sylmar, CA, USA). A short pulse width (0.2 ms) was used for stimulation to induce direct activation of RGCs [26], [100], and to maintain the total pulse duration below 6 ms (Argus II limit) when applying AA stimulation. IPG was included as a variable, since it has been shown to reduce stimulation thresholds by delaying the opposing effect of the anodic phase on neural depolarization [172]. We compared its effect on threshold reduction with that of AA stimulation. In all experiments, 15% of the trials were catch trials randomly distributed among stimulus-present trials.

2.3.2. Threshold Measurement

Perceptual thresholds were measured for symmetric cathodic-first (SC) and SA stimuli for 4 electrodes per participant. First, an approximate threshold range was determined for each electrode by applying stimuli with increasing amplitude. Within the approximate threshold range, 10 pulse amplitudes were chosen for more thorough testing. Threshold was measured for all 4 electrodes during one "block" of testing and each electrode had a distinct set of 10 amplitudes for

testing. Each trial consisted of one electrode stimulated at one amplitude with 20 identical pulses over 1 second. The participant was cued with an audio tone to indicate (verbally) whether or not they saw a percept. Responses were collected for all 4 electrodes and 10 amplitudes in random order, to avoid desensitzation and order effects. A logistic function was fit to the data and threshold was defined as the pulse amplitude corresponding to 50% probablility on the logistic curve (Fig 2.1).

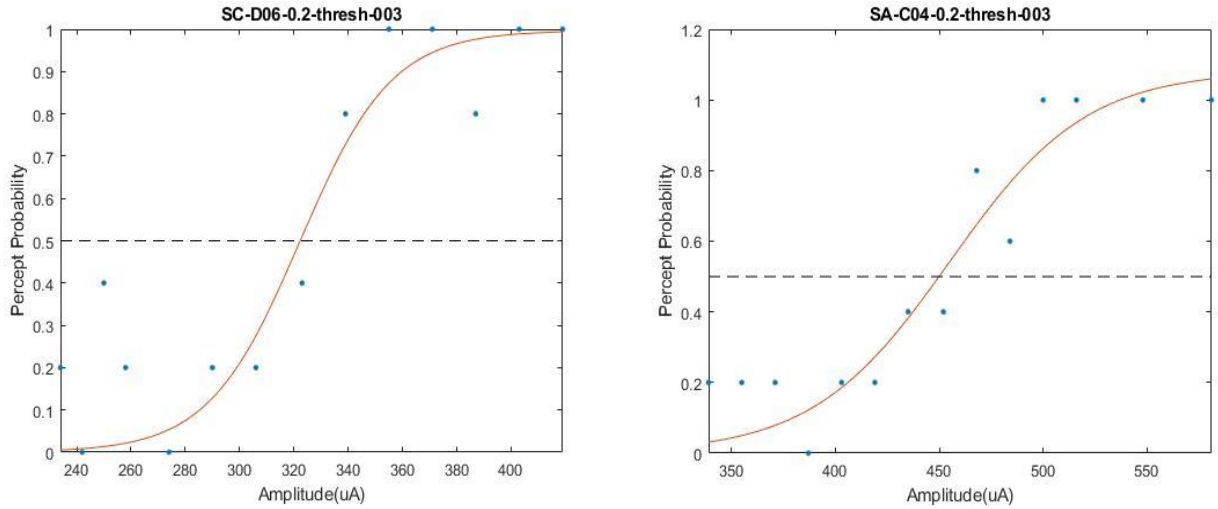

Figure 2. 1. Example logistic curves fitted to percept probability as a function of stimulation amplitude for electrode D06 (left) and C04 (right) for participant 3. Dashed line shows 50% probability of eliciting a percept.

Asymmetric pulses use two different amplitudes but must maintain charge balance. The Argus II implant has a limited set of current amplitudes available. Thus, only a limited number of asymmetric pulse durations and amplitudes were available to use. As a result, we could not follow the same protocol for estimating threshold described above, since a full logistic threshold curves could not be generated for asymmetric pulses. Instead, perception probabilities for multiple pulse types were measured and compared at a single amplitude. For asymmetric pulses, amplitude refers to the current in the cathodic phase. For each electrode we selected an amplitude value that satisfied three conditions: 1) A subthreshold amplitude (between 0% and 50% probability) based on the SC threshold curve calculated earlier, 2) availability of that amplitude with AA stimulation, and 3)

availability of a duration ratio higher than 10 at that amplitude. Four stimulation types (SC, SA, AA, SC + IPG) were delivered with the aforementioned amplitude and repeated 20 times each in order to calculate the perception probabilities. Each trial consisted of a pulse train of 20 pulses in 1 second. The active electrode and pulse type were chosen randomly in each block of trials. Based on our previous *in vitro* study [26], we hypothesized that AA pulses would have lower thresholds, and thus higher perception probabilities at the same amplitude. The same process was repeated (3 electrodes per participant) to measure perception probabilities in response to SC and AA stimuli with different IPG values (SCI and AAI). We used paired *t*-tests with Bonferroni correction to compare different groups of perception probabilities.

2.3.3. Phosphene Shape Analysis

Each trial began with a control experiment using tactile targets to calculate the participant's drawing bias and variability [73]. Participants were asked to feel the tactile shapes and draw them on a touch-screen monitor, considering the shape, size, and orientation of the objects (Fig. 2.2). For retinal stimulation trials, we asked participants to draw their perceptions in response to stimuli consisting of a pulse train delivered at 20 Hz for a total duration of 3 seconds (Fig. 2.3). We used SC, SA, and AA stimuli at a single amplitude. The amplitude value had to satisfy three conditions: 1) A suprathreshold amplitude based on the previously calculated SC threshold curve, 2) availability of that amplitude with AA stimulation, and 3) availability of a duration ratio higher than 10 at that amplitude. We chose a suprathreshold amplitude to ensure a phosphene in the majority of trials. Phosphene shapes were analyzed using two descriptors: area and elongation. Area is defined as the total number of non-zero pixels in the image, and elongation is the ratio of the major to minor axis of the best-fit ellipse. Inclusion of catch trials and randomization of

electrodes were done similarly to the threshold measurement task. Paired *t*-tests with Bonferroni correction were used to compare area and elongation for different pulse types.

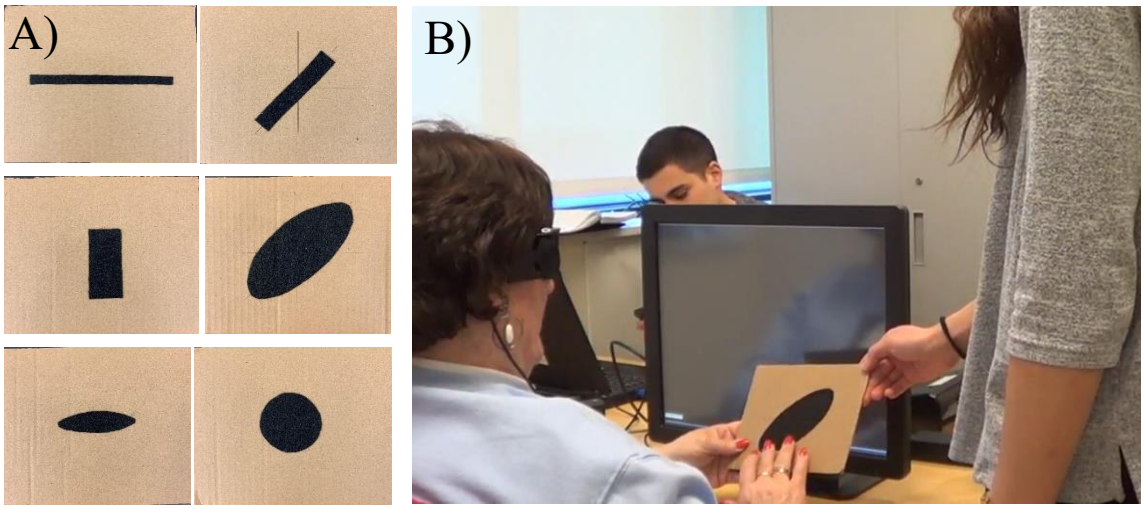

Figure 2. 2. Tactile target control task. A) tactile shapes. B) participant feeling the tactile shape before drawing on the touch screen.

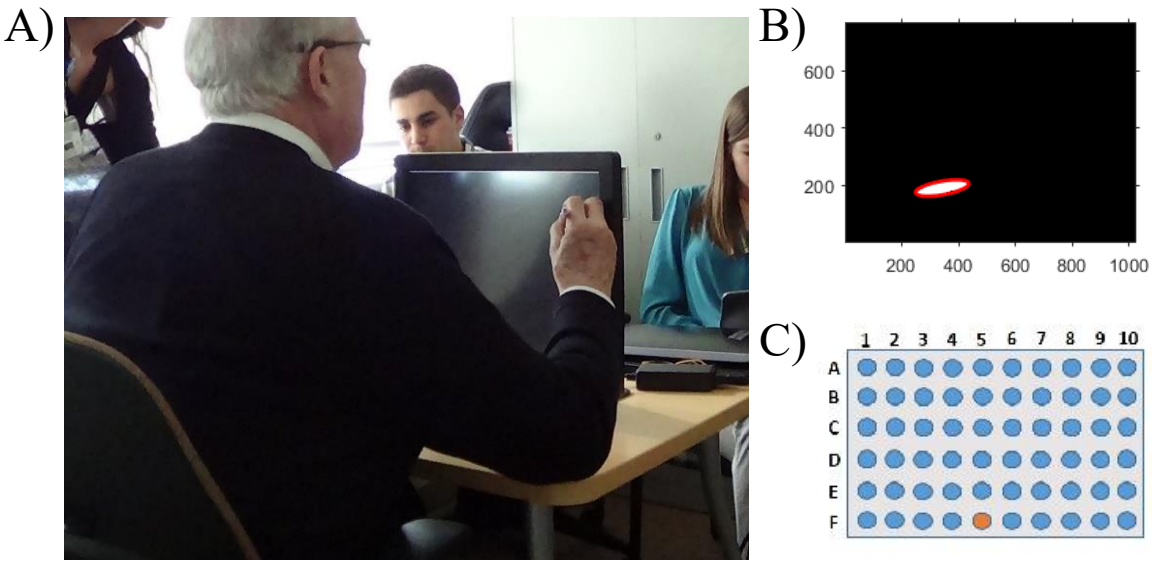

Figure 2. 3. Phosphene drawing task. A) participant drawing a phosphene after electrical stimulation. B) example drawing of a phosphene. C) active electrode in this example.

2.3.4. Computational Modeling

A computational model of a RGC with simplified geometry was built in the NEURON simulation environment [173] to study the effect of pulse asymmetry and polarity order on activation thresholds. This allowed us to test a more exhaustive parameter set than what was feasible with human subjects. The geometry and membrane kinetics were based on a previously published model [153] with modifications made to the length of segments. The model consisted of 1065 compartments of 1 µm length constructing an axon, narrow region of axon, initial segment of axon, and soma, with 1 mm, 45 µm, 10 µm, and 10 µm lengths respectively (Fig. 2.4). The RGC membrane included five nonlinear ion channels: sodium ($\bar{g}_{\mathrm{Na}}$), delayed rectifier potassium ($\bar{g}_{\mathrm{K,dr}}$), inactivating potassium ($\bar{g}_{\mathrm{K,A}}$), calcium activated potassium ($\bar{g}_{\mathrm{K,Ca}}$), and L-type calcium ($\bar{g}_{\mathrm{Ca}}$). The ion channel conductances varied by RGC region, as described in Schiefer *et al*. These were in parallel with a leakage conductance and a membrane capacitance. A point current source was placed above the axon – axon narrow region junction, at a 50 µm distance from the neuron vertically to simulate the thickness of the nerve fiber layer and inner limiting membrane [174]. The extracellular space was modeled as a purely resistive homogenous volume conductor with 500 Ω–cm resistivity [175]. To study the effect of AA stimulation on thresholds, six different pulse types were used: SC, and AA with 2, 5, 10, 20, and 30 duration ratios. Pulse widths ranged from 0.05 to 0.5 ms, and IPGs ranged from 0.1 to 2 ms. Electrical current pulses were delivered at 20 Hz for a total duration of 1500 ms (30 pulses). This frequency was chosen for consistency with the clinically used parameters. Electrcial potential at each point along the neuron was calculated using equation (1).

$$V_e = \frac{\rho_e I}{4\pi r} \tag{1}$$

Where V_e = extracellular potential, ρ_e = resistivity of the extracellular space, I = electrode current, r = distance between the center of each compartment to the electrode.

Numerical integration was done using a backward Euler method with a time step of 2 µs. Activation threshold was defined as the minimum amplitude at which the cell fired an action potential in response to at least 50% of the delivered pulses and calculated using a bisection algorithm with a ±0.1 µA error. Based on our *in vitro* study [26] and the human subject testing results, we hypothesized that AA stimulation with a large duration ratio reduced the threshold by the anode break excitation mechanism [176]. Differences in time constants for the *m*, *n*, and *h* gating variables are responsible for anode break excitation. After termination of a prolonged hyperpolarizing stimulation, the short time constant for sodium channel activation (*m*) leads to a sodium influx greater than potassium efflux, thereby increasing the probability of excitation. Adding a cathodic phase after termination of the anodic pulse further increases the excitation probability. Anode break was demonstrated in the squid giant axon, which is modeled by Hodgkin and Huxley using only Na^+ and K^+ channels. However, RGCs have at least 5 types of ion channels [177], [178], and the membrane potential follows (2) [150].

$$C_m \frac{dE}{dt} = -\bar{g}_{Na} m^3 h(E - E_{Na}) - \bar{g}_{Ca} c^3 (E - E_{Ca}) - \bar{g}_{K,dr} n^4 (E - E_K) - \bar{g}_{K,A} p^3 q (E - E_K) - g_{K,Ca}(E - E_K) - \bar{g}_L (E - E_L) + I_{stim} \quad (2)$$

Where *m*, *h*, *c*, *n*, *p*, and *q* are the gating variables of the voltage-gated ion channels, E_{Na}, E_{Ca}, E_K, and E_L are the equilibrium potentials of the ion channels, E is the membrane potential, $\bar{g}_{Na}$, $\bar{g}_{K,dr}$, $\bar{g}_{K,A}$, $\bar{g}_{K,Ca}$, $\bar{g}_{Ca}$ are the ion channel conductances, and C_m is the membrane capacitance. To gain insight into the mechanism of threshold reduction by AA stimulation in a

RGC, we analyzed the membrane voltage and the numerical values of gating variables over the course of stimulation.

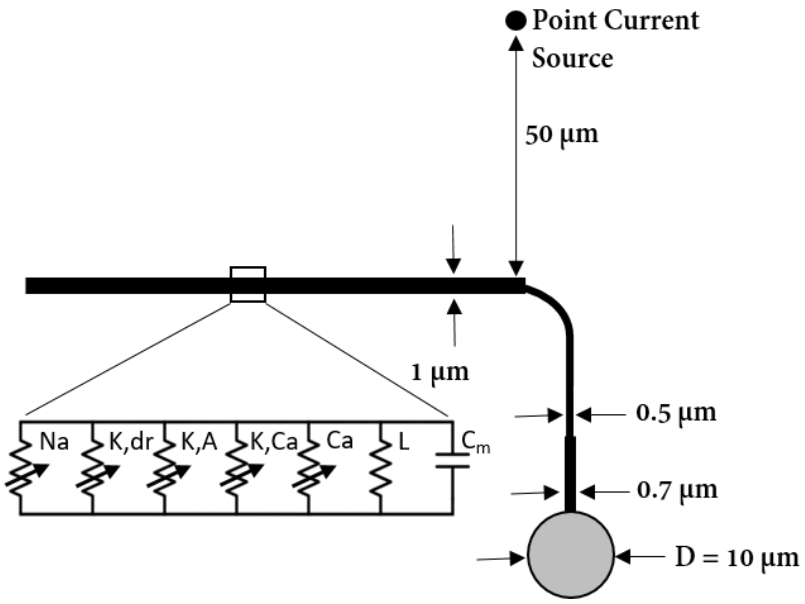

Figure 2. 4. Computational model of a single retinal ganglion cell. The geometry consists of the RGC soma, axon initial segment, axon narrow region, and axon. A point current source is positioned 50 µm above the axon- axon narrow region junction. Each compartment consists of five ion channels (Na^+, delayed rectifier K^+, inactivating K^+, Ca^{2+} activated K^+, and L-type Ca^{2+}), a leak channel, and a membrane capacitance. (figure is not drawn to scale)

2.4. **Results**

2.4.1. Human Subject Testing

Perception threshold and probability measurement was performed on four Argus II participants. One participant was removed from the analysis due to a high false positive rate (55-70%). Results from the remaining participants were analyzed separately and are shown in figure (2.5). The full logistic threshold curve could not be generated for SA stimulation for participant 3, since the perception probability did not reach the threshold despite stimulation with the maximum amplitude allowable within the safety limits. For participants 1 and 2 there was an increase in thresholds with SA compared to SC stimulation, consistent with previous *in vitro* studies [26],

[55], [179]. This difference was significant for participant 1 (29.66% increase in average threshold, $P < 0.05$), and not significant for participant 2 (19.58% increase in average threshold). All *p*-values were adjusted by the Bonferroni correction since multiple hypotheses were being tested in each experiment. We demonstrated that AA stimulation and SC stimulation with an IPG increase perception probability significantly compared to both SC and SA stimuli in participants 1 and 2. Participant 3 showed no difference in perception probabilities (Fig. 2.5. A3). This might be due to the participant not reporting phosphenes accurately, evident from his high false positive rate on that day (31.67 %). Introducing an IPG to the SC pulse raised the perception probability significantly regardless of the IPG duration in participant 1. Perception probability increased with the duration of IPG in participants 2 and 3, however this change was not significant (Fig. 2.5. B2 and B3). Adding an IPG to the AA pulse increased the perception probability in participant 1, however not significantly (Fig. 2.5. C1). This effect was less obvious for the other two participants (Fig. 2.5. C2 and C3).

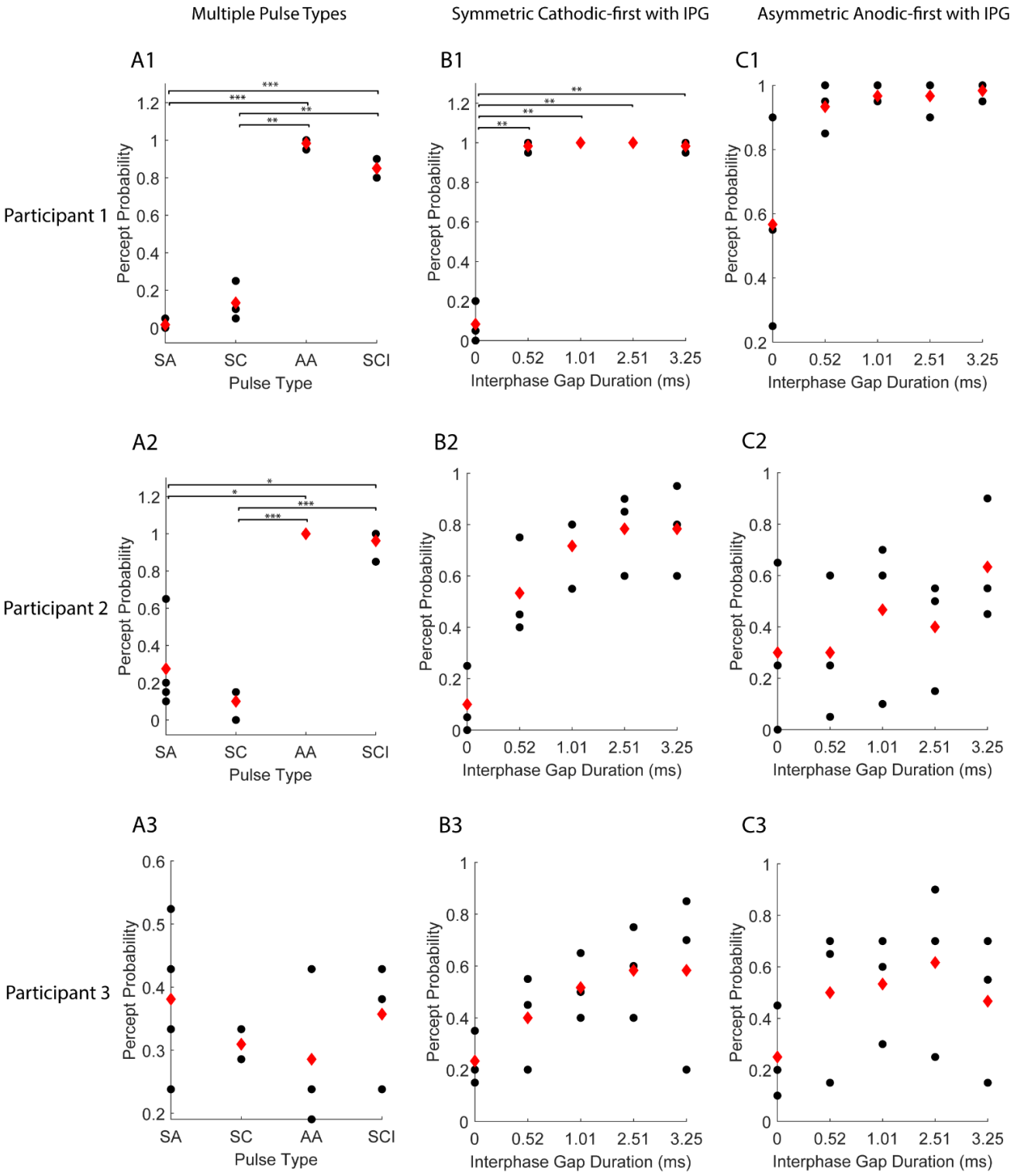
Multiple Pulse Types
Symmetric Cathodic-first with IPG
Asymmetric Anodic-first with IPG
A1
B1
C1
A2
B2
C2
A3
B3
C3
Participant 1
Participant 2
Participant 3
Percept Probability
Pulse Type
SA
SC
AA
SCI
Interphase Gap Duration (ms)
0
0.52
1.01
2.51
3.25

Figure 2. 5. A1-A3) Perception probability comparison for different pulse types in human participants. Each plot represents perception probability values for SA, SC, AA, and SCI stimuli for 4 electrodes. False positive rates: participant 1 = 0 %, participant 2 = 0 %, participant 3 = 31.67 % B1-B3) Perception probability comparison for SC stimulation with different IPG values. Each plot represents perception probability values for SC pulse with different IPG values measured for 3 electrodes. False positive rates: participant 1 = 9 %, participant 2 = 0.8 %, participant 3 = 12 % C1-C3) Perception probability comparison for AA stimulation with different IPG values. Each plot represents perception probability values for AA pulse with different IPG values measured for 3 electrodes. False positive rates: participant 1 = 9 %, participant 2 = 0.8 %, participant 3 = 12 %. (P<0.05*, P<0.01**, P<0.001***). In some cases (plot 1B for example), the data points overlap. Black dots represent perception probability values for individual electrodes. Red diamonds represent the average perception probability for each column of data.

Phosphene shape analysis revealed no significant difference between percept elongations in response to SA, SC, and AA stimuli. Average phosphene area was significantly larger with AA stimulation compared to SC (121.67% increase, P < 0.01) and larger compared to SA (64.8% increase) for participant 2. An increase in average phosphene area with AA stimulation was observed in participants 1 (38.64% increase from SC, 8.1% increase from SA) and 3 (2.39% increase from SC, 3.26% increase from SA), but this change was not significant. Perception thresholds were lower with AA stimulation, therefore with the same amplitude it is expected that this pulse creates larger percepts compared to symmetric pulses. Figure 2.6 and 2.7 show example

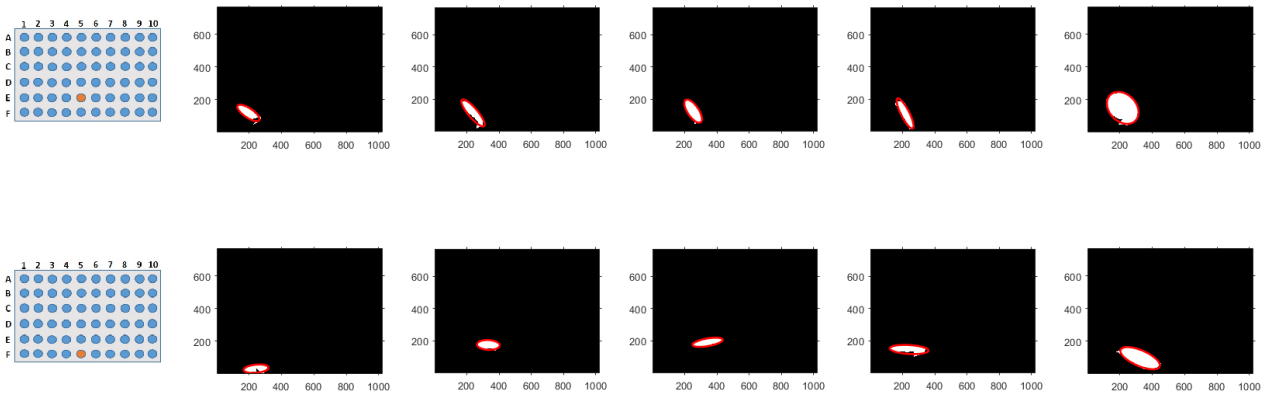

Figure 2. 6. Example phosphene drawings for participant 3. Top and bottom row show phosphene drawing examples for asymmetric anodic-first pulses with 0.1 ms duration for two different electrodes. 5 similar trials were done for each electrode and drawings were averaged for statistical analyses.

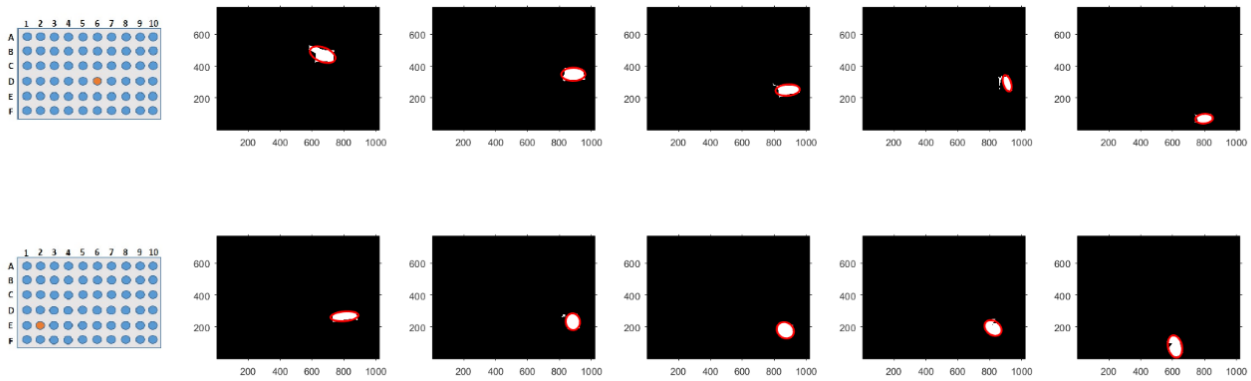

Figure 2. 7. Example phosphene drawings for participant 1. Top and bottom row show phosphene drawing examples for asymmetric anodic-first pulses with 0.2 ms duration for two different electrodes. 5 similar trials were done for each electrode and drawings were averaged for statistical analyses.

drawings for participant 3 and 1 respectively in response to asymmetric anodic-first pulse train with 0.1 ms and 0.2 ms cathodic phase pulse width.

2.4.2. Computational modeling

A computational model of a RGC (described in 2.2) was used to further investigate the effect of order and duration ratio of pulse polarities on activation thresholds in epiretinal stimulation. The model predicts lower activation thresholds with longer IPGs, consistent with our human subject testing results and with previous research studies [172], [180], [181]. Our results reveal that the effect of IPG is more pronounced for shorter pulse widths (Fig. 2.8). Figure (2.9) shows the percent change in threshold with AA stimulation of different duration ratios vs. SC stimulation. The model predicts lower activation thresholds with higher duration ratios, consistent with our previous *in vitro* research study [26]. The threshold reduction effect is more pronounced with shorter pulse widths.

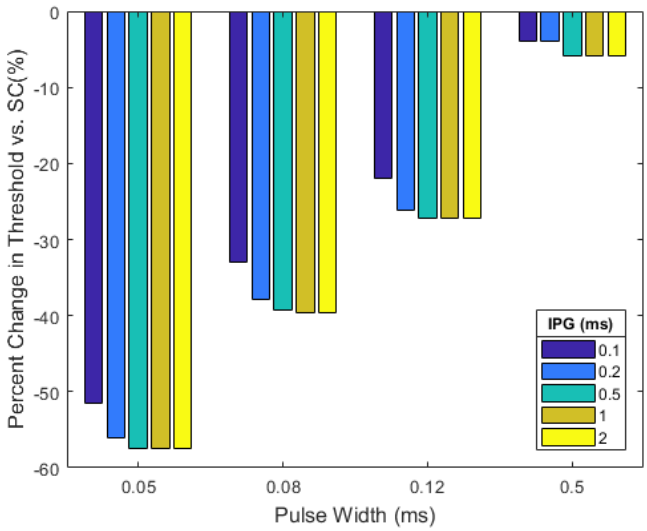

Figure 2. 8. Model predictions of percent change in activation threshold with SC stimulation with interphase gap vs. no interphase gap in a RGC. Effect of IPG on threshold reduction is stronger for shorter pulse widths.

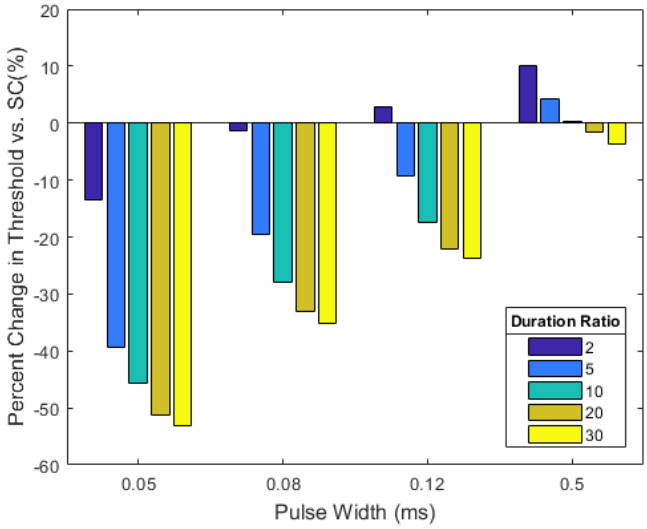

Figure 2. 9. Model predictions of percent change in activation threshold with AA vs. SC stimulation in a RGC. Effect of AA stimulation on threshold reduction is stronger for shorter pulse widths.

Figure (2.10) shows these parameters during an anodic pulse of 2 ms and 5 µA amplitude. In this model, with the electrode positioned nearest the junction of axon - axon narrow region, the action potential initiated in the narrow region. The sodium (Na^+) and delayed rectifier potassium (K^+,dr) currents are dominant because the membrane conductances for other ionic currents are

negligible in the axon narrow region [153], [182]. There is a reduction in the *m* and *n* values and an increase in the *h* value. These changes are more gradual for *n* and *h*, and more immediate for *m* during the anodic pulse due to their different time constants ($\tau_m << \tau_n , \tau_h$). After removal of the hyperpolarizing pulse, *m* rapidly returns to its normal value while *h* is still elevated and *n* is depressed, which promotes $I_{Na} > I_K$ and a high excitation probability. Figure 2.10.A and B were single pulses extracted from trains of 10 pulses. An anodic only pulse evoked an action potential once out of 10 pulses, while the AA pulse evoked an action potential 10 out of 10 pulses. This model result supports the mechanism of anode break as a means of making cells more sensitive to cathodic stimulation, if not exciting cells directly.

If the action potential is generated in the initial segment of axon (axon hillock), other ionic currents ($I_{K,A}$, I_{Ca} , and $I_{K,Ca}$) also need to be studied for a comprehensive examination of RGC activation mechanism with AA stimulation. The long hyperpolarizing current causes a drop in *m*, *n*, *p*, and *c*, and an increase in *h* and *q* values. The reduction in *p* and elevation in *q* (Fig. 2.10) results in an overall lower $I_{K,A}$ and lower total potassium current according to (2). I_{Ca} is expected to decrease during the hyperpolarization as *c* is lowered. However, the Ca^{2+} current has a negligible contribution to action potential generation and due to slower kinetics, only appears after the sodium channel activation has initiated the spike [147]. $I_{K,Ca}$ is very small compared to other ionic currents during an action potential and is only dominant during the early portion of the interspike interval. There is no independent gating variable defined for the calcium activated potassium channel and the change in its conductance is ligand-gated based on the internal Ca^{2+} concentration. The Ca^{2+} concentration is virtually constant before initiation of the spike. However, a small decrease in $I_{K,Ca}$ is expected due to the membrane hyperpolarization according to (2). After removal of the

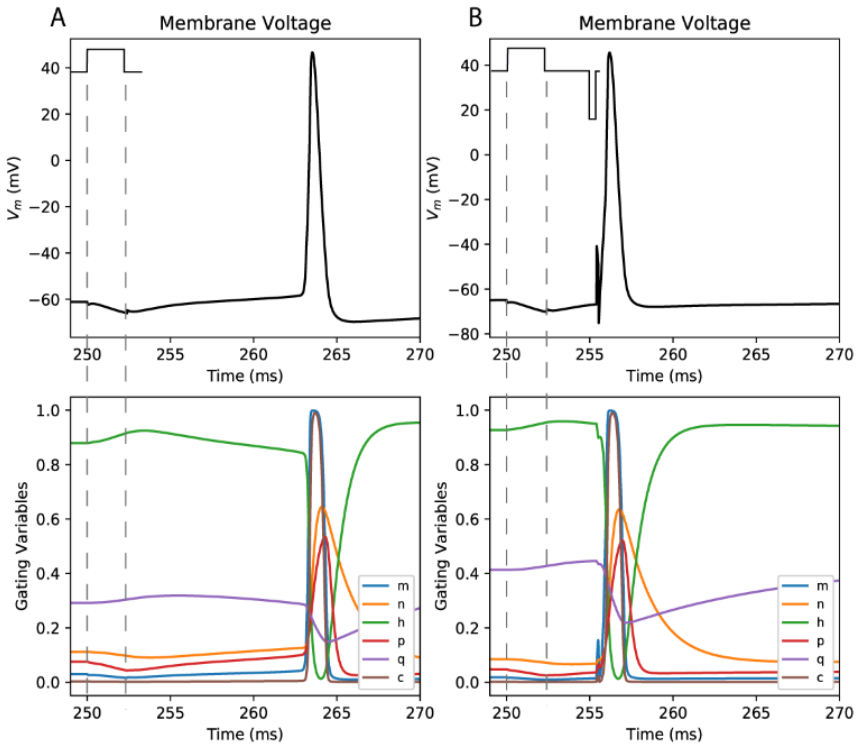

Figure 2. 8. Membrane response to stimulation in the RGC computational model. A) *Top:* Membrane voltage in response to an anodic pulse. The cell spikes with some latency after termination of stimulation. Stimulation includes an anodic current pulse of 2.4 ms duration and 5 µA amplitude. *Bottom:* Membrane gating variables before, after and during stimulation (between the dashed lines). Varying time constants of the gating variables results in an action potential. B) *Top:* Membrane voltage in response to an AA pulse. The cell spikes in response to the cathodic phase of the stimulus. Stimulation includes an AA current pulse of 2.4 ms anodic and 0.12 ms cathodic phase duration, with 5 µA anodic and 100 µA cathodic phase amplitude. *Bottom:* membrane gating variables before, after and during stimulation. Dashed lines show the limits of the anodic phase. The anodic only pulse evoked an action potential once out of 10 pulses, while the AA pulse evoked an action potential 10 out of 10 pulses. The differences in the initial values of the gating variables between A and B are due to the cumulative effect of previously applied pulses.

hyperpolarization, sodium current begins to recover rapidly while the total potassium current is still lowered due to the slower kinetics of potassium channels. This makes the membrane more excitable.

We used our model to investigate a wider range of stimulus settings than was practical in the human subjects. In particular, we investigated AA stimulation with different IPG values for comparison to human testing results, and asymmetric cathodic-first (AC), which was not tested in human subjects. Figure (2.11) displays the percent threshold change in response to a range of IPGs (0-2 ms) and pulse types (AC and AA with 2, 5, 10, 20, 30 duration ratios, and SC). The effect of

IPG duration on threshold with all pulse types could be described by a decaying logarithmic function. The effects of both IPG and asymmetric pulses on thresholds are less pronounced for longer pulses.

The comparison of AA to AC pulses demonstrated that AA is more effective than AC in threshold reduction but only at smaller duration ratios with longer IPGs for 0.05 – 0.12 ms pulse widths. This indicates that the anode break mechanism is more effective at reducing thresholds with a higher amplitude anodic phase and a gap between the anodic and cathodic phases. This is in agreement with the anode break excitation mechanism (Fig. 2.10) since the gating variable dynamics can result in membrane excitation only with some latency after termination of the hyperpolarizing pulse [176]. In absence of a gap or with shorter gaps, AC is more effective than AA. Both reduce the threshold by applying an anodic phase with lower amplitude and longer duration compared to the anodic phase of symmetric pulses, reducing the inhibitory effect of the anodic phase. However, with AC the inhibitory phase comes after the excitatory phase. Thus, multiple factors appear to contribute to achieve the lowest excitation threshold. Our initial hypothesis that the threshold reduction effect of AA stimulation is based on the anode break excitation mechanism is partially supported by the results. AA pulses with small duration ratios ($\leq$ 5) and long IPGs ($\geq$ 2 ms), were most effective in threshold reduction for 0.05 – 0.12 ms pulse

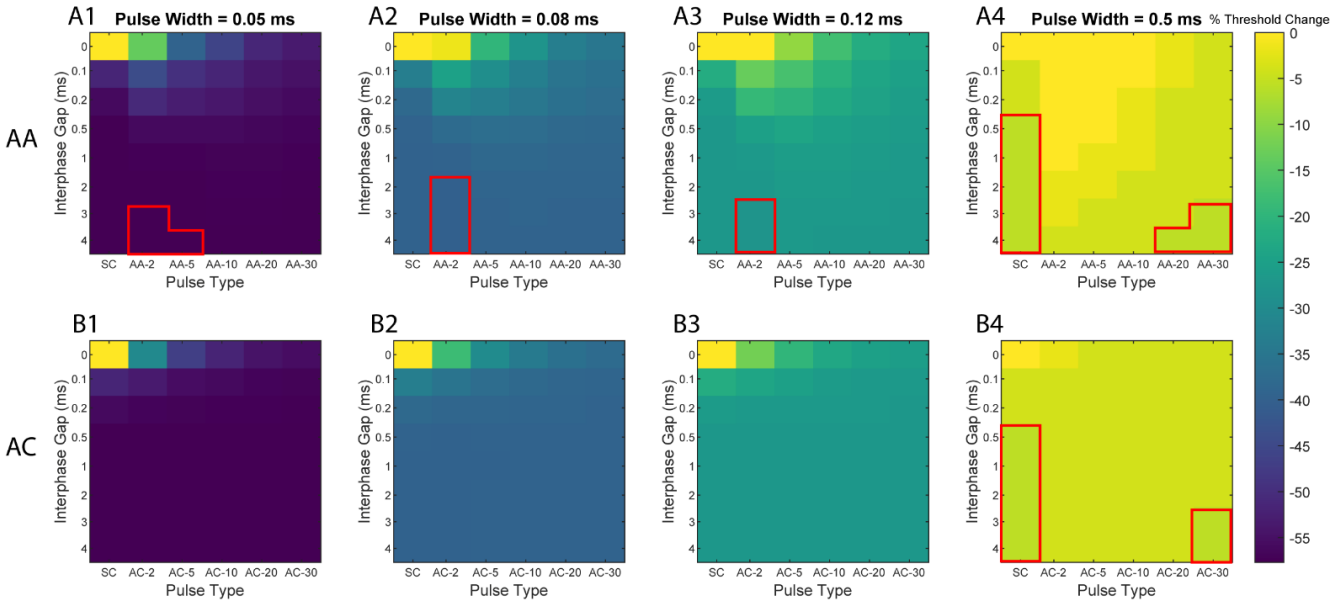

Figure 2. 9. Model predictions of percent change in activation thresholds with different pulse types and IPGs vs. standard SC stimulation. A1-A4) threshold change for AA vs. SC. The x-axis for each colormap represents pulse types: SC, AA with 2, 5, 10, 20, and 30 duration ratios. B1-B4) threshold change for AC vs. SC. The x-axis for each colormap represents pulse types: SC, AC with 2, 5, 10, 20, and 30 duration ratios. The y-axis represents IPG values. The color bar limits were kept constant to allow comparison between different pulse widths. The tiles with the highest threshold reduction percentage are outlined with a red line for each pulse width. The threshold reduction effects of IPG and asymmetric stimuli are less with longer pulse durations.

widths. SC pulses with IPGs longer than 0.5 ms, and asymmetric pulses with large duration ratios ($\geq$ 20) were most effective in threshold reduction for 0.5 ms pulse widths (Fig. 2.11).

2.5. **Discussion and Conclusion**

Our human subject testing and computational modeling of a single RGC establish that asymmetric anodic-first stimulation is an effective strategy to reduce stimulation thresholds in epiretinal stimulation and that this effect is stronger at higher duration ratios, consistent with our *in vitro* findings in mice [26]. Our computational modeling results demonstrate that this threshold reduction effect is more pronounced for shorter pulse widths. Even though the threshold current is lower with longer pulse widths, charge per phase increases with pulse width [101], [158], [168]. Therefore, using shorter pulses in clinic will likely be advantageous because the safety limit is

defined in terms of charge per unit area. Using short AA pulses can lower the threshold currents compared to a standard cathodic-first biphasic pulse, while maintaining the benefit of low charge per phase associated with short pulses.

According to our computational modeling results (Fig. 2.9) and previous *in vitro* findings, AA stimulation with smaller duration ratios (≤ 5) is less effective for threshold reduction. However, our model which tested a combination of AA stimulation and IPG (Fig. 2.11), indicated that AA pulses with small duration ratios (≤ 5) and long IPGs (≥ 2 ms) are amongst the most effective stimuli in threshold reduction. We have previously shown that smaller duration ratios of AA stimulation produce focal responses, meaning the RGC response is confined to the region near the active electrode [26]. A study has shown that bipolar cells are more sensitive to long anodic-first biphasic pulses due to the presence of cyclic nucleotide-gated (HCN) channels [183]. This can likely contribute to less axonal activation with anodic-first pulses due to indirect RGC activation, and provide an advantage for anodic-first pulses compared to cathodic-first pulses. If adding an IPG to small duration ratio AA stimulation maintains a focal response, then this pulse type can offer great potential for threshold reduction and focal phosphenes simultaneously. Experimentation with combinations of AA and IPG will be necessary to suppport this claim. We based our model on a previously published RGC model [153]. Although this model has a relatively simple geometry, it has predicted an experimental finding confirmed by our prior work, specifically that pulse widths below 0.1 ms avoid axonal activation [27]. However, a number of details have not been included in the model that might affect the threshold values. We investigated only a single electrode-retina distance, though it has been shown that this distance affects excitability [184]. Different RGC types and neurite geometries respond differently to electrical stimulation [185], [186], and using a disc electrode might affect RGC responses [182]. Thus, the

specific predictions of our modeling study (e.g. using a duration ratio less than 5) may not hold when other models are used, and when tested clinically. But more generally, the model predictions are consistent with our clinical data and the results taken together support the claim that asymmetric pulses are an important feature to include in future prosthesis design, to allow optimization of pulse parameters.

The effects of AA stimulation had a similar pattern among our human participants, but variability inherent in human subjects testing made these results less clear. Recruitment is a challenge. We were able to enroll four participants in these experiments. Argus II subjects are typically elderly, and due to their blindness, are dependent on others for transportation. Three of the four participants live several hours away from the University of Michigan, which further limited their participation. The number of electrodes tested was also small because experiments were repetitive and mentally taxing for the participants and their time on campus was limited. We used manual process to measure perception thresholds since the automated process could not deliver anodic-first pulses. This added to the testing duration. In addition to the small sample size, other factors contributed to variability in participants' responses. Participants' accuracy in reporting phosphenes can be influenced by the time they take to respond to stimulation and their background visual activity (spontaneous phosphenes). This background activity can vary day-to-day. Intersubject differences that might be introducing variability to our data include the position of the implant on the retina, the electrode-retina distance, and the amount of retinal degeneration under the implant. The comparison of perception probabilities in response to different pulse types and IPGs was done at a single amplitude value due to the following reasons: 1) The software limitation prevented us from directly measuring the thresholds and 2) Our amplitude selection criteria and the tedious nature of the experiments did not allow for testing with more settings. The

pattern of change in perception probability can be a representation of change in perception threshold. However the variability of location of the chosen amplitude on the logistic curve (based on the three criteria mentioned in the methods section), introduces some noise to the perception probability values.

Phosphene shape analysis revealed no significant difference among percept elongations with different pulse types. We expected less elongated phosphenes with short SA stimulation based on our in vitro findings. We have demonstrated that this pulse type activates cell bodies preferentially and avoids axonal stimulation, resulting in a more focal response [26]. In the current study, phosphene elongation was compared for different pulse types at only one amplitude. Since pulse amplitude has been shown to effect the elongation of activation area with SA stimulation [26], this comparison needs to be done at different amplitudes for a more valid comparison with the in vitro study, but was not possible with the limitations on AA pulse amplitude. We observed a significant increase in phosphene size with AA stimulation compared to SC and SA in participant 2. Larger phosphenes with AA stimulation may be due to the lower activation thresholds with this pulse type, but this was noted in only one participant. Overall, there were not reliable trends relating pulse type to phosphene shape.

Our results suggest that incorporating asymmetric stimulation as an option can improve retinal prosthesis function. Lower perceptual threshold provides a wider dynamic range for stimulation amplitudes and phosphene sizes, which results in more flexibility for retinal stimulation. In addition, it allows for individual usage of electrodes that were previously grouped with neighboring electrodes due to high thresholds, and potentially improving the perception resolution. Lower perceptual thresholds will also result in lower power consumption. Our conclusions are limited by the small sample size and must be validated in a larger number of

participants. On the whole, our data demonstrates the need for more flexible programming options in retinal prostheses. Optimization of the stimulation protocol for each patient will be necessary for the best outcomes. Systems that can only produce symmetric, biphasic pulses will limit optimization.

Chapter 3 : Closed-loop Optimization of Retinal Ganglion Cell Responses to Epiretinal Stimulation: A Computational Study

A version of this chapter has been published in IEEE Xplore (NER 2021)

Dorsa Haji Ghaffari, Yao-Chuan Chang, Ehsan Mirzakhalili, and James D. Weiland

3.1. Abstract

Retinal prostheses improve vision for patients with retinal degeneration. However, the shape recognition ability of retinal prostheses users is limited due to the low visual resolution of these devices. Off-target retinal ganglion cell (RGC) activation is an important contributing factor to the low stimulation precision. Previous research has shown RGC spatial activity and perception of shapes by users can be difficult to predict due to the complexity of retina structure and electrode-retina interactions. In this study we demonstrate a method to iteratively search for optimal stimulation parameters that create focal RGC activation *in silico.* Our findings indicate that stimulation parameters can be customized to each electrode in a closed-loop manner. This approach can potentially eliminate the time-consuming process of searching a broad range of parameters for optimal stimulation outcome and provide more control over personalized fitting of retinal implants.

3.2. Introduction

Retinal prostheses help restore functional vision to patients blinded by retinal degenerative diseases such as retinitis pigmentosa and age-related macular degeneration [21], [22], [70]. These devices produce percepts by electrically stimulating the remaining layers of the retina. Even though retinal prosthesis users report improvements in perceiving light and performing visual tasks, their ability to perceive shapes and letters remains limited [77], [80]. The best visual acuity is 20/1260 [99] for epiretinal and 20/460 [52] for subretinal implants. These values are lower than the acuity level for legal blindness (20/200). Perception quality is highly dependent on the capability to precisely activate the target retinal cells. However, *in vitro* studies have demonstrated off-target retinal ganglion cell (RGC) activation in response to electrical stimulation [26], [27]. Human subject testing has also shown that a single electrode activation results in perception of elongated phosphenes in subjects, confirming the *in vitro* results with respect to off-target activation of RGCs [73], [88]. Off-target stimulation results from a number of factors including unintended axonal activation, electric field spread [71], [187], large electrode size, and spatiotemporal interactions between electrodes [84]. A number of studies have focused on modulation of the stimulation protocol to avoid axonal activation. Using long duration pulses [27], and low-frequency sinusoidal stimulation [90] are amongst these stimulation strategies. Yet these protocols have not been proven clinically feasible due to high threshold charge densities. Our previous *in vitro* study showed that symmetric anodic-first stimulation, and asymmetric anodic-first stimulation with small duration ratios (ratio of anodic to cathodic phase duration) can avoid axonal activation [26]. However the clinical results did not show significant improvement in phosphene shapes with these pulses [188]. In addition to phosphene elongation, phosphene shapes are highly variable across electrodes and subjects. This inconsistency confirms that despite the

clinical use of retinal prostheses, the visual experience of retinal implant users is inadequately understood [74]. Complex axonal pathways, variable electrode-retina separation, inconsistent health of the surviving neurons across the retina, and how the brain interprets neuronal responses contribute to this unpredictability [93], [94]. Thus, there is a crucial need to customize electrical stimulation parameters to each electrode for focal activation of the target neurons.

In this study, we developed data-driven models of RGC spatial activity and optimized stimulation parameters with a closed-loop algorithm to elicit focal responses. This approach provides a method to quickly search through a broad range of pulse parameters to achieve the desired RGC activation.

3.3. Methods

3.3.1 Data-driven Modeling of RGC Spatial Activity

Calcium images from previous *in vitro* experiments [26] were used to create data-driven models of RGC response to electrical stimulation for 48 regions (from 11 mouse retinas). Calcium imaging reveals RGC activity using the Ca^{2+} transient change in spiking neurons. GCaMP6f was expressed in RGCs by intravitreal injection of an adeno-associated virus (AAV) vector two-four weeks prior to sacrificing the animal. Spatial activity of RGCs in response to a single electrode stimulation was quantified with two descriptors: area and eccentricity. Area was defined as the area of the best-fit ellipse to the calcium activity, and eccentricity was defined as the ratio of the distance between the ellipse foci to its major axis length. Eccentricity values are always between 0 and 1 (0 is a circle and 1 is a line segment), and are used as a measure of response elongation. Calcium images were recorded in response to a train of anodic-first pulses at 120 Hz frequency lasting 5 seconds. Cathodic phase duration was always 40 μs and the anodic phase duration

changed based on the duration ratio. Electrical stimulation parameters included pulse amplitude and type. The range for pulse amplitude and type was 10 to 100 μA and 1 to 20 respectively. Pulse type is defined as the ratio of the anodic to cathodic phase duration and pulse amplitude is the amplitude of the cathodic phase in μA. For the purpose of this study we used calcium image responses to 50 different combinations of pulse amplitude and type.

A single model could not be formulated to define the relationship between pulse parameters and spatial response descriptors that was consistent across the 48 retinal regions. Therefore, we trained feedforward artificial neural networks (ANN) for each region separately to quantify this relationship. Data points were divided into three subsets of training (80%), validation (10%) and test (10%). The inputs to the networks are pulse amplitude and type, and outputs are area and eccentricity. The ANNs include ten hidden layers and they all have hyperbolic tangent transfer

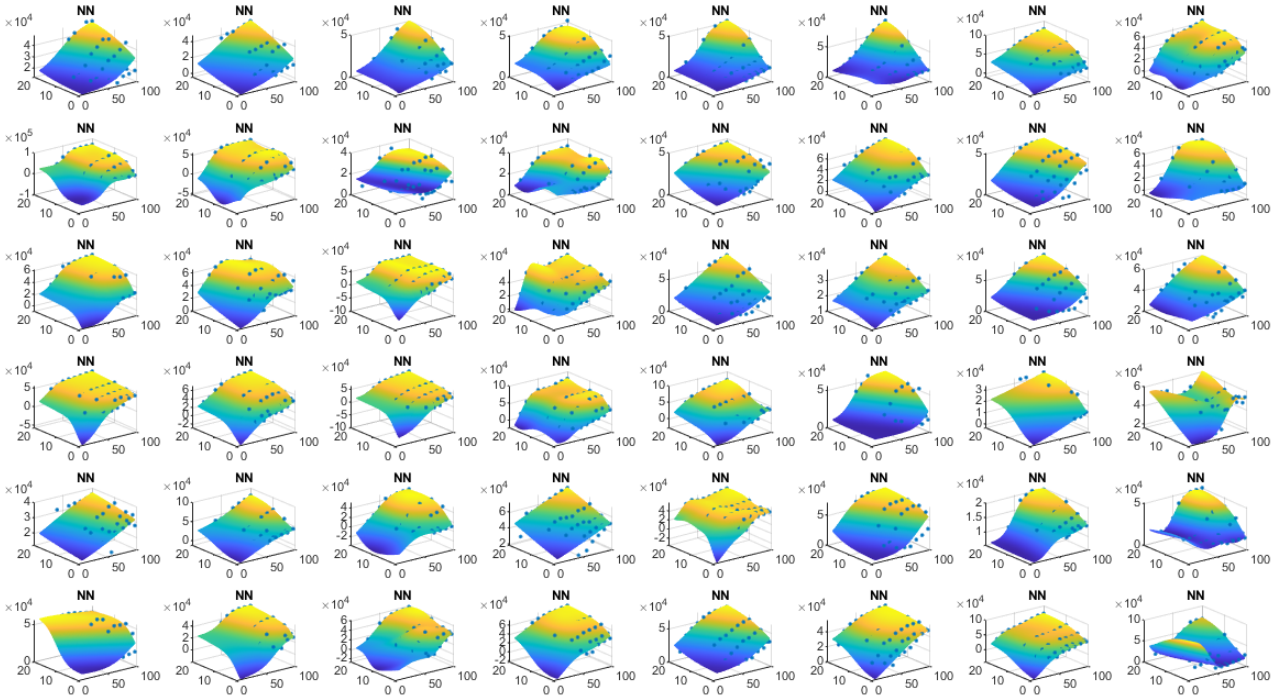

Figure 3. 1. Neural network models for area vs. pulse amplitude and type in all 48 retinal regions. The z-axes show area in pixels. X-axes and y-axes show pulse amplitude and type.

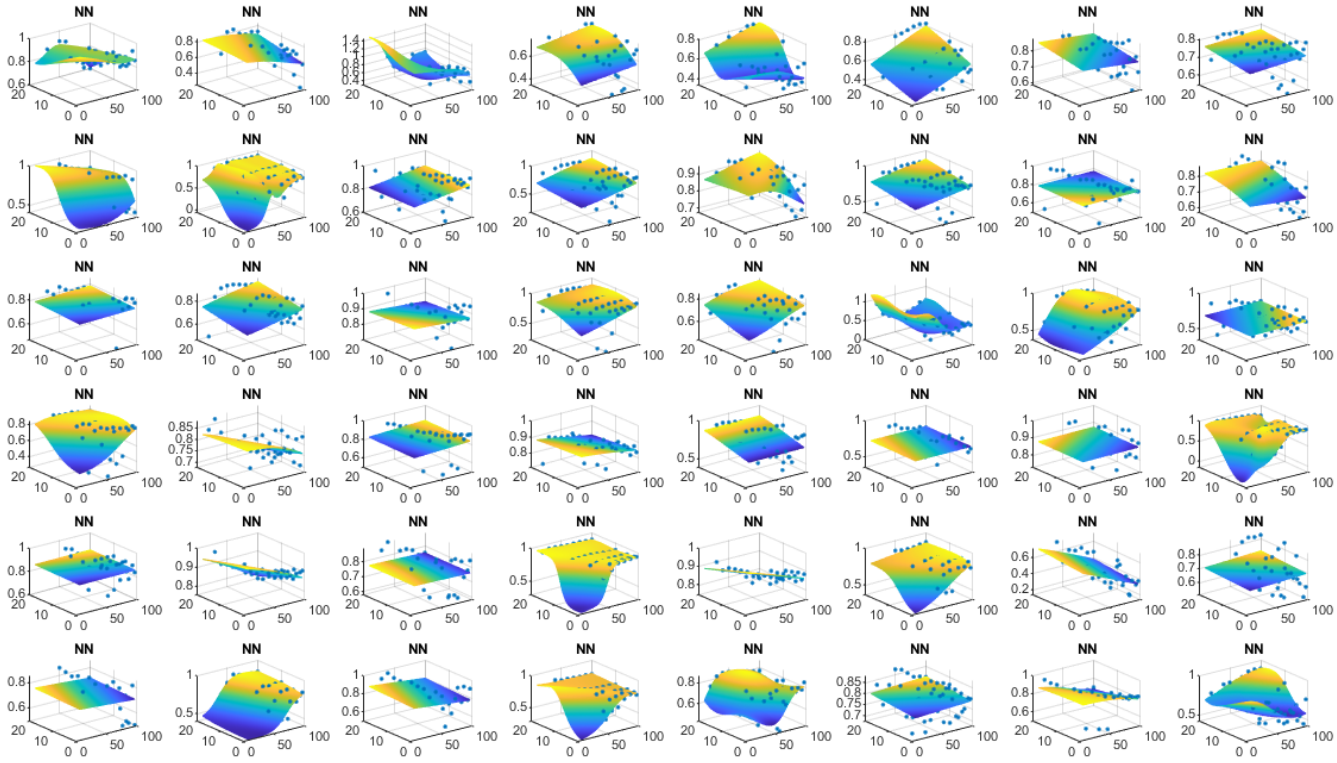

Figure 3. 2. Neural network models for eccentricity vs. pulse amplitude and type in all 48 retinal regions. The z-axes show eccentricity values. X-axes and y-axes show pulse amplitude and type.

functions. We used MATLAB built-in functions and the Levenberg-Marquardt backpropagation method for training the networks. Figure 3.1 and 3.2 show the fitted neural networks for area and eccentricity in all 48 retinal regions.

3.3.2. Closed-loop Search for Optimal Stimulation Parameters

The desired RGC activation has an area equal to the electrode area and eccentricity of zero (i.e. circular). A closed-loop optimization algorithm was developed to search for optimal stimulation parameters that elicit the desired RGC activity by minimizing the following objective function:

$$f(a,t) = |A(a,t) - C| + E(a,t) \qquad (1)$$

where A and E are activation area and eccentricity respectively as functions of pulse amplitude (a) and type (t). C is a constant representing the electrode area. Area values were normalized to the maximum of the RGC activation area in each region.

An interior point algorithm was used to find the minimum of the objective function in each region [189], [190], [167]. The algorithm combines line search and trust-region steps to decrease

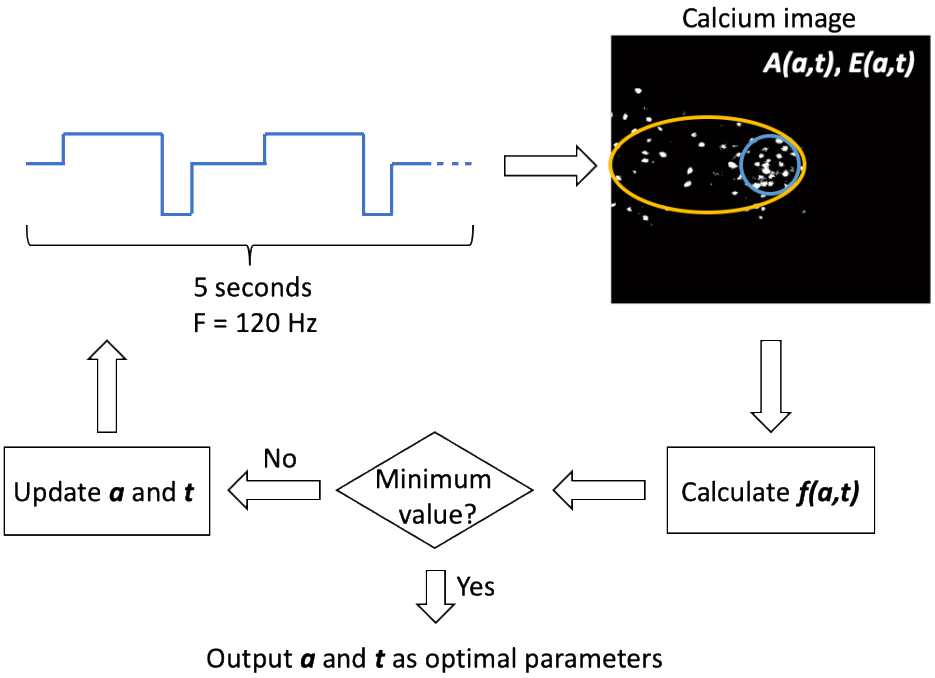

Figure 3. 3. Flow chart of the optimization process. Area and eccentricity values are calculated in each iteration in response to a combination of pulse amplitude and type (a and t). The objective function (f) is calculated based on area and eccentricity. The algorithm then determines if the minimum objective function value is achieved, and either updates a and t or ends the search accordingly. Note that the calcium imaging block translates into an ANN in the optimization process. Calcium image demonstrates the best-fit ellipse (yellow) and the electrode location (blue).

the objective function value. At each iteration the algorithm selects the next testing point based on the direction of change in the objective function value and stops searching when the minimum value of (1) is found. The FMINCON function from MATLAB optimization toolbox was used to implement this algorithm. Fig. 3.3 shows a summary of the parameter optimization process.

3.4. Results

3.4.1 Artificial Neural Network Training

Fig. 3.4. A-B show two examples of area and eccentricity maps as functions of pulse amplitude and type, and their resulting objective function. These examples demonstrate the different behavior of spatial RGC responses to the same range of stimulation parameters, and the need for developing an individual model for each region. Stimulation parameters that did not result

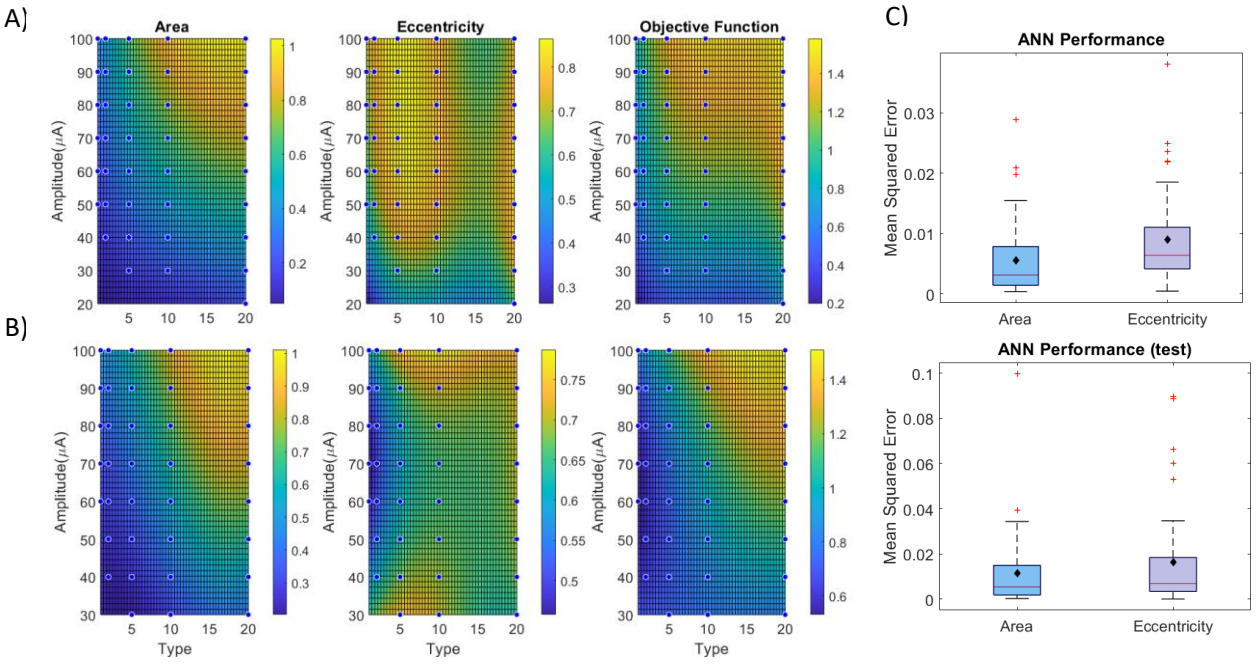

Figure 3. 4. ANN performance and examples. A,B) Two examples for area, eccentricity, and objective function maps as functions of pulse amplitude and type. The blue dots represent the experimental data points. Area values are normalized to the maximum area value in each region. Color bars do not have units since all values are normalized. C) ANN performance quantified as MSE across all data points (top), and test data points (bottom). Each box plot represents MSEs for 48 regions. Black diamonds show the mean value for each box plot and the red plus signs show the outliers.

in a calcium response were eliminated from the data points used for modeling. ANNs were created for activation area (A) and eccentricity (E), and the objective function was constructed based on (1). The performance of ANNs was quantified as the mean squared error (MSE) between the trained model and the experimental data points. The performances on all data points as well as on the test data set for all 48 regions are shown in Fig. 3.4 C.

3.4.2. Optimizing Stimulation Parameters for Focal RGC Activation

Optimization was performed individually in each region. The initial condition was chosen as the point with minimum value of pulse amplitude and type. Examples of the closed-loop search are shown in Fig. 3.5. An average of 8±5 iterations were required to converge to the optimal parameters for focal RGC activity. This number is much lower than 50 which is the number of parameter combinations tried experimentally to find the optimal parameters for focal activation.

The algorithm explores the continuous space fitted to the experimental data, therefore the optimal point found by the algorithm was not amongst the experimental data points in most cases. However, the calcium image resulting from the closest stimulation parameters to the optimal point was extracted and the corresponding images are shown for examples in Fig 3.5 These images show relatively focal RGC activities with only sparse axonal stimulation. This further confirms that the algorithm is effective in finding the optimal stimulus parameters for different regions with various

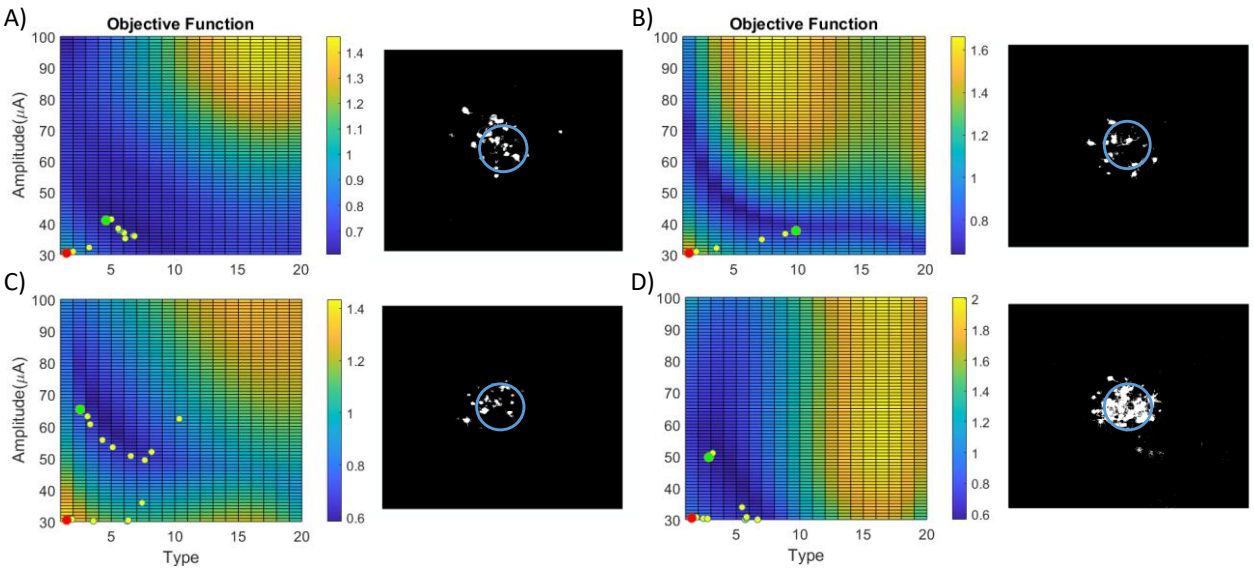

Figure 3. 5. A-D) Four examples of automatic closed-loop search for optimal parameters. The red dot is the starting point, the yellow dots represent the search points in intermediary iterations, and the green dot is the end point. Calcium image for the experimental data point closest to the end point is shown in front of each objective function example. Blue circles represent the electrode location.

response characteristics. Fig. 3.6 shows the optimal solutions for focal RGC activity for the 48 retinal regions.

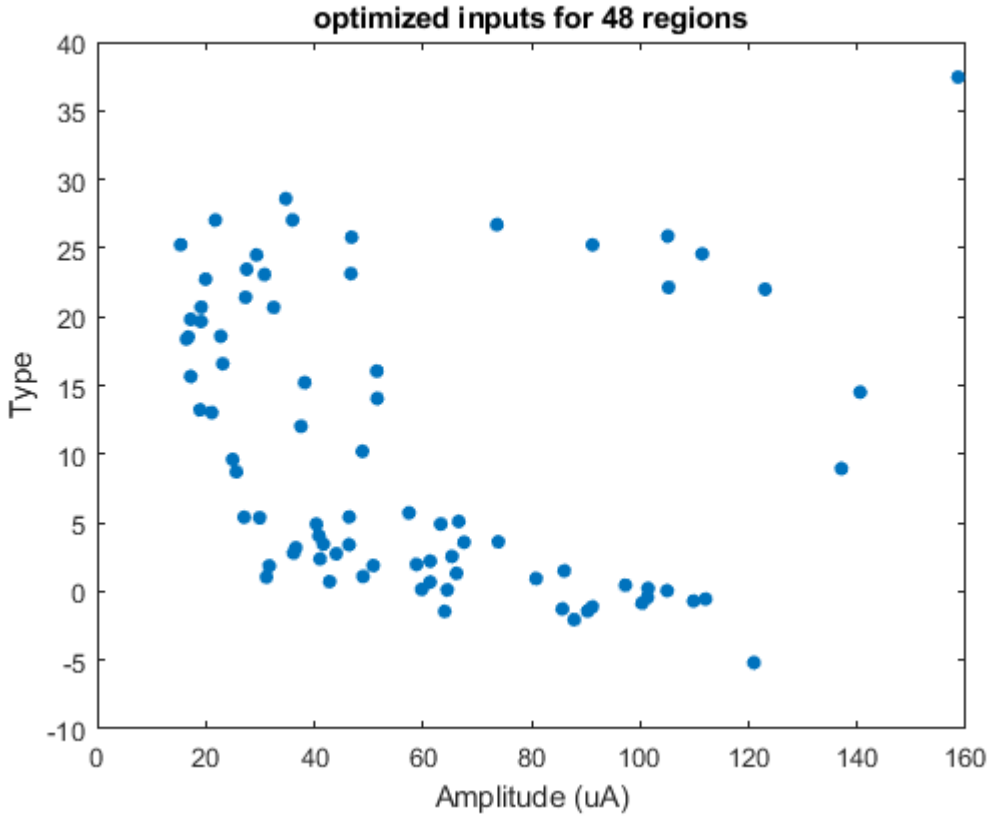

Figure 3. 6. Optimal stimulation parameters across 48 retinal regions.

3.5. Discussion

We have presented a method for automatic closed-loop searching of optimal stimulation parameters for the desired spatial response of RGCs. We have shown that an optimization algorithm can guide the parameter search effectively and find optimal parameters with a few iterations (8±5). This approach can reduce the exploration time significantly compared to a manual search, especially when the parameter space is large. We only used two pulse parameters to construct our objective function. Effectiveness of this algorithm should be tested for higher dimension parameter spaces (e.g. pulse width, frequency, inter-phase gap, etc.). In most regions

there were many parameter combinations that resulted in a low objective function and a near optimal solution. The final solution found by the algorithm is not necessarily the global minimum. Defining a range of acceptable area and eccentricity values will be helpful for future experiments. However, those values might vary across regions due to intrinsic differences between regions.

Our data indicated that RGC spatial activity can vary for different regions in response to the same stimulation parameters. This finding confirms the previous clinical studies with respect to phosphene shape inconsistency across different electrodes and subjects [74]. Future work includes performing *in vitro* calcium imaging of RGCs to verify this method. For real time optimization *in vitro*, this algorithm needs prior knowledge of the retinal response and local derivative information in order to select the next iterations effectively. Therefore, a few trials might be necessary to create a simple ANN or re-train the most similar model to our *in vitro* retina before proceeding with the optimization process. Models will be dynamically re-trained with each new recording to improve performance. This will increase the overall time for optimization, but will still allow fewer test conditions overall. Validation experiments will require a full parameter space search to ensure that an optimal result was reached when using a model based on a few trials. Algorithms that do not require prior knowledge of the system such as evolutionary algorithms and stochastic searching will also be considered for *in vitro* optimization. However, these methods generally require many iterations before converging to the optimal point. In this project, optimal stimulation parameters were identified using particle swarm optimization, and the average number of trials with this method was 53. In addition, the objective function had to be evaluated at every point in the parameter space at each iteration, adding to the total number of measurements needed *in vitro* and in clinic, which makes this method less efficient for optimization in these settings.

If applied clinically, the approach presented here could shorten the repetitive process of requiring users to draw phosphenes compared to a manual search for optimal parameters. The ANNs trained on *in vitro* data could be used as a starting point in human subject experiments, or new ANNs can be trained on a few drawings and dynamically re-trained over the course of optimization. Our prior work has shown that spatial activation patterns recorded during *in vitro* experiments and human perception of phosphene shape are influenced in a similar way by adjusting pulse parameters. Specifically, pulse durations greater than 20 ms created focal responses *in vitro* and smaller, rounder percepts in people [27]. Findings of this project could lead to the development of a clinically applicable system for electrode-specific optimization of stimulation protocol, improving the overall outcome of retinal prostheses.

Chapter 4: Real-time Optimization of Retinal Ganglion Cell Spatial Activity in Response to Epiretinal Stimulation

A version of this chapter has been submitted to IEEE Transactions on Neural Systems and Rehabilitation Engineering

Dorsa Haji Ghaffari, Akwasi D. Akwaboah, Ehsan Mirzakhalili, and James D. Weiland

4.1. Abstract

Retinal prostheses aim to improve visual perception in patients blinded by photoreceptor degeneration. However, shape and letter perception with these devices is currently limited due to low spatial resolution. Previous research has shown the retinal ganglion cell (RGC) spatial activity and phosphene shapes can vary due to the complexity of retina structure and electrode-retina interactions. Visual percepts elicited by single electrodes differ in size and shapes for different electrodes within the same subject, resulting in interference between phosphenes and an unclear image. Prior work has shown that better patient outcomes correlate with spatially separate phosphenes. In this study we use calcium imaging, *in vitro* retina, neural networks (NN), and an optimization algorithm to demonstrate a method to iteratively search for optimal stimulation parameters that create focal RGC activation. Our findings indicate that we can converge to stimulation parameters that result in focal RGC activation by sampling less than 1/3 of the parameter space. A similar process implemented clinically can reduce time required for optimizing implant operation and enable personalized fitting of retinal prostheses.

4.2. Introduction

Retinal implants help improve functional vision for patients blinded by retinal degenerative diseases such as age-related macular degeneration and retinitis pigmentosa [21], [22], [70]. Percepts are created by electrically stimulating the remaining cells of the retina, including retinal ganglion cells (RGC) and bipolar cells. Patients with implants report improvements in perceiving light, detecting motion, and following lines on the ground while walking. However, their ability to recognize shapes and letters is currently limited [77], [80]. The best visual acuity is reported as 20/1260 [99] for epiretinal and 20/460 [52] for subretinal implants, both of which are lower than the acuity level for legal blindness (20/200).

The ability to precisely stimulate target neurons and avoid off-target activation is critical to create focal, non-overlapping percepts. However, human subject testing has shown that a single electrode often elicits elongated percepts [10], and *in vitro* studies have demonstrated off-target stimulation of retinal ganglion cells, confirming the clinical results [26], [27]. Unintended axonal activation is an important factor that contributes to elongated responses and low resolution of retinal stimulation. Other factors include large electrode size, electric field spread [71], [187], and spatiotemporal interactions between electrodes [84]. Prior work has related visual acuity and other visual task performance metrics with two point resolution in retinal prosthesis patients [191]. Thus, creating focal percepts is important for better patient outcomes with artificial vision systems.

Previous studies have focused on modulation of stimulation parameters to avoid axonal activation. Some of these strategies include using long duration pulses [27], and low-frequency sinusoidal stimulations [90]. While successful at avoiding axonal activation, these protocols have not proven to be feasible clinically due to high threshold charge densities associated with long pulse durations. Our previous study showed that symmetric and asymmetric anodic-first pulses

with low duration ratios (ratio of anodic to cathodic phase duration) can preferentially activate RGC somas and reduce axonal activation. However subsequent clinical experiments did not show significant improvement in phosphene elongation with those pulses, which may be due to the limited parameter space explored in these tests [188]. In addtion to phosphene elongation, phosphene shapes and thresholds are highly inconsistent across electrodes and subjects [10]. This variability confirms that despite clinical use of retinal implants, the visual experience of patients is not adequately understood [74]. Contributing factors to these inconsistencies are variable electrode-retina separation, complex axonal pathways, heterogeneous degeneration, and perceptual interpretation of electrically elicited neural activity [93], [94]. Previous studies have shown that modifying stimulus parameters can transform the spatial RGC activity [26], and phosphene shapes [73]. Manually tuning each electrode is time consuming and tiring for patients, even when pulse shapes are limited to symmetric, biphasic pulses. Adding asymmetric pulses as an option will increase flexibility and may offer some benefits with respect to threshold and percept consistency, but this expands the parameter space to cover during a fitting procedure. Patient participation is required to confirm improvements in percept shape, but a prolonged fitting procedure will diminish the patient's willingness and ability to provide useful feedback. Therefore, there is a crucial need to make the fitting process as efficient as possible.

Optimization algorithms have been applied to aid clinical decision making for deep brain stimulation implants [192]. In this study, we demonstrate a process that optimizes RGC spatial activity. We developed neural network (NN) models of RGC spatial activity and a real-time optimization method to search for stimulation parameters that elicit focal responses from *in vitro* retina. Using this approach, we can rapidly identify stimulation parameters that produce a focal response based on sampling less than 1/3 of the possible pulse parameter combinations. A similar

process may be applicable to a clinical setting for efficiently tuning phosphene shape to improve the function of visual prostheses.

4.3. Methods

4.3.1. Overview

Wild-type mice C57BL/6 (n = 10) aged 3-4 weeks purchased from Envigo were used for calcium imaging experiments. Mice were injected with an adeno-associated virus (AAV) vector encoding a genetically encoded calcium indicator (GECI) 3 – 4 weeks prior to being euthanized for experiments. All procedures were approved by the Institutional Animal Care and Use Committee (IACUC) and the Institutional Biosafety Committee (IBC) at the University of Michigan.

4.3.2. Adeno-Associated Virus Vector (AAV) production

pGP AAV-CAG-Flex-JCaMP7f-WPRE (Addgene #104496) was obtained from Addgene. To make pGP-AAV-CAG-JGCaMP7f-WPRE 1 μg of the Addgene plasmid was incubated with 4 units of Cre Recombinase (New England Biolabs cat# M0298) for 30 minutes at 37 C. The Cre-plasmid reaction was then cleaned up using the Monarch® PCR and DNA clean up kit from New England Biolabs and resuspended in 35 μL of elution buffer. Two microliters of the cleaned-up Cre-plasmid reaction was then transformed into chemically competent NEB Stable bacteria using standard procedures and grown on LB Ampicillin plates. Colonies were picked and mini-prepped. The obtained clonally isolated DNA was then sequenced at the University of Michigan Advanced Genomics Core to identify a clone that had Cre mediated flipping of the pGP AAV-CAG-Flex-JCaMP7f-WPRE flex cassette. The resulting vector was named pGP-AAV-CAG-JGCaMP7f-WPRE. This vector is based on the AAV2 inverted terminal repeats (ITR). AAV2 has been reported to be best for labeling RGCs, as it transduces the largest number of cells after intravitreal

injection [136], [193]. CAG promoter in combination with AAV2 has been able to target the majority of RGCs in mammalian retina [194].

4.3.3. Intravitreal AAV injection

To transduce the GECI jGCaMP7f in RGCs, pGP-AAV-CAG-Flex-jGCaMP7f-WPRE (Addgene #104496) was obtained from Addgene (Watertown, MA). The plasmid was then modified by the University of Michigan Vector Core to create the final vector pGP-AAV-CAG-jGCaMP7f-WPRE. Mice were anesthetized with intraperitoneal injection of ketamine (100 mg kg^{-1}) and xylazine (10 mg kg^{-1}). Pupils were dilated with 1% tropicamide and 2.5% phenylephrine hydrochloride. Topical tetracaine hydrochloride was applied for local anesthesia. A pilot hole was created through the sclera, choroid, and retina 1 – 2 mm posterior to the corneal limbus using a 30-gauge needle. A 5 µl Hamilton syringe (Hamilton Robotics, Reno, NV) with a 32-gauge blunt needle was used to inject 1 µl (1.83 x 10^{12} vg/ml) of pGP-AAV-CAG-jGCaMP7f-WPRE in the vitreous area (between the lens and retina). Injection was done slowly over 30 seconds and left in place for another 30 seconds after injection and slowly retracted to minimize leakage. Antibiotic eye ointment was used on the injection site to prevent infection.

4.3.4. Calcium imaging

Retinas were harvested 3 – 4 weeks [26] after injecting pGP-AAV-CAG-jGCaMP7f-WPRE. Animals were anesthetized with ketamine (100 mg kg^{-1}) and xylazine (10 mg kg^{-1}). Both eyes were enucleated and hemisected inside a perfusion chamber filled with bicarbonate-buffered Ames' Medium (Sigma-Aldrich, St. Louis, MO). After removal of both eyes animals were euthanized by CO_2 overdose. Isolated retina was flattened by making four cuts on the periphery. Vitreous was removed with fine forceps to ensure tight coupling between retina and the microelectrode array (MEA). The MEA formed the bottom of the perfusion chamber. Retina was

then mounted on a porous membrane (cat. No. JVWP01300; Millipore) attached to a titanium ring and then placed on the transparent MEA with retinal ganglion cells facing the MEA. During the experiment, retina was superfused with bicarbonate-buffered Ames' Medium equilibrated with 5% CO_2 - 95% O_2 gas, and adjusted to 280 mOsm. Solution was kept at 33° C and had a flow rate of 4 – 5 ml min^{-1}. Fluorescence excitation was induced by a super bright white light emitting diode (LED). Excitation and emission light were passed through a filter set (49002 - ET - EGFP(FITC/Cy2), Chroma Technology Corp, Bellows Falls, VT) and images are captured by an electron-multiplied charge-coupled device (EMCCD) camera (iXon 897, Andor Technology, Belfast, Northern Ireland) through an inverted Olympus UPLFLN 0.3 numerical aperture (NA) ×10 objective at 10 Hz.

4.3.5. Electrical stimulation

A transparent microelectrode array (MEA) constructed from glass, indium tin oxide, silicon nitride, and SU-8 epoxy photoresist was used for electrical stimulation [26]. The MEA contained 60 disk electrodes with 200 μm diameter and 500 μm electrode pitch. Electrical stimulus pulses were generated by the PlexStim system (Plexon Inc., Dallas, Texas) controlled by a computer software. A custom circuit board was used to relay the electrical signal to the MEA. A platinum wire placed on top of the recording chamber was used as the return electrode. Stimuli consisted of charge balanced, biphasic, anodic-first current pulses delivered at 120 Hz for 5 seconds to evoke a calcium response. Five different pulse types were used in experiments: symmetric anodic-first, asymmetric anodic-first with duration ratio of 2, 5, 10, and 20. Duration ratio is defined as the ratio of the anodic phase to cathodic phase duration. Pulse amplitude range was 20 – 140 μA (with 10 μA increments) for the cathodic phase, and the anodic phase amplitude was calculated according

to the duration ratio to keep the pulse charge balanced. Cathodic phase duration was 100 μs in all experiments. A total of 46 pulse parameter combinations were used at each retinal region.

4.3.6. RGC spatial activity analysis

For each stimulation protocol, the fluorescence images around the active electrode were recorded at 10 fps. Images were captured for 5 seconds before and 5 seconds during electrical stimulation. The baseline image was obtained by averaging images 2 – 3 seconds after recording initiation, and the stimulation image was obtained by averaging images 2 – 3 seconds after stimulation initiation. RGC spatial activity was obtained by subtracting the baseline image from the stimulation image. The resulting calcium transient image (ΔF) was further normalized with respect to baseline (F), and a threshold was selected ($\Delta F/F > 15\%$) to remove noise based on the typical noise in the fluorescent signal. The shape of the RGC spatial activity (response shape) was quantified with two descriptors: activation area and eccentricity. Activation area was defined as the area of the best-fit ellipse to the RGC spatial activity, and eccentricity was defined as the ratio of the distance between the ellipse foci to its major axis length. Eccentricity values are always between 0 and 1 (0 is a circle and 1 is a line segment), and are a measure of response elongation.

4.3.7. Optimization pipeline overview

We use artificial neural networks (NN), a convolutional neural network (CNN), and an optimization algorithm to iteratively search the parameter space and classify activation area and eccentricity, to converge to the desired response shape. Two NNs, based on images recorded during the experiment, are used to estimate surfaces for activation area and eccentricity and the resulting objective function. The optimization routine uses the objective function surface to predict optimal stimulus parameters. We record the RGC spatial activity to the predicted optimal stimulus parameters and classify the resulting image using the CNN. The procedure ends if the required class is achieved, and continues otherwise. Fig. 4.1 illustrates a flow chart of the optimization steps.

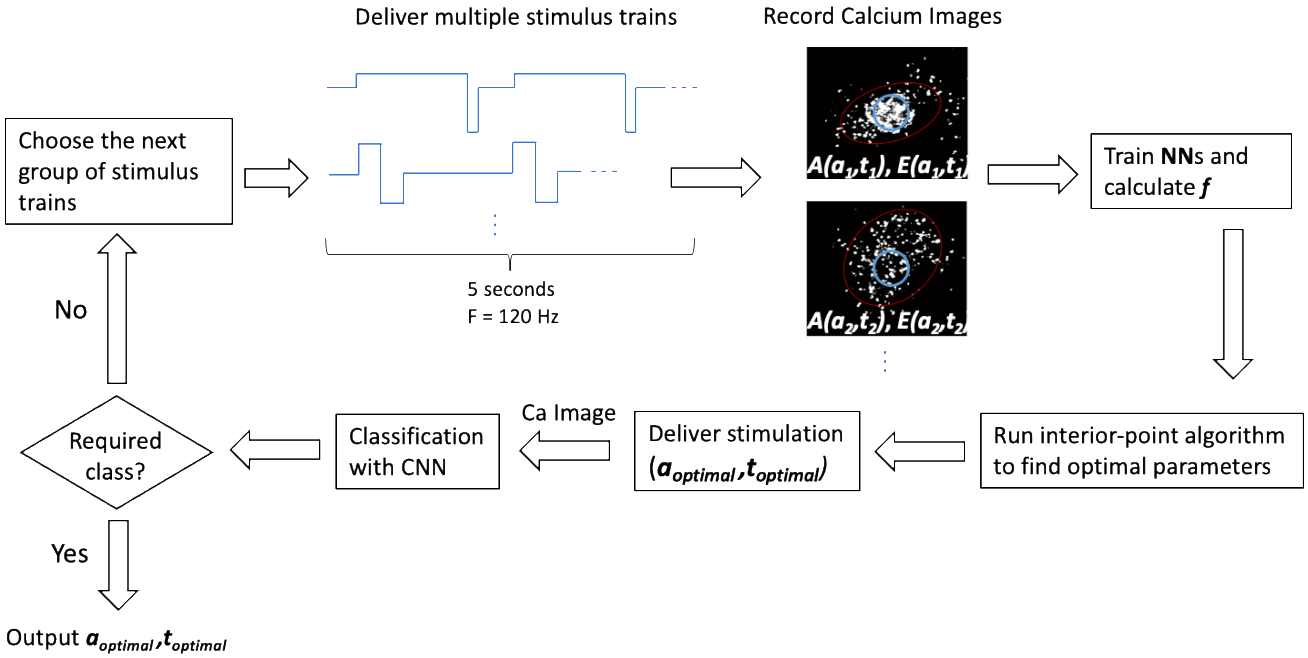

Figure 4. 1. Flow chart of the optimization process. A group of 5 different stimulus trains are delivered at the beginning. Calcium images of spatial RGC activity are recorded and analyzed for area and eccentricity values. Neural networks are trained for area and eccentricity as functions of pulse amplitude and type. Interior point algorithm is run to find optimal stimulation parameters for a focal response, which is then delivered to the retina and the resulting RGC spatial activity is recorded and classified by the CNN. If the image is classified as the required class, optimal amplitude and type are reported as outputs. Otherwise, the loop continues with 10, 15, 20, and 46 different stimulus trains. Blue circles show the electrode position on calcium images, and the best fit ellipse is outlined in red.

4.3.8. Neural network training

Based on our previous results on empirical modeling of RGC spatial activity [195],a single model could not be created for the relationship between stimulus parameters (pulse amplitude and type) and the spatial response descriptors (activation area and eccentricity) that was generalizable to all regions (a region is a retinal area above and nearby an electrode). Therefore, we chose to train feedforward artificial neural networks (NN) for each region separately to quantify this relationship. Data points were divided into three subsets for training (60-80%), validation (10-20%) and test (10-20%), where the exact percentage was determined by the number of data points. The network inputs are pulse amplitude and type, and outputs are activation area and eccentricity. The NNs include a hidden layer of size 10 with hyperbolic tangent transfer functions. We used MATLAB (MathWorks, Natick, MA) built-in functions and the Levenberg-Marquardt backpropagation method for training the networks.

4.3.9. Closed-loop search for optimal stimulation parameters

A closed-loop optimization algorithm was developed to find stimulation parameters that elicit the desired response shape by minimizing the following objective function:

$$f(a,t) = |A(a,t) - C| + E(a,t) \quad (1)$$

where A and E are activation area and eccentricity respectively as functions of pulse amplitude (a) and type (t), as estimated by the NNs. C is a constant representing the electrode area. Area values were normalized to the maximum value of the activation area for a given region. The

ideal response shape has an activation area equal to the electrode area and eccentricity of zero (i.e. circular).

An interior point algorithm was implemented in order to find the minimum of the objective function in each region [189], [190], [167]. The algorithm combines line search and trust-region steps to reduce the objective function value. At each iteration the next testing point is selected based on the direction of change in the objective function value and searching stops when the last step is smaller than the step tolerance (10^{-4}). The FMINCON function from MATLAB optimization toolbox was used to implement this algorithm.

In each retinal region we started by recording the fluorescent transient images in response to 5 different sets of stimulation parameters. These points were chosen by randomly selecting one amplitude (20 – 140 μA) for each pulse type. NNs for activation area and eccentricity were then trained on the images of RGC spatial activity and the objective function was created based on (1). The interior point algorithm was used to search for the minimum of the objective function and the optimal stimulation parameters. The next step was delivering a stimulus train with the predicted optimal parameters and recording the spatial RGC activity. In most cases the optimal parameters were modified to settings possible for delivery with the electrical stimulator. Similar steps were done on 10, 15, 20, (by randomly selecting 2, 3, 4 amplitudes per class) and 46 sets of stimulation parameters.

4.3.10. Convolutional neural network training for calcium image classification

Prior work using a database of previously recorded RGC spatial activity images [26] showed that in most regions there were many pulse parameters combinations that resulted in a near optimal solution, and the solution found by the algorithm was not necessarily the global minimum

of the objective function. Therefore, we created 5 different classes for response shape and used that as a measure of the desirability of the response shape elicited by the predicted optimal stimulus parameters. Initially, we categorized our images into 5 classes based on activation area and eccentricity values (Table 1). One metric that distinguishes different classes from each other is having an area larger or smaller than twice the electrode area. This metric was chosen because it determines whether the RGC activity overlaps with adjacent electrodes according to the electrode pitch in the MEA, which is similar to the pitch in Argus II implants. Another classification metric is having an eccentricity larger or smaller than 0.5. This number was chosen as the mid-point in the eccentricity range. Fig. 4.2 shows examples for each class of images. An initial total of 5466 images were labeled manually to more accurately distribute images into 5 classes: class 0 = no meaningful activity, class 1: round and focal response, class 2: elongated and focal response, class 3: round and large response, class 4: elongated and large response. Subsequent data augmentation to balance the number of images per class increased the total number to 8622. Data augmentation was implemented through orthogonal rotations, image flipping, and addition of gaussian and salt and pepper noise to classes 1, 2, and 3.

Convolutional neural network (CNN) architecture consisted of two convolutional layers each containing 32, 3×3 kernels and a subsequent rectified linear unit (ReLU) activation functions. Towards the end the network has 2 fully connected layers with 32 and 5 nodes respectively. The training protocol involved the use of ‘Adam’ [196] optimizer with categorical cross-entropy loss and learning rate of 0.001. A 20% dropout, L2-norm regularization ($\lambda = 0.0007$), and a batch size of 32 were used. Training-test data split was 90-10%, and a further 90-10% training-validation split was done on the training data. Training was done over 25 epochs while monitoring accuracy and loss performance metrics.

Table 4.1. Image Classification Information

Class	Area	Eccentricity	Initial number	Final number
0	No meaningful activity		2045	2045
1	< 2× electrode area	< 0.5	257	1559
2	< 2× electrode area	> 0.5	754	1438
3	> 2× electrode area	< 0.5	30	1200
4	> 2× electrode area	> 0.5	2380	2380

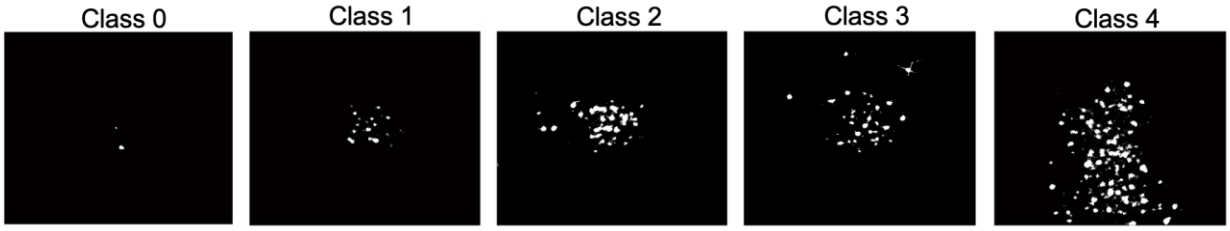

Figure 4. 2. Example images for each class. Class 0: no meaningful activity, class 1: round and small response, class 2: long and small response, class 3: round and large response, class 4: long and large response.

4.4. Results

4.4.1. In silico *prediction of optimal stimulus parameters with NNs based on RGC spatial activity data*

RGC spatial activity was obtained from 24 retinal regions during the experiments. Fig. 4.3 A – C shows three examples of objective function maps based on pulse amplitude and type. These examples demonstrate the variability of RGC spatial activity to the same range of stimulation parameters. Stimuli that did not result in a calcium response were not included in the data points used for modeling. NNs were created for activation area (A) and eccentricity (E), and the objective function was constructed based on (1). The performance of NNs was quantified as the mean squared error (MSE) between the trained model and the experimental data points. The

performances on the test data sets for all 24 retinal regions are shown in Table 2. The training time for NN and execution time for the interior point algorithm varied based on the amount of data and the number of iterations, respectively. But in general, these took less than 1 minute running on a standard desktop computer, without any attempt to optimize code.

Examples of interior point optimization are shown in Fig. 4.3. The initial condition was chosen as the point with minimum value of pulse amplitude and type. The interior point algorithm explores the continuous space fitted to the experimental data in each region, therefore the optimal point found by the algorithm was not amongst the experimental data points in most cases. Due to limitations in the resolution of the electrical stimulator, the optimal amplitudes and types were rounded to parameters within the stimulator capability. Example RGC spatial activity resulting from the closest stimulation parameters to the optimal point are shown in Fig. 4.3 for each corresponding objective function map. These images show relatively focal RGC activities with only sparse axonal stimulation. This confirms that the NNs and interior point algorithm are effective at finding the optimal stimulus parameters for different regions with various response characteristics.

Table 4.2. Neural Network Performance (MSE)

	5 points	**10 points**	**15 points**	**20 points**	**46 points**
Area	0.0655±0.1068	0.0690±0.1049	0.0513±0.0858	0.0442±0.0600	0.0361±0.0394
Eccentricity	0.0171±0.0228	0.0191±0.0408	0.0148±0.0332	0.0130±0.0182	0.0140±0.0205

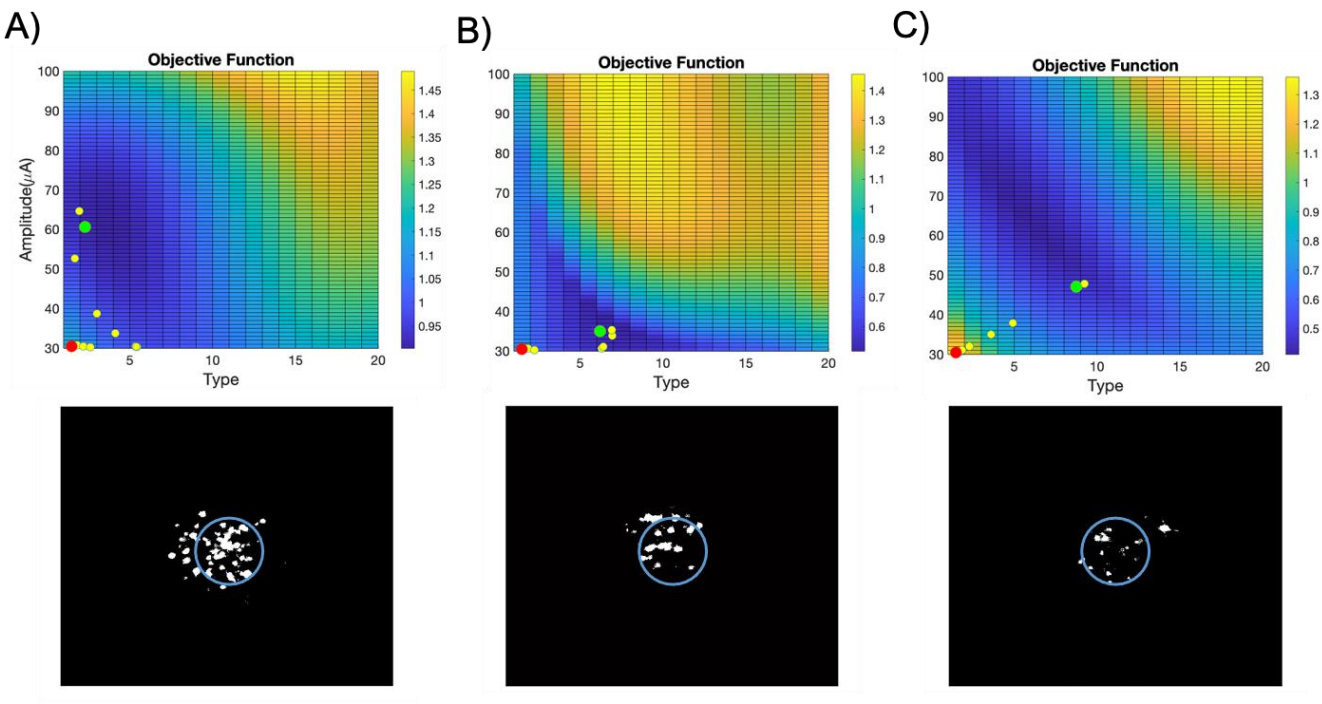

Figure 4. 3. A-C) Three examples of closed-loop search for optimal stimulation parameters. Objective function maps are plotted against pulse amplitude and type. The interior point algorithm is used to search for the optimal stimulus. Red dots represent the initial condition (lowest amplitude and class), yellow dots are the intermediary points, and green dots are the optimal points. Calcium images resulting from the optimal stimulation parameters are below each objective function map. All 46 calcium images were used to create these objective functions.

4.4.2. Real-time search for optimal stimulation parameters in vitro

Closed-loop optimization was performed in each region on objective function maps fitted to RGC spatial activity evoked by 5, 10, 15, 20 and 46 stimulus parameter combinations. As described in Fig. 4.1 and the previous section, the interior point algorithm predicted optimal stimulus parameters. Pulse parameters near the optimal settings were delivered to the retina and the RGC spatial activity was recorded. The CNN was used to classify the response shape evoked by both the randomly chosen stimulus parameters (used for NN training) and the predicted optimal stimulus parameters. The CNN performance was measured based on accuracy of predictions. Fig.

4.4 is a confusion matrix for true labels vs. prediction labels, showing the prediction accuracies ranging from 93 – 100%.

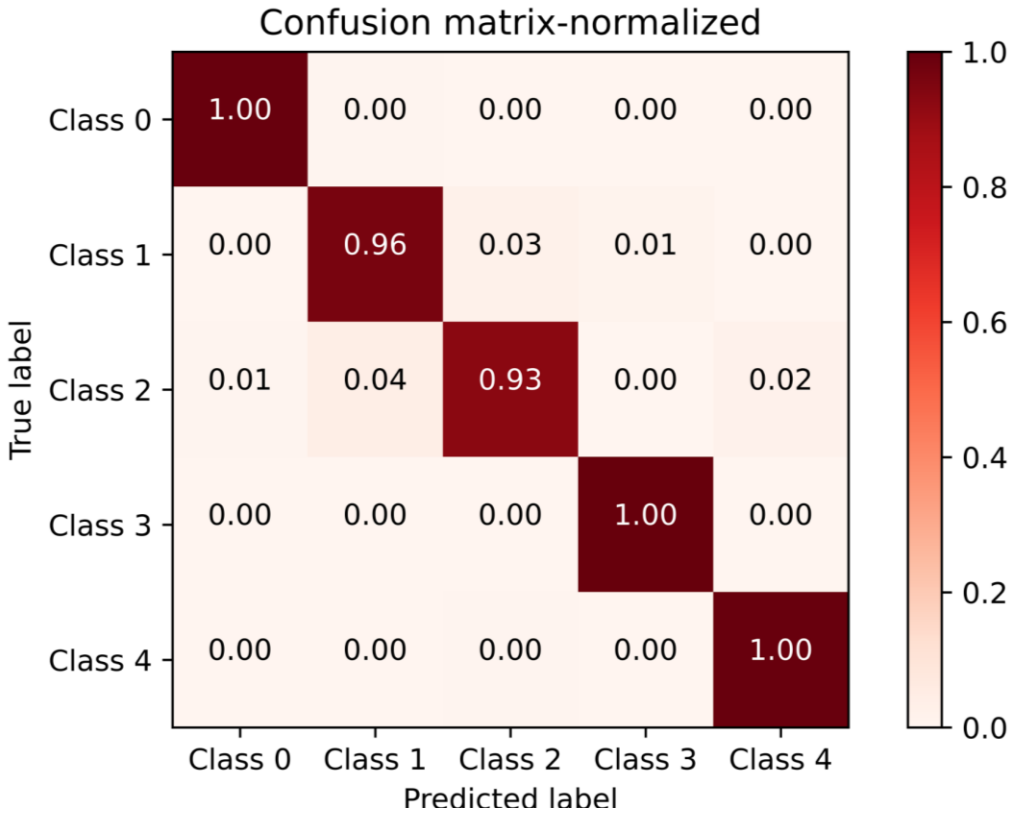

Figure 4. 4. Normalized confusion matrix for CNN accuracy. Individual class recognition rates are shown for test data. Accuracy values for correctly predicting each class are shown on the diagonal.

The CNN classification step determined if the search was completed or if the process should continue. Since our overall goal was to create a focal response area, class 1 is the most desirable class due to focal activation area and round shape. If the CNN classified the response shape as class 1, then the process was completed. Otherwise, a new set of data was collected with more data points. Class 2, 3, and 4 follow class 1 in terms of desirability. Class 0 means no meaningful activity in response to retinal stimulation. The best class in each retinal region was defined as the most desirable class achievable considering response areas across all stimuli. Class 1 was not always achievable, but all regions yielded either a class 1 or 2 response area using this range of parameters. Class 1 was reached in 7 out of 24 regions and Class 2 was reached in 17 out

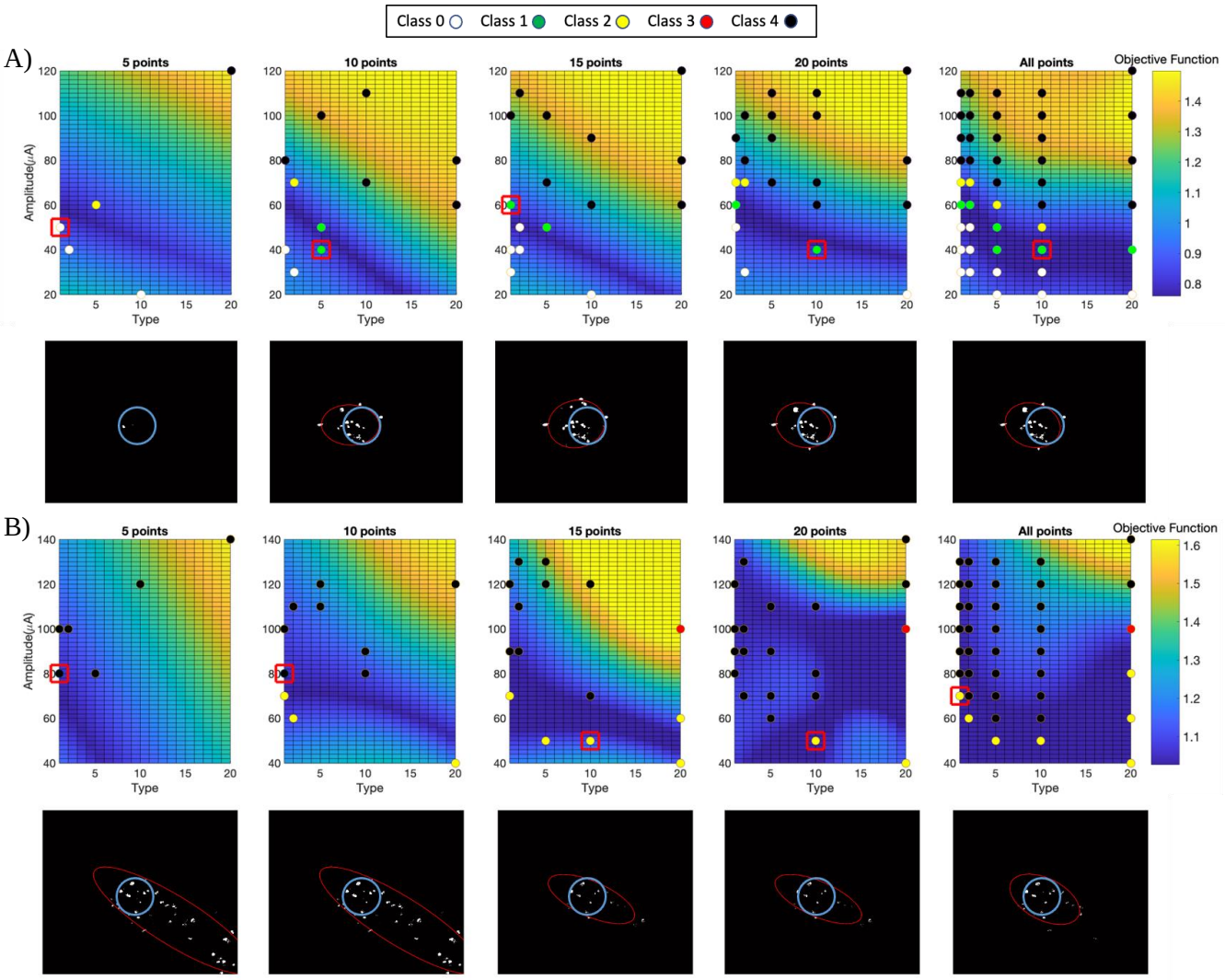

Figure 4. 5. Examples for objective function maps at different iterations and the resulting optimal solution and calcium image. Colored dots are the classified calcium images for every stimulus train delivered at each iteration. Red boxes designate the optimal solution found by the algorithm. Calcium image corresponding to the optimal solution is shown below each objective function map. A) At the first iteration (5 points), the algorithm is converging to a solution with class 0 spatial activity. At iterations 2-5 the algorithm is converging to a solution with class 1 spatial activity. B) At the first and second iterations, the algorithm is converging to solutions with class 4 spatial activity. At iterations 3-5 the algorithm is converging to a class 2 spatial activity, which is the best class possible based on all trials.

of 24 regions. Fig. 4.5 includes examples of the optimization process in two different retinal regions. The best possible class in these regions is 1 and 2 shown in Fig. 4.5A and Fig. 4.5B respectively. Best class was achieved after 10 and 15 trials in these examples. Fig 4.6. shows the possibility of getting best class vs. the number of trials. In all retinal regions, we achieved response

shape with the best class after 20 trials. The average and median number of trials for achieving best class was 10.

Figure 4.5 shows how the objective functions become more complex when more data is used to train the NN. Objective functions based on five points are simple, with gradients in one direction. As more data points are used to train the NN, the objective function surface becomes more complex. Figure 4.7 shows a boxplot of the number of trials needed to converge to best class across 24 retinal regions. Figure 4.8 shows the optimal stimulation parameters in all 24 regions, rounded to the closest value possible for delivery with the stimulator.

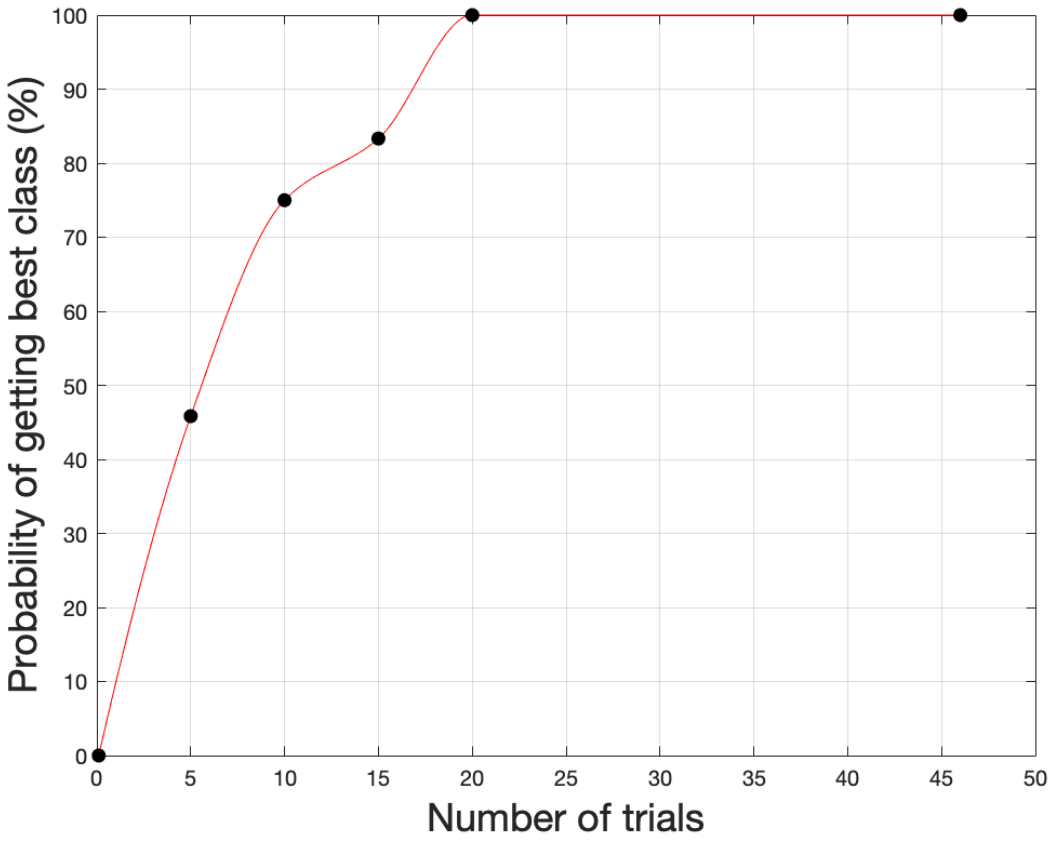

Figure 4. 6. Probability of converging to the best possible class. Maximum number of trials to get the best class is 20 across all retinal regions.

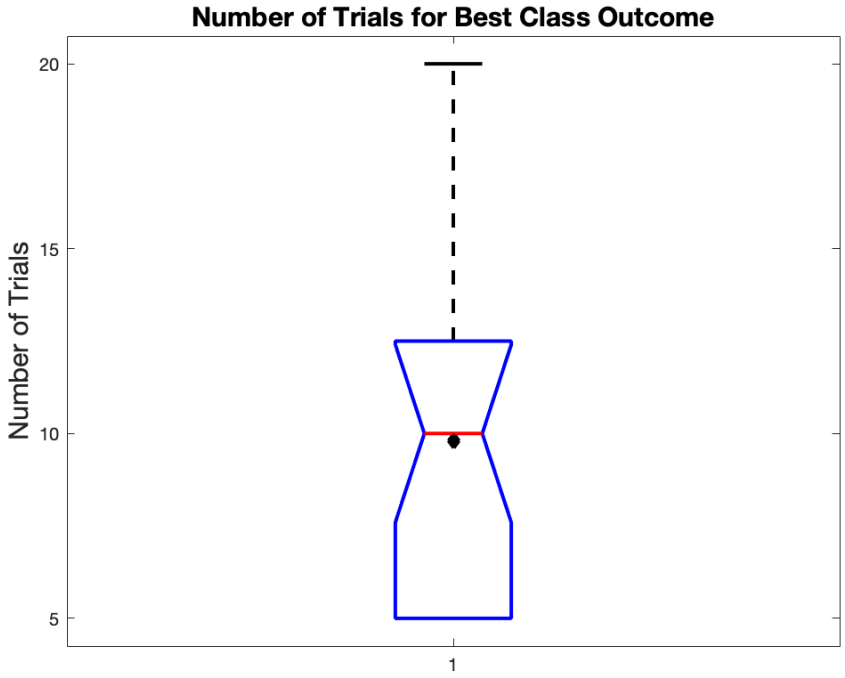

Figure 4. 8. Box plot of the number of trials needed to converge to best class across 24 retinal regions. The black diamond shows the average number of trials.

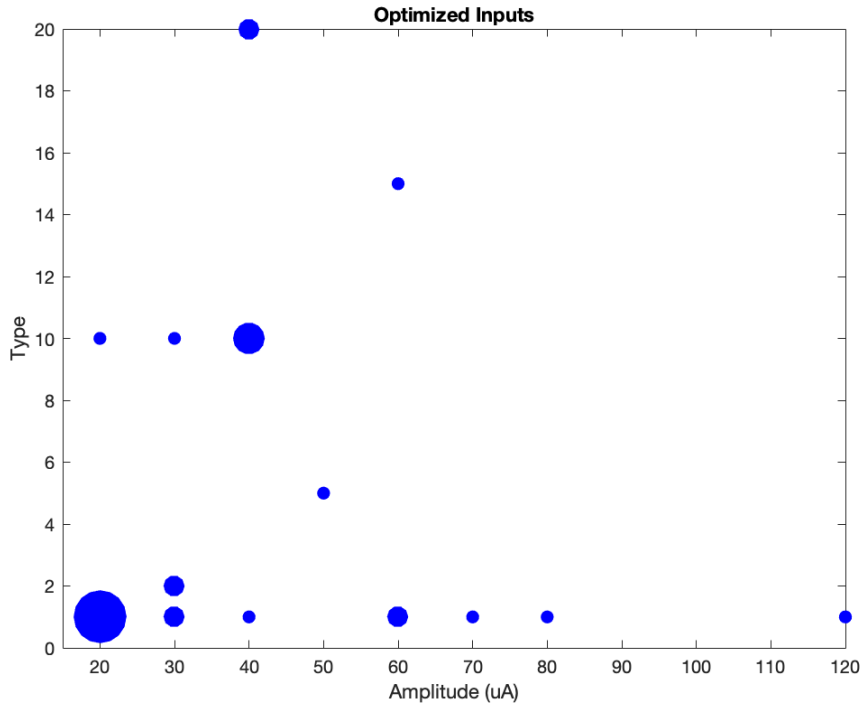

Figure 4. 7. Optimal stimulation parameters across 24 retinal regions. Size of the blue dots corresponds to the number of regions with the same optimal inputs. The optimized input values are graduated due to rounding to the closest value possible for delivery with the stimulator.

4.5. Discussion

We have presented a process for guided modification of epiretinal stimulation parameters to produce a focal RGC response area. Prior work in patients with Argus II retinal implants has shown the importance of increasing the focality of percepts. There has been a strong correlation between two point resolution and the grating visual acuity task; the higher the two point resolution, the better the visual acuity [191]. Further work established a link between visual acuity and performance on visually guided tasks, including line following, door finding, and letter recognition. Therefore, artificial vision can be improved by creating focal percepts from individual electrodes.

We have shown that we can iteratively search and classify response areas using two NNs, a CNN, and an optimization algorithm. With this approach we were able to converge to the best possible response shape in all 24 retinal regions within 20 trials. The average number of trials needed to converge to a class 1 or 2 response shape was 10. To validate our approach, we performed a full parameter space search to identify the most desirable class possible when considering the entire parameter space. This process can reduce the exploration time significantly compared to a manual search, especially when the parameter space is large. For our experiments, we limited the free parameters to only two: amplitude and type. We used anodic-first pulses in this study based on our results from a previous study demonstrating anodic-first pulses elicit more focal activity and avoid axonal stimulation compared to cathodic-first stimuli [26]. Other fixed parameters included cathodic pulse width (100 μs) and interphase gap (5μs). Increasing the number of free parameters makes a manual process less likely to succeed. However, a large parameter

space will also increase the time for a semi-automated optimization process like we demonstrate. In our process, we randomly selected pulse amplitudes for each of the five pulse types tested. If the desired class was not achieved, we randomly selected a new set of pulse parameters with five additional settings. A more efficient process may be able to use the prior set of data to inform the selection of the next set of parameters.

In most cases there were many parameter combinations that resulted in a near optimal solution. Therefore, we defined five distinct response shape classes to discretize the desirability of the solution. This approach provides the flexibility to choose any of the 5 classes as the desired outcome by modifying multiplying factors for area and eccentricity, and the *C* constant in the objective function. We did not optimize for pulse efficiency, only for shape. Other studies have focused on optimizing pulse parameters for stimulation efficacy and lower thresholds by modifying pulse duration and polarities, however these studies haven't optimized for spatial RGC activity [26], [197], [198]. Optimizing for efficiency can be added to our framework simply by selecting the most efficient of the several pulse types that create the most focal percept class. The optimal stimulation parameters predicted by the interior point algorithm were rounded to the nearest available parameter settings. The rounded settings sometimes were less optimal (as measured by the objective function value) than the original solution.

The choice of training a CNN was based on the need for a rapid execution time and to eliminate any error in the ellipse fitting process. CNNs have recently received significant attention due to their superior performance in computer vision tasks such as image segmentation and classification [199], [200]. These deep learning models are comprised of learnable convolution filters that significantly reduce input image dimensions while preserving characteristic features necessary for good decision making by the subsequently cascaded multi-layer neural network.

The interior-point algorithm needs prior knowledge of the retinal response and local derivative information in order to select the next iterations effectively. Therefore, fitting NNs to a set of images at each iteration was necessary. Algorithms that do not require prior knowledge of the system such as evolutionary algorithms and stochastic searching can also be considered for optimization. However, these methods require evaluating the objective function at every point in the parameter space at each iteration and generally require many iterations before converging to the optimal point [201], [202].

Our data indicated that RGC spatial activity can vary for different retinal regions in response to the same stimulation parameters. This finding in *in vitro* mouse retina confirms the previous clinical studies with respect to phosphene shape inconsistency across different electrodes and subjects [74]. Future work includes performing human subject testing to verify this method. If applied clinically, the approach presented here could shorten the repetitive process of requiring users to draw phosphenes compared to a manual search for optimal parameters. In place of calcium images, patient drawings [74] would be used to determine the focality of percepts. The NNs trained on *in vitro* data could be used as a starting point in human subject experiments, or new NNs can be trained on a few drawings and dynamically re-trained over the course of optimization. Our prior work has shown that spatial activation patterns recorded during *in vitro* experiments and human perception of phosphene shape are influenced in a similar way by adjusting pulse parameters. Specifically, pulse durations greater than 20 ms created focal responses *in vitro* and smaller, rounder percepts in people [27]. Findings of this project could lead to the development of a clinically applicable system for electrode-specific optimization of stimulation protocol, improving the overall outcome of retinal prostheses.

Chapter 5: Investigating temporal properties of retinal ganglion cell responses to asymmetric anodic-first pulses

A version of this chapter has been presented at the International Conference of the IEEE Engineering in Medicine and Biology Society (EMBC' 18)

5.1. Introduction

Retinal prosthetic implants have helped improve vision in blind patients with retinitis pigmentosa (RP) and age-related macular degeneration (AMD), two of the common retinal diseases that lead to loss of photoreceptor cells and eventual blindness [21][97][50]. Patients with retinal prostheses have reported improvement in their light perception and performing visual tasks; however, their ability to perceive shapes and letters is currently limited due to the low precision of retinal activation [77][80]. Patients with implants who can recognize letters take an average of more than 40 seconds to do so [77]. A clinical trial showed that among 30 patients with retinal prostheses, about half of the electrodes had activation thresholds above the acute stimulation safety limit [99]. Even with a direct contact between the macula and electrodes, an average of 10% of electrodes had thresholds above the acute stimulation safety limit [97][88]. Electrodes that have high activation thresholds cannot be used individually and are grouped with adjacent electrodes, effectively creating a larger electrode area and lowering the stimulation resolution. Therefore, it is critical to investigate stimulation parameters that lower activation thresholds as it could provide a wider range of stimulus intensities for safe retinal activation in clinic [100], decrease charge and power consumption [100][101], and improve the resolution.

In Chapter 2, we investigated the effect of asymmetric waveforms on perception thresholds by human subject testing and computational modeling. In our previous work, we studied RGC thresholds in response to asymmetric waveforms using calcium imaging [26]. While calcium imaging allows for recording of RGC activity from a large number of cells, it does not provide a high temporal resolution. Intracellular recording through patch clamping provides unmatched temporal resolution and offers more details on cellular level responses such as spike latencies. We used single cell electrophysiology to study RGC responses to different stimulation parameters, mainly asymmetric anodic-first pulses. We demonstrate that asymmetric waveforms decrease cell activation thresholds compared to symmetric stimuli.

5.2. Methods

5.2.1. Retina Preparation

Wild type mice (C57BL/6) were anesthetized by intraperitoneal injection of ketamine (100 mg/mL) and xylazine (20 mg/mL). Eyes were enucleated and hemisected using iris and spring scissors (F.S.T, Foster City, CA); after removing the lens, vitreous humor was removed from the surface of the retina using fine forceps (F.S.T, Foster City, CA), and retina was cut into four equal pieces. Dissection process was done inside the superfusion solution to maintain retina health and cell viability. Mice were then euthanized by CO_2 overdose, and bilateral pneumothorax as the secondary mean. The dissected retina piece was placed on a piece of lens paper, which was then held in place with a slice anchor (harp) in the recording chamber. The superfusion solution was composed of Ame's medium with sodium bicarbonate and glucose, bubbled with a 5%CO_2 / 95%O_2 gas mixture, and adjusted to 280 mOsm osmolality. The retina was continuously superfused with the solution at 33 °C throughout the experiments.

5.2.2. Electrical Stimulation and Recording

To ensure maximum current is directed through the retina and to limit the current shunting around it, a 1.5 mm hole is created at the center of the recording chamber and the ground electrode

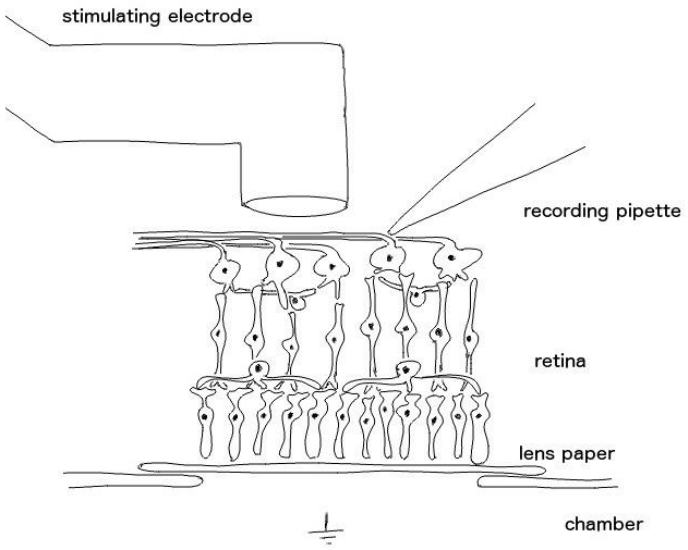

Figure 5. 1. Schematic of the stimulation and recording setup. (drawing is not to scale)

is placed under the hole in a smaller chamber. A ring of vacuum grease is applied around the hole to serve as an extra insulation, and the lens paper with the retina piece is placed on top of it [203]. Retina is placed ganglion cell side up with the external stimulating electrode placed 50 μm above it, and the ground electrode on the photoreceptor side (Fig. 5.1). STG-4008 stimulator and software from Multi-Channel Systems (Reutlingen, Germany) are used to deliver current pulses. Whole-cell patch clamp recordings are done using patch electrodes with tip resistances ranging 5-8 MΩ filled with internal solution containing (in mM): 111 K-gluconate, 5 NaCl, 4 KCl, 10 HEPES, 2 EGTA, 4 Mg-ATP, 0.3 Na-GTP, 7 Tris-phosphocreatine, 0.1% Lucifer Yellow, and KOH to 7.3

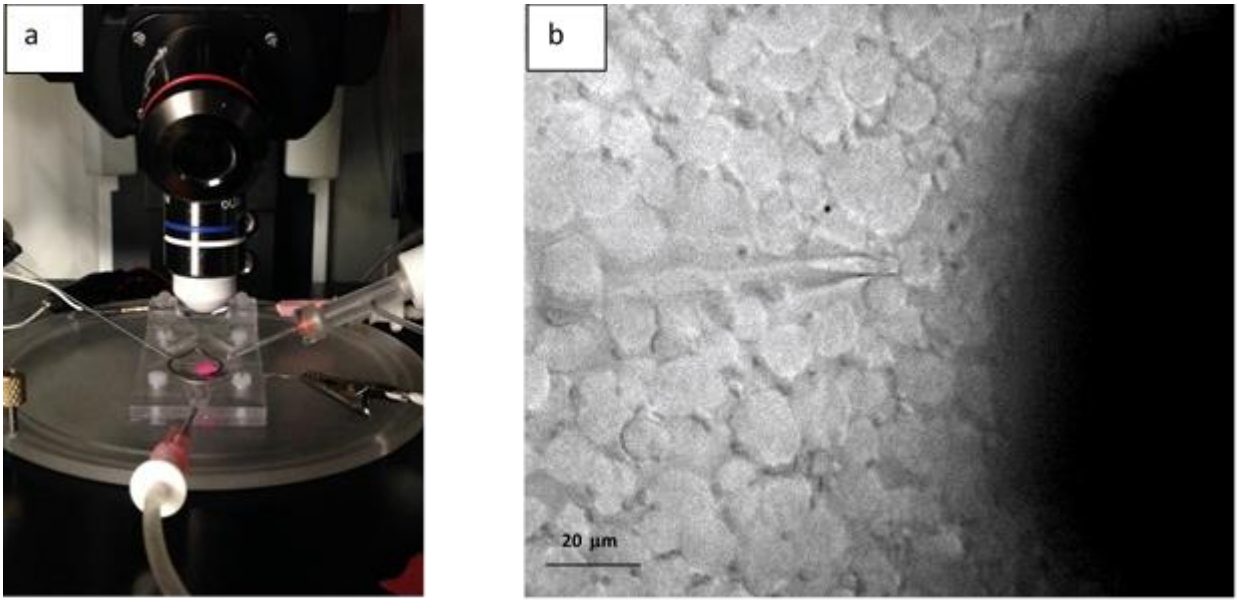

Figure 5. 2. (a)Stimulation/recording setup, (b)close-up image of whole-cell patch clamp recording with stimulation electrode on the right (dark shadow)

pH. Recordings are acquired and amplified using the Axopatch 200B amplifier and Clampex software.

5.2.3. RGC Threshold Measurement

Current pulses were delivered through the disk-shaped Platinum-Iridium electrode with 125 μm diameter, placed within 50 μm laterally from the targeted RGC. Three types of current pulses were used in experiments: symmetric cathodic-first, symmetric anodic-first, and asymmetric anodic-first with 5, 10, and 20 phase duration ratios. Pulse durations were 80 μs, 120 μs, and 500 μs. The two shorter pulses mainly lead to direct activation of RGCs and result in lower threshold charge densities, which provide flexibility in modifying the pulse amplitude [100][101]. Pulses were delivered at 10 Hz frequency to avoid desensitization of retinal neurons to repetitive stimuli [111][87]. Baseline activity of ganglion cells were recorded before delivering stimulation of each type (cathodic-first, anodic-first, asymmetric anodic-first) to ensure consistency. The baseline spontaneous spike rate was calculated as the probability of a spontaneous spike occurring

within 5 ms of the onset of the cathodic phase. The order of delivery of different current amplitudes was randomized to eliminate any threshold dependency on the direction of amplitude change. The activation threshold was defined as the amplitude at which an action potential is evoked in response to 50% of the total of 200 delivered pulses; if the spontaneous rate is not zero, the activation threshold is the midline between the spontaneous spike rate and 100% probability of evoking a spike. Only the spikes with their peaks occurring within 5 ms of the cathodic phase onset were counted as an evoked action potential since we were interested in direct activation of ganglion cells [55]. Dose-response curves were created for each pulse type for each cell by plotting the spike probability vs. current amplitude. Curves are fit using the logistic equation:

$$p = \frac{a}{b + e^{-xc}}$$

Where p is the spike probability, x is the current amplitude, and a, b and c are constants.

5.3. Results

Our results show an increase in spike probability when the stimulation amplitude is increased. Representative data for evoked spikes in an RGC within 5 ms of the cathodic phase onset of 200 anodic-first pulses is shown in Fig. 5.3.

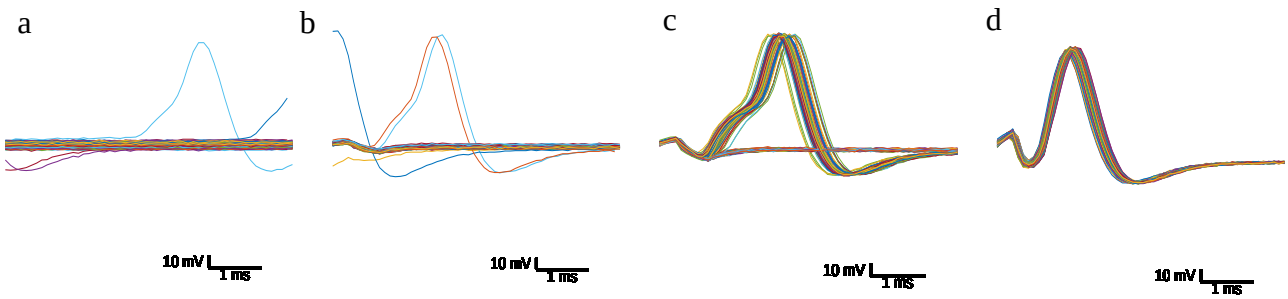

Figure 5. 3. Evoked action potentials in the 5 ms window after initiation of the cathodic phase of stimulus.(a)baseline activity (0.5 % spike probability). (b)20 uA- 0.5 ms anodic-first (1 % spike probability). (c) 40 uA- 0.5 ms anodic-first (41 % spike probability). (d) 100 uA- 0.5 ms anodic-first (100 % spike probability).

RGC activation thresholds were calculated from fitted graphs to spike probabilities for each pulse type and duration (Fig. 5.4a). Figure 5.4b shows a RGC baseline activity and response to different stimulation amplitudes for the 0.5 ms pulse duration. The liquid junction potential was calculated based on the ion concentrations, valences, and mobilities and was subtracted from the recorded membrane voltage. Stimulus artifacts are visible in the recordings for the 200 delivered pulses. Our data on 7 ganglion cells show a decrease in thresholds with the 10-time asymmetric anodic-first pulse compared to the symmetric cathodic-first and symmetric anodic-first stimulation (Fig. 5.5).

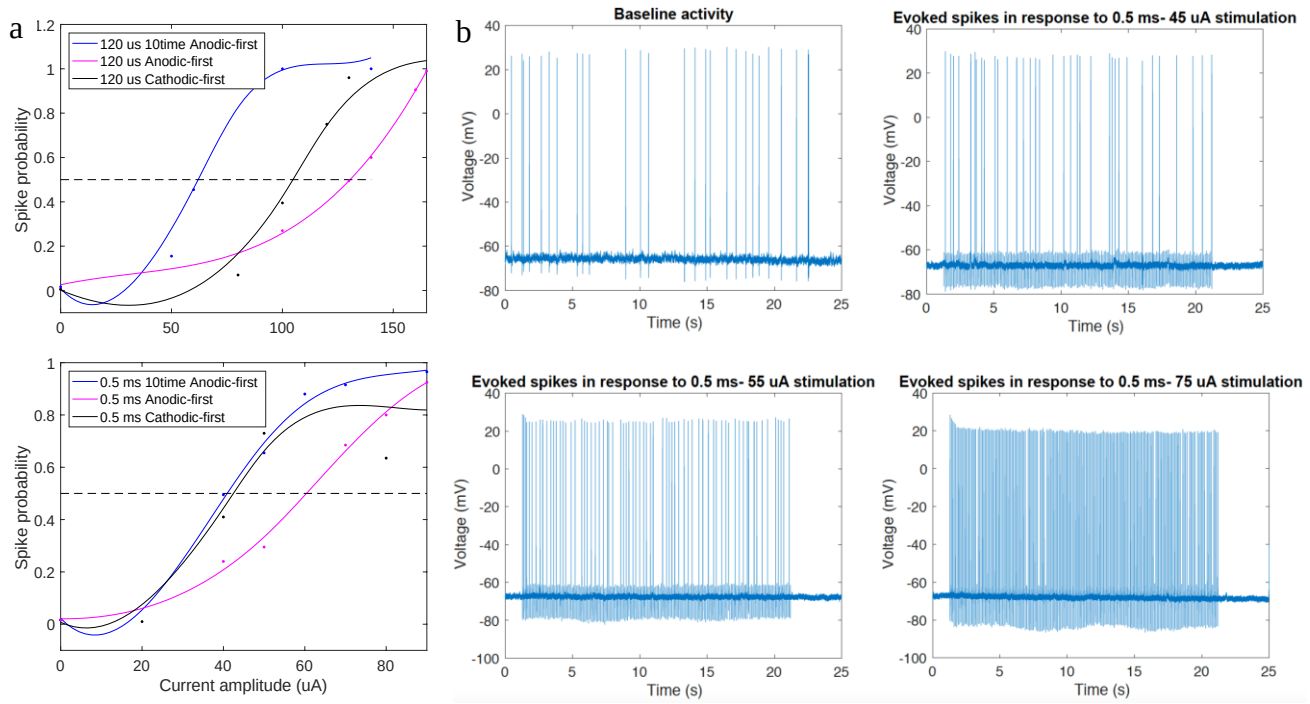

Figure 5. 5. (a) Dose response curves for 0.5 ms and 120 μs pulse durations, (b) Evoked action potentials in a RGC in response to different stimulation amplitudes.

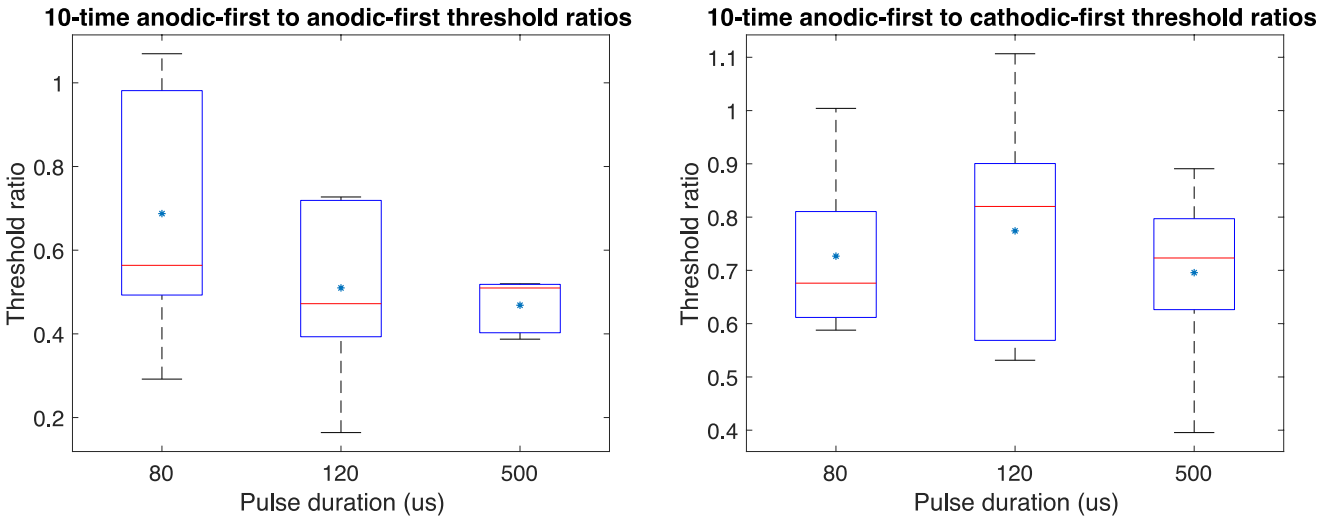

Figure 5. 4. Threshold ratios for different pulse durations. *Right:* box plots for threshold ratio of 10-time anodic-first to cathodic-first stimuli. *Left:* box plots for threshold ratio of 10-time anodic-first to anodic-first stimuli.

5.4. Discussion

In this study we determined that asymmetric anodic-first stimulation is effective in reducing activation thresholds in RGCs. We did not record from enough cells to perform a robust statistical analysis, but given that these findings are consistent with Chapter 2, we expect that data from more cells would confirm these results. For future experiments, cells should be categorized based on their dendritic morphology and light response into three groups of ON, OFF, and ON-OFF RGCs. Cell activation thresholds in these groups should be compared and the significance of threshold differences for the three pulse types should be studied separately in each group.

The asymmetric anodic-first stimulation may be decreasing cell thresholds based on anode-break excitation [26]. The amplitude range in which this pulse type can produce focal activation will determine its future practicality in clinic. We do not expect to see a significant difference between ON, OFF, and ON-OFF ganglion cell thresholds. It has been shown that with lower stimulation frequencies (5-10 Hz), the difference between ON and OFF ganglion cell activation thresholds is not significant [112]. However a significant difference between ON and OFF ganglion cell activation thresholds has been recorded in a study using high frequency (kHz) stimulation [167].

Studies have shown that adding interphase gaps equal to or greater than 0.5 ms reduces RGC thresholds by 20-25% [172] with cathodic-first biphasic pulses, as it delays the hyperpolarizing effect of the anodic phase. Adding an interphase delay to asymmetric anodic-first pulses, can reduce RGC thresholds possibly with a different mechanism. After applying a long hyperpolarization, the values of Hodgkin-Huxley parameters n and m are reduced while h is elevated. When the hyperpolarization is released, m quickly regains its normal value due to its very

short time constant (< 1 ms). But *n* and *h* take 3-10 ms to do so [176]. By having an interphase delay of less than 1ms, enough time is provided for the *m* value to go back to normal and make the net sodium current more than the potassium current, which can initiate an excitation. The relationship of the cell thresholds with the interphase delay duration is studied *in silico* in chapter 2. An electrophysiology experiment to investigate this phenomenon would involve delivering asymmetric anodic-first and cathodic-first stimulation and comparing RGC activation thresholds, as it is described in chapter 2. Different interphase gaps should be applied to the anodic-first stimuli to determine the optimal gap for lowering thresholds. For a more accurate understanding, single-channel patch clamp recordings could be performed to reveal the sodium and potassium channel dynamics over the course of stimulation.

Chapter 6: Discussion

6.1. Summary of Main Contributions

The main contributions of my dissertation are:

1. I demonstrated a reduction in perception thresholds in Argus II retinal prosthesis users, using asymmetric anodic-first pulses, and symmetric cathodic-first pulses with an interphase gap. (Chapter 2)
2. Biophysical modeling of an RGC confirmed the results from human subject testing. I extended the clinical results by testing a wide range of interphase gaps and duration ratios. I showed that pulses with small duration ratios (≤ 5) and long IPGs (≥ 2 ms), were predicted to be most effective for threshold reduction with short pulse widths (≤ 0.12 ms). Symmetric cathodic-first stimuli with IPGs longer than 0.5 ms, and asymmetric anodic-first pulses with large duration ratios (≥ 20) were predicted to be most effective for threshold reduction with 0.5 ms pulse widths. (Chapter 2)
3. I demonstrated a method for automatic closed-loop optimization of stimulation parameters to create focal RGC activity using an interior-point algorithm and neural network models. (Chapter 3)
4. I extended the optimization approach and demonstrated real-time optimization of stimulation *in vitro* for focal RGC activity. I was able to converge to the most focal response with an average of 10 trials. (Chapter 4)
5. I demonstrated a reduction in RGC activation thresholds with asymmetric anodic-first pulses in vitro using whole-cell patch clamp recordings. (Chapter 5)

6.2. Conclusion

Retinal prostheses have helped improve vision in patients blinded by retinal degenerative diseases such as RP and AMD. While patients with implants report improvements in light perception and performing visually guided tasks, their ability to perceive shapes and letters remains limited [77], [80]. The best reported visual acuity for epiretinal and subretinal prostheses is 20/1260 and 20/460 respectively [52], [99]. Unintended activation of axon fibers, and using electrodes in unison due to high individual thresholds are important contributing factors to low image resolution. The ability to precisely activate target neurons and avoid off-target activation is crucial to creating non-overlapping percepts and improving the prosthetic image quality [191]. In addition, reducing perception thresholds helps improve device efficiency and allows individual usage of electrodes, which is a necessary step for improving resolution. In this thesis I investigated a novel pulse paradigm for threshold reduction by performing a clinical study of retinal implant users, and computational modeling of a RGC, and *in vitro* retina studies. I also demonstrated a method for iterative searching for optimal stimulation parameters that create the most focal RGC activity *in silico*. Using this method, I created a framework for closed-loop optimization of stimulation parameters for focal RGC activity *in vitro*.

In Chapter 2, I investigated the effect of asymmetric waveforms and interphase gaps (IPG) on perception thresholds and shapes with epiretinal stimulation. Threshold measurements in Argus II implant users showed significant increase in perception probabilities in two out of three patients using AA and SCI stimuli compared to a standard symmetric cathodic-first pulse. Adding an IPG to the standard cathodic-first pulse increased perception probabilities significantly regardless of duration in one participant. Perception probabilities increased with the duration of IPG in the other

two participants, however not significantly. Adding an IPG to the AA pulse increased perception probabilities in one patient. Phosphene shape analysis revealed no significant difference between percept shape elongation with SC, SA, and AA stimuli. Average phosphene area was larger with AA stimulation compared to SC and SA. This difference was significant only for one participant. Our computational modeling study predicted lower activation thresholds with longer IPGs and higher duration ratio AA pulses. Combining AA stimulation with IPG showed that pulses with small duration ratios (≤ 5) and long IPGs (≥ 2 ms), were most effective in threshold reduction with short pulse widths (≤ 0.12 ms). Symmetric cathodic-first stimuli with IPGs longer than 0.5 ms, and asymmetric anodic-first pulses with large duration ratios (≥ 20) were predicted to be most effective for threshold reduction with 0.5 ms pulse widths. Our results suggest that incorporating asymmetric waveforms for retinal stimulation can improve the overall outcomes. Lower perceptual thresholds will improve device efficiency and battery life. In addition, it provides a wider dynamic range for stimulation amplitudes, and phosphene sizes and shapes. Lower thresholds will allow for individual usage of electrodes previously grouped with neighboring electrodes, and this potentially improves the overall image resolution. We expected less elongated phosphenes with short SA pulses based on our previous *in vitro* results [26]. We compared phosphene elongation only at one amplitude due to limitation in time. Since pulse amplitude can affect the elongation of spatial RGC activity, this comparison needs to be done at different amplitudes for a more thorough conclusion. Overall, our data demonstrates a need for flexible programming options in retinal implants. This will allow more flexibility for patient specific optimization of stimulation parameters [73], [204].

In Chapter 3, I demonstrated a method for automatic closed-loop optimization of stimulation parameters for focal RGC activity. This approach included training neural networks to quantify the relationship between stimulation parameters (pulse amplitude and type), and response

area descriptors (area and eccentricity), and using an interior point algorithm to minimize the objective function. We showed that the optimization algorithm can effectively find optimal parameters with few iterations (8±5). Calcium images corresponding to the parameters closest to the optimal parameters showed round and focal RGC activity with only sparse axonal stimulation. We used a gradient based algorithm that needs prior knowledge of the response and local derivative information to select the next iterations. Therefore, if this approach is used in real-time, fitting a continuous surface to a set of images at each iteration is necessary. Algorithms that do not require knowledge of the system such as stochastic searching and evolutionary algorithms require evaluating the objective function at every point in the population, and generally require many iterations before converging to an optimal solution [201], [202]. This study also indicated that spatial RGC activity, and the optimal parameters can vary greatly between different retinal regions, confirming the clinical studies' results with respect to phosphene shape inconsistency across electrodes and subjects [74]. The approach presented here can help create a framework for electrode-specific optimization of stimulation parameters for the desired percept shape.

In Chapter 4, I extended the work in Chapter 3 by utilizing the process for closed-loop optimization of stimulation parameters to converge to a focal RGC response *in vitro*. This process included training neural networks at each iteration based on a few images, using the interior point algorithm to find the optimal parameters, and classifying the resulting calcium images with a CNN trained on previous data. The average number of trials to converge to the most focal response was 10 across 24 retinal regions. This means that by sampling 10 out of 46 parameter settings, the process can select stimulus parameters that optimize spatial activity. This approach can shorten the exploration time significantly compared to a manual search, especially when the parameter space is large. If applied clinically, patient drawings would be used in place of calcium images to

determine the response focality [74]. This semi-automatic approach can shorten the repetitive process of drawing phosphenes compared to a manual search. Previous studies have shown a strong correlation between two point resolution (discernibility of two distinct phosphenes) and the grating visual acuity task [191]. And the visual acuity is predictive of the performance on visually guided tasks. Thus, by creating focal, non-overlapping phosphenes, this optimization approach can possibly improve the outcome of artificial vision.

In Chapter 5, I studied the effect of asymmetric anodic-first pulses on RGC thresholds. Whole-cell patch clamp recordings from 7 RGCs showed a decrease in thresholds with AA pulses with a duration ratio of 10, compared to SC and SA stimuli. This confirms our previous calcium imaging experiments [26], as well as human subject trials and computational modeling [188].

6.3. Future Directions

6.3.1. Asymmetric waveforms for retinal prostheses

Studies in Chapter 2 and 5 demonstrate that asymmetric waveforms are effective in reducing retinal response thresholds. Future work should continue to explore and optimize this type of stimulation. For single cell recordings, RGCs should be categorized based on dendritic morphology, light response, and labeling, where possible. To explore the effect of anode-break excitation on thresholds, AA and AC stimulation thresholds with different IPGs should be compared. Axonal stimulation is a major concern in epiretinal stimulation [27], [74]. To study the effect of SA and AA pulses on axon fiber activation, axon visualization methods such as transgenic mice expressing enhanced Green Fluorescent Protein (GFP) or AAV injection must be used [139], [205]. Clinical trial results must be validated on a larger number of participants. Effect of AC stimulation on perception thresholds must be studied in retinal implant users. Phosphene shapes in response to SA and AA stimulation must be studied at various amplitudes for a more thorough

conclusion [26]. AA pulses with low duration ratios and long IPGs were most effective in threshold reduction according to our computational model. This type of pulse need to be tested on human subjects to verify its effectiveness. If adding an IPG to a low duration ratio AA stimulation maintains focal response, this pulse type can possibly offer great potential for both threshold reduction and creating focal percepts [26]. However, due to intrinsic variabilities between different retinal regions and retinal implant users, the specific stimulation parameters need to be optimized for each electrode. In future studies, intersubject differences such as the position of implant, electrode-retina distance, and the amount of retinal degeneration could be considered to explain percept variabilities.

6.3.2. Automatic optimization of stimulation parameters

Studies in Chapter 3 and 4 demonstrate a process for automatic optimization of stimulation parameters to produce a focal RGC response area. We only used two stimulation parameters (pulse amplitude and type). Other parameters, such as pulse width, IPG, and frequency could be included in future studies to provide a more comprehensive framework for optimization. However, having a large parameter space will likely increase computation time for training neural networks and searching for optimal parameters using the interior point algorithm. Pulse efficiency is another important factor that should be added to this optimization framework [140], [197], [198]. This can be done by selecting the most efficient of several optimal parameters for focal RGC activity, or modifying the objective function to include a factor for the amount of charge delivered. We used an *in vitro* retina model to simulate the response to a retinal implant. Although useful, this model does not fully mimic an epiretinal implant. The MEA in a human subject, as opposed to the *in vitro* MEA, is not perfectly attached to the retina due to the eye curvature. The implant can also rotate and reposition after the surgery [206]. This creates varying distributions of electrical field,

thresholds, and percept shapes with identical stimuli. Previous research studies also show that chronic stimulation may result in change of neural activity [207]–[209]. These factors are not accounted for in the *in vitro* retina model. *In vivo* retinal implant models can possibly simulate the retinal anatomy and pathophysiology more accurately. Functional calcium imaging of the retina has been realized using two-photon imaging and genetically encoded calcium indicators [210], [211]. Future work should also include performing human subject testing to verify the optimization method. Instead of calcium images, patient drawings should be used to determine the focality of percepts [74]. This process can be improved by a more informed selection of initial parameters instead of randomly selecting them.

6.3.3. Future visual prostheses

An ideal retinal implant should create small, round, and focal percepts for each active electrode in order to provide a high resolution image. I demonstrated a method for automatic optimization of stimulation parameters *in vitro* and *in silico* to create focal RGC activity. While RGC response maps are good predictors of phosphene shape, they oversimplify a more complex problem. The *in vitro* recording setup does not account for a realistic electrode-retina distance, response desensitization, and threshold adaptation. In addition, retinal and cortical reorganization can affect the spatiotemporal properties of percepts. These factors contribute to even more variability in spatial response, compared to the *in vitro* setup. Therefore, an automatic process for electrode-specific optimization of stimulation parameters is necessary for retinal prostheses to succeed. Electrode arrays with the capability to stimulate and record from the retina simultaneously, can possibly decrease the optimization time in clinic.

Epiretinal prostheses should permit symmetric and asymmetric stimulation with the flexibility to modify pulse width and order of polarities. I showed that asymmetric pulses increase

the perception probability significantly compared to symmetric pulses. This effect was more pronounced with short pulse durations ($\leq$ 0.12 ms) based on my RGC model. Short pulses also provide other advantages such as high frequency stimulation, less axonal activation, and requiring less charge, making it easier to remain within electrochemical safety limits. Therefore, the capability of generating short pulse widths with retinal implants is needed, as part of a strategy that provides a more flexible fitting process and improve the overall outcomes.

Regardless of the anatomical placement, visual prostheses face similar challenges in capturing visual information, image processing, data and power delivery, and biocompatibility. No device has shown significant advantage over other systems. Resolution of artificial vision is limited by the electrode size and density, fading of percepts, and visual encoding processes. In addition, variations in disease severity, health of retinal neurons, and electrode-retina contact result in inconsistent outcomes. However, there has been considerable progress in the field over the past decades through innovation and collaboration. Some groups such as Nano Retina have focused on improving the electrode-retina contact by designing 3D electrodes with nano-coated tips. This may reduce stimulation thresholds and artifacts, but penetrating the retina might lead to greater surgical complications. The approaches presented in this thesis can possibly be applied to existing retinal implants to increase the stimulation resolution through electrode-specific optimization of stimulation parameters. Overall, visual prostheses hold great potential for improving vision for blind patients, and overcoming the limitations relies on collaborations between engineering, medicine and patients.

Bibliography

[1] H. Wässle, “Parallel processing in the mammalian retina,” *Nature Reviews Neuroscience*. 2004.

[2] C. A. Curcio, K. R. Sloan, R. E. Kalina, and A. E. Hendrickson, “Human photoreceptor topography,” *J. Comp. Neurol.*, 1990.

[3] R. R. A. Bourne *et al.*, “Global Prevalence of Blindness and Distance and Near Vision Impairment in 2020: progress towards the Vision 2020 targets and what the future holds.,” vol. 61.

[4] K. M. Gehrs, J. R. Jackson, E. N. Brown, R. Allikmets, and G. S. Hageman, “Complement, age-related macular degeneration and a vision of the future,” *Archives of Ophthalmology*. 2010.

[5] D. T. Hartong, E. L. Berson, and T. P. Dryja, “Retinitis pigmentosa,” *Lancet*. 2006.

[6] A. I. Den Hollander *et al.*, “Mutations in a human homologue of Drosophila crumbs cause retinitis pigmentosa (RP12),” *Nat. Genet.*, 1999.

[7] S. P. Daiger, L. S. Sullivan, and S. J. Bowne, “Genes and mutations causing retinitis pigmentosa,” *Clinical Genetics*. 2013.

[8] W. L. Wong *et al.*, “Global prevalence of age-related macular degeneration and disease burden projection for 2020 and 2040: A systematic review and meta-analysis,” *Lancet Glob. Heal.*, 2014.

[9] S. G. Jacobson and A. V. Cideciyan, “Treatment Possibilities for Retinitis Pigmentosa,” *N. Engl. J. Med.*, 2010.

[10] E. L. Berson, “Retinitis pigmentosa: The Friedenwald lecture,” *Investigative Ophthalmology and Visual Science*. 1993.

[11] P. Gouras, R. E. Carr, and R. D. Gunkel, “Retinitis pigmentosa in abetalipoproteinemia: Effects of vitamin A.,” *Invest. Ophthalmol.*, 1971.

[12] E. L. Berson, “Nutrition and retinal degenerations,” *International Ophthalmology Clinics*. 2000.

[13] S. Russell *et al.*, “Efficacy and safety of voretigene neparvovec (AAV2-hRPE65v2) in patients with RPE65-mediated inherited retinal dystrophy: a randomised, controlled, open-label, phase 3 trial,” *Lancet*, 2017.

[14] C. J. Simon, J. A. Sahel, J. Duebel, S. Herlitze, and D. Dalkara, “Opsins for vision restoration,” *Biochem. Biophys. Res. Commun.*, 2020.

[15] V. Busskamp, S. Picaud, J. A. Sahel, and B. Roska, “Optogenetic therapy for retinitis pigmentosa,” *Gene Therapy*. 2012.

[16] M. E. McClements, F. Staurenghi, R. E. MacLaren, and J. Cehajic-Kapetanovic, "Optogenetic Gene Therapy for the Degenerate Retina: Recent Advances," *Frontiers in Neuroscience*. 2020.

[17] D. Maberley, "Pegaptanib for neovascular age-related macular degeneration.," *Issues Emerg. Health Technol.*, 2005.

[18] A. D. Penman, K. W. Crowder, and W. M. Watkins, "Photodynamic Therapy of Subfoveal Choroidal Neovascularization in Age-Related Macular Degeneration with Verteporfin," in *50 Studies Every Ophthalmologist Should Know*, 2020.

[19] W. Rhoades, D. Dickson, and D. V. Do, "Potential role of lampalizumab for treatment of geographic atrophy," *Clinical Ophthalmology*. 2015.

[20] F. G. Holz *et al.*, "Efficacy and safety of lampalizumab for geographic atrophy due to age-related macular degeneration: Chroma and spectri phase 3 randomized clinical trials," *JAMA Ophthalmol.*, 2018.

[21] E. Zrenner, "Fighting blindness with microelectronics," *Science Translational Medicine*. 2013.

[22] J. D. Weiland, W. Liu, and M. S. Humayun, "Retinal prosthesis.," *Annu. Rev. Biomed. Eng.*, 2005.

[23] E. Zrenner, "Will retinal implants restore vision?," *Science*. 2002.

[24] E. Bloch, Y. Luo, and L. da Cruz, "Advances in retinal prosthesis systems," *Ther. Adv. Ophthalmol.*, 2019.

[25] N. L. Opie, A. N. Burkitt, H. Meffin, and D. B. Grayden, "Heating of the eye by a retinal prosthesis: Modeling, cadaver and in vivo study," *IEEE Trans. Biomed. Eng.*, 2012.

[26] Y. C. Chang, D. H. Ghaffari, R. H. Chow, and J. D. Weiland, "Stimulation strategies for selective activation of retinal ganglion cell soma and threshold reduction," *J. Neural Eng.*, 2019.

[27] A. C. Weitz *et al.*, "Improving the spatial resolution of epiretinal implants by increasing stimulus pulse duration," *Sci. Transl. Med.*, vol. 7, no. 318, 2015.

[28] A. Horsager *et al.*, "Predicting visual sensitivity in retinal prosthesis patients," *Investig. Ophthalmol. Vis. Sci.*, 2009.

[29] M. Mahadevappa, J. D. Weiland, D. Yanai, I. Fine, R. J. Greenberg, and M. S. Humayun, "Perceptual thresholds and electrode impedance in three retinal prosthesis subjects," *IEEE Trans. Neural Syst. Rehabil. Eng.*, 2005.

[30] D. Yanai, J. D. Weiland, M. Mahadevappa, R. J. Greenberg, I. Fine, and M. S. Humayun, "Visual Performance Using a Retinal Prosthesis in Three Subjects With Retinitis Pigmentosa," *Am. J. Ophthalmol.*, 2007.

[31] L. DaCruz *et al.*, "Patients blinded by outer retinal dystrophies are able to identify letters using the Argus TM II retinal prosthesis system," *Invest. Ophthalmol. Vis. Sci.*, 2010.

[32] A. K. Ahuja *et al.*, "Blind subjects implanted with the Argus II retinal prosthesis are able to improve performance in a spatial-motor task," *Br. J. Ophthalmol.*, 2011.

[33] R. Hornig, T. Zehnder, M. Velikay-Parel, T. Laube, M. Feucht, and G. Richard, “The IMI Retinal Implant System,” in *Artificial Sight*, 2007.

[34] G. Richard, R. Hornig, M. Keseru, and M. Feucht, “Chronic Epiretinal Chip Implant in Blind Patients With Retinitis Pigmentosa: Long-Term Clinical Results,” *ARVO Meet. Abstr.*, 2007.

[35] R. Eckmiller, D. Neumann, and O. Baruth, “Tunable retina encoders for retina implants: Why and how,” in *Journal of Neural Engineering*, 2005.

[36] R. Hornig *et al.*, “Pixium Vision: First Clinical Results and Innovative Developments,” in *Artificial Vision*, 2017.

[37] P. Walter, “A Fully Intraocular Approach for a Bi-Directional Retinal Prosthesis,” in *Artificial Vision*, 2017.

[38] M. Schloesser *et al.*, “Embedded device for simultaneous recording and stimulation for retina implant research,” in *Proceedings of IEEE Sensors*, 2013.

[39] S. Klauke *et al.*, “Stimulation with a wireless intraocular epiretinal implant elicits visual percepts in blind humans,” *Investig. Ophthalmol. Vis. Sci.*, 2011.

[40] B. W. Jones and R. E. Marc, “Retinal remodeling during retinal degeneration,” *Experimental Eye Research*. 2005.

[41] R. E. Marc, B. W. Jones, C. B. Watt, and E. Strettoi, “Neural remodeling in retinal degeneration,” *Progress in Retinal and Eye Research*. 2003.

[42] S. K. Kelly *et al.*, “Developments on the Boston 256-channel retinal implant,” in *Electronic Proceedings of the 2013 IEEE International Conference on Multimedia and Expo Workshops, ICMEW 2013*, 2013.

[43] Shire DB, “Advanced hermetic feedthrough and packaging technology for the boston retinal prosthesis,” *Investig. Ophthalmol. Vis. Sci.*, 2014.

[44] A. Y. Chow, V. Y. Chow, K. H. Packo, J. S. Pollack, G. A. Peyman, and R. Schuchard, “The Artificial Silicon Retina Microchip for the Treatment of Vision Loss from Retinitis Pigmentosa,” *Arch. Ophthalmol.*, 2004.

[45] A. Y. Chow, A. K. Bittner, and M. T. Pardue, “The artificial silicon retina in retinitis pigmentosa patients (an american ophthalmological association thesis),” *Trans. Am. Ophthalmol. Soc.*, 2010.

[46] M. T. Pardue *et al.*, “Possible sources of neuroprotection following subretinal silicon chip implantation in RCS rats,” in *Journal of Neural Engineering*, 2005.

[47] M. T. Pardue *et al.*, “Neuroprotective effect of subretinal implants in the RCS rat,” *Investig. Ophthalmol. Vis. Sci.*, 2005.

[48] A. Bhardwaj, S. Som, and S. K. Muttoo, “HS1-RIV: Improved efficiency for authenticated encryption,” *Int. J. Eng. Technol.*, 2018.

[49] K. Stingl *et al.*, “Subretinal Visual Implant Alpha IMS - Clinical trial interim report,” *Vision Res.*, 2015.

[50] K. Stingl *et al.*, “Artificial vision with wirelessly powered subretinal electronic implant

alpha-IMS," *Proc. R. Soc. B Biol. Sci.*, 2013.

[51] K. Stingl *et al.*, "Interim results of a multicenter trial with the new electronic subretinal implant alpha AMS in 15 patients blind from inherited retinal degenerations," *Front. Neurosci.*, 2017.

[52] D. Palanker, Y. Le Mer, S. Mohand-Said, M. Muqit, and J. A. Sahel, "Photovoltaic Restoration of Central Vision in Atrophic Age-Related Macular Degeneration," in *Ophthalmology*, 2020.

[53] Y. Mandel *et al.*, "Cortical responses elicited by photovoltaic subretinal prostheses exhibit similarities to visually evoked potentials," *Nat. Commun.*, 2013.

[54] H. Lorach *et al.*, "Performance of photovoltaic arrays in-vivo and characteristics of prosthetic vision in animals with retinal degeneration," *Vision Res.*, 2015.

[55] D. Boinagrov, S. Pangratz-Fuehrer, G. Goetz, and D. Palanker, "Selectivity of direct and network-mediated stimulation of the retinal ganglion cells with epi-, sub- and intraretinal electrodes," *J. Neural Eng.*, vol. 11, no. 2, 2014.

[56] J. D. Loudin, S. F. Cogan, K. Mathieson, A. Sher, and D. V. Palanker, "Photodiode circuits for retinal prostheses," in *IEEE Transactions on Biomedical Circuits and Systems*, 2011.

[57] A. E. Hadjinicolaou, H. Meffin, M. I. Maturana, S. L. Cloherty, and M. R. Ibbotson, "Prosthetic vision: Devices, patient outcomes and retinal research," *Clinical and Experimental Optometry*. 2015.

[58] L. M. Parver, C. R. Auker, and D. O. Carpenter, "Choroidal Blood Flow: III. Reflexive Control in Human Eyes," *Arch. Ophthalmol.*, 1983.

[59] Y. Yamauchi *et al.*, "Comparison of electrically evoked cortical potential thresholds generated with subretinal or suprachoroidal placement of a microelectrode array in the rabbit," in *Journal of Neural Engineering*, 2005.

[60] L. N. Ayton *et al.*, "First-in-human trial of a novel suprachoroidal retinal prosthesis," *PLoS One*, 2014.

[61] N. C. Sinclair *et al.*, "The appearance of phosphenes elicited using a suprachoroidal retinal prosthesis," *Investig. Ophthalmol. Vis. Sci.*, 2016.

[62] M. A. Petoe *et al.*, "Determining the Contribution of Retinotopic Discrimination to Localization Performance With a Suprachoroidal Retinal Prosthesis," *Invest. Ophthalmol. Vis. Sci.*, 2017.

[63] L. N. Ayton *et al.*, "A prototype suprachoroidal retinal prosthesis enables improvement in a tabletop object detection task," *Invest. Ophthalmol. Vis. Sci.*, 2015.

[64] C. J. Abbott *et al.*, "Safety studies for a 44-channel suprachoroidal retinal prosthesis: A chronic passive study," *Investig. Ophthalmol. Vis. Sci.*, 2018.

[65] G. J. Suaning, N. H. Lovell, and T. Lehmann, "Neuromodulation of the retina from the suprachoroidal space: The Phoenix 99 implant," in *IEEE 2014 Biomedical Circuits and Systems Conference, BioCAS 2014 - Proceedings*, 2014.

[66] T. Fujikado *et al.*, "Testing of semichronically implanted retinal prosthesis by

suprachoroidal-transretinal stimulation in patients with retinitis pigmentosa," *Investig. Ophthalmol. Vis. Sci.*, 2011.

[67] T. Fujikado *et al.*, "One-year outcome of 49-channel suprachoroidal–transretinal stimulation prosthesis in patients with advanced retinitis pigmentosa," *Investig. Ophthalmol. Vis. Sci.*, 2016.

[68] T. Endo, T. Fujikado, M. Hirota, H. Kanda, T. Morimoto, and K. Nishida, "Light localization with low-contrast targets in a patient implanted with a suprachoroidal–transretinal stimulation retinal prosthesis," *Graefe's Arch. Clin. Exp. Ophthalmol.*, 2018.

[69] A. P. Finn, D. S. Grewal, and L. Vajzovic, "Argus II retinal prosthesis system: A review of patient selection criteria, surgical considerations, and post-operative outcomes," *Clinical Ophthalmology*. 2018.

[70] M. S. Humayun *et al.*, "Pattern electrical stimulation of the human retina," *Vision Res.*, 1999.

[71] C. De Balthasar *et al.*, "Factors affecting perceptual thresholds in epiretinal prostheses," *Investig. Ophthalmol. Vis. Sci.*, 2008.

[72] S. H. Greenwald, A. Horsager, M. S. Humayun, R. J. Greenberg, M. J. Mcmahon, and I. Fine, "Brightness as a function of current amplitude in human retinal electrical stimulation," *Investig. Ophthalmol. Vis. Sci.*, 2009.

[73] D. Nanduri *et al.*, "Frequency and amplitude modulation have different effects on the percepts elicited by retinal stimulation," *Investig. Ophthalmol. Vis. Sci.*, 2012.

[74] M. Beyeler, D. Nanduri, J. D. Weiland, A. Rokem, G. M. Boynton, and I. Fine, "A model of ganglion axon pathways accounts for percepts elicited by retinal implants," *Sci. Rep.*, 2019.

[75] M. S. Humayun *et al.*, "Preliminary 6 month results from the argus™ II epiretinal prosthesis feasibility study," in *Proceedings of the 31st Annual International Conference of the IEEE Engineering in Medicine and Biology Society: Engineering the Future of Biomedicine, EMBC 2009*, 2009.

[76] J. A. Sahel *et al.*, "Subjects Blind From Outer Retinal Dystrophies Are Able To Consistently Read Short Sentences Using The ArgusTM Ii Retinal Prosthesis System," *ARVO Meet. Abstr.*, 2011.

[77] L. Da Cruz *et al.*, "The Argus II epiretinal prosthesis system allows letter and word reading and long-term function in patients with profound vision loss," *Br. J. Ophthalmol.*, 2013.

[78] L. da Cruz *et al.*, "Five-Year Safety and Performance Results from the Argus II Retinal Prosthesis System Clinical Trial," *Ophthalmology*, 2016.

[79] Y. C. Chang and J. D. Weiland, "Stimulation strategies for selective activation of retinal ganglion cells," in *International IEEE/EMBS Conference on Neural Engineering, NER*, 2017, pp. 345–348.

[80] E. Zrenner *et al.*, "Subretinal electronic chips allow blind patients to read letters and combine them to words," *Proc. R. Soc. B Biol. Sci.*, 2011.

[81] YC Chang, “Manipulation of RGCs Response Using Different Stimulation Strategies for Retinal Prosthesis,” 2017.

[82] H. Kasi, W. Hasenkamp, G. Cosendai, A. Bertsch, and P. Renaud, “Simulation of epiretinal prostheses - Evaluation of geometrical factors affecting stimulation thresholds,” *J. Neuroeng. Rehabil.*, vol. 8, no. 1, 2011.

[83] D. Palanker, A. Vankov, P. Huie, and S. Baccus, “Design of a high-resolution optoelectronic retinal prosthesis,” in *Journal of Neural Engineering*, 2005.

[84] A. Horsager, R. J. Greenberg, and I. Fine, “Spatiotemporal interactions in retinal prosthesis subjects,” *Investig. Ophthalmol. Vis. Sci.*, 2010.

[85] W. Tong *et al.*, “Minimizing axon bundle activation of retinal ganglion cells with oriented rectangular electrodes,” *J. Neural Eng.*, 2020.

[86] A. P. Fornos *et al.*, “Temporal properties of visual perception on electrical stimulation of the retina,” *Investig. Ophthalmol. Vis. Sci.*, 2012.

[87] D. K. Freeman and S. I. Fried, “Multiple components of ganglion cell desensitization in response to prosthetic stimulation,” *J. Neural Eng.*, 2011.

[88] A. K. Ahuja *et al.*, “Factors Affecting Perceptual Threshold in Argus II Retinal Prosthesis Subjects,” *Transl. Vis. Sci. Technol.*, 2013.

[89] D. Nanduri, “Prosthetic vision in blind human patients: Predicting the percepts of epiretinal stimulation,” 2011.

[90] D. K. Freeman, D. K. Eddington, J. F. Rizzo, and S. I. Fried, “Selective Activation of Neuronal Targets With Sinusoidal Electric Stimulation,” *J. Neurophysiol.*, 2010.

[91] R. H. Masland, “Cell populations of the retina: The proctor lecture,” *Investig. Ophthalmol. Vis. Sci.*, 2011.

[92] J. F. Fohlmeister and R. F. Miller, “Mechanisms by which cell geometry controls repetitive impulse firing in retinal ganglion cells.,” *J. Neurophysiol.*, 1997.

[93] M.-N. Delyfer *et al.*, “Adapted Surgical Procedure for Argus II Retinal Implantation: Feasibility, Safety, Efficiency, and Postoperative Anatomic Findings,” *Ophthalmol. Retin.*, 2018.

[94] G. J. Chader, J. Weiland, and M. S. Humayun, *Artificial vision: needs, functioning, and testing of a retinal electronic prosthesis*, vol. 175, no. 09. Elsevier, 2009.

[95] J. F. Rizzo, “Methods and Perceptual Thresholds for Short-Term Electrical Stimulation of Human Retina with Microelectrode Arrays,” *Invest. Ophthalmol. Vis. Sci.*, 2003.

[96] M. Keserü *et al.*, “Acute electrical stimulation of the human retina with an epiretinal electrode array,” *Acta Ophthalmol.*, 2012.

[97] A. K. Ahuja and M. R. Behrend, “The Argus™ II retinal prosthesis: Factors affecting patient selection for implantation,” *Progress in Retinal and Eye Research*. 2013.

[98] S. F. Cogan, “Neural stimulation and recording electrodes,” *Annual Review of Biomedical Engineering*. 2008.

[99] M. S. Humayun *et al.*, “Interim results from the international trial of second sight’s visual

prosthesis," *Ophthalmology*, 2012.

[100] S. I. Fried, "A Method for Generating Precise Temporal Patterns of Retinal Spiking Using Prosthetic Stimulation," *J. Neurophysiol.*, 2005.

[101] R. J. Jensen, O. R. Ziv, and J. F. Rizzo, "Thresholds for activation of rabbit retinal ganglion cells with relatively large, extracellular microelectrodes," *Investig. Ophthalmol. Vis. Sci.*, 2005.

[102] Y. H. L. Luo, J. J. Zhong, M. Clemo, and L. da Cruz, "Long-term Repeatability and Reproducibility of Phosphene Characteristics in Chronically Implanted Argus II Retinal Prosthesis Subjects," *Am. J. Ophthalmol.*, 2016.

[103] K. Loizos, R. Marc, M. Humayun, J. R. Anderson, B. W. Jones, and G. Lazzi, "Increasing electrical stimulation efficacy in degenerated retina: Stimulus waveform design in a multiscale computational model," *IEEE Trans. Neural Syst. Rehabil. Eng.*, 2018.

[104] T. M. O'Hearn, S. R. Sadda, J. D. Weiland, M. Maia, E. Margalit, and M. S. Humayun, "Electrical stimulation in normal and retinal degeneration (rd1) isolated mouse retina," *Vision Res.*, 2006.

[105] L. T. Xu, A. V. Rachitskaya, M. J. DeBenedictis, J. Bena, S. Morrison, and A. Yuan, "Correlation between Argus II array–retina distance and electrical thresholds of stimulation is improved by measuring the entire array," *Eur. J. Ophthalmol.*, 2021.

[106] M. Abramian, N. H. Lovell, J. W. Morley, G. J. Suaning, and S. Dokos, "Activation and inhibition of retinal ganglion cells in response to epiretinal electrical stimulation: A computational modelling study," *J. Neural Eng.*, 2015.

[107] Q. Lyu *et al.*, "A Three-Dimensional Microelectrode Array to Generate Virtual Electrodes for Epiretinal Prosthesis Based on a Modeling Study," *Int. J. Neural Syst.*, 2020.

[108] J. K. Mueller and W. M. Grill, "Model-based analysis of multiple electrode array stimulation for epiretinal visual prostheses," *J. Neural Eng.*, 2013.

[109] H. Kolb, N. Ralph, and F. Eduardo, "The Organization of the Retina and Visual System," *Webivcson*, 2019.

[110] M. J. Mayer and J. E. Dowling, "The Retina: An Approachable Part of the Brain," *Am. J. Psychol.*, 1988.

[111] D. Tsai, J. W. Morley, G. J. Suaning, and N. H. Lovell, "Direct Activation and Temporal Response Properties of Rabbit Retinal Ganglion Cells Following Subretinal Stimulation," *J. Neurophysiol.*, 2009.

[112] C. Sekirnjak, P. Hottowy, A. Sher, W. Dabrowski, A. M. Litke, and E. J. Chichilnisky, "High-Resolution Electrical Stimulation of Primate Retina for Epiretinal Implant Design," *J. Neurosci.*, vol. 28, no. 17, pp. 4446–4456, 2008.

[113] C. Sekirnjak *et al.*, "Loss of responses to visual but not electrical stimulation in ganglion cells of rats with severe photoreceptor degeneration," *J. Neurophysiol.*, 2009.

[114] A. Van Wart, J. S. Trimmer, and G. Matthews, "Polarized distribution of ion channels within microdomains of the axon initial segment," *J. Comp. Neurol.*, 2007.

[115] P. Werginz, S. I. Fried, and F. Rattay, "Influence of the sodium channel band on retinal

ganglion cell excitation during electric stimulation - A modeling study," *Neuroscience*, 2014.

[116] S. I. Fried, A. C. W. Lasker, N. J. Desai, D. K. Eddington, and J. F. Rizzo, "Axonal sodium-channel bands shape the response to electric stimulation in retinal ganglion cells," *J. Neurophysiol.*, 2009.

[117] D. K. Freeman, J. F. Rizzo, and S. I. Fried, "Encoding visual information in retinal ganglion cells with prosthetic stimulation," *J. Neural Eng.*, 2011.

[118] R. J. Jensen and J. F. Rizzo, "Activation of retinal ganglion cells in wild-type and rd1 mice through electrical stimulation of the retinal neural network," *Vision Res.*, 2008.

[119] S. W. Lee, D. K. Eddington, and S. I. Fried, "Responses to pulsatile subretinal electric stimulation: Effects of amplitude and duration," *J. Neurophysiol.*, 2013.

[120] R. O. L. Wong, "Calcium imaging and multielectrode recordings of global patterns of activity in the developing nervous system," *Histochem. J.*, 1998.

[121] D. Smetters, A. Majewska, and R. Yuste, "Detecting action potentials in neuronal populations with calcium imaging," *Methods A Companion to Methods Enzymol.*, 1999.

[122] L. L. Looger and O. Griesbeck, "Genetically encoded neural activity indicators," *Current Opinion in Neurobiology*. 2012.

[123] C. Lohmann, K. L. Myhr, and R. O. L. Wong, "Transmitter-evoked local calcium release stabilizes developing dendrites," *Nature*, 2002.

[124] A. Miyawaki *et al.*, "Fluorescent indicators for Ca2+ based on green fluorescent proteins and calmodulin," *Nature*, 1997.

[125] A. Takahashi, P. Camacho, J. D. Lechleiter, and B. Herman, "Measurement of intracellular calcium," *Physiological Reviews*. 1999.

[126] M. Mank and O. Griesbeck, "Genetically encoded calcium indicators," *Chemical Reviews*. 2008.

[127] J. Nakai, M. Ohkura, and K. Imoto, "A high signal-to-noise ca2+ probe composed of a single green fluorescent protein," *Nat. Biotechnol.*, 2001.

[128] T. W. Chen *et al.*, "Ultrasensitive fluorescent proteins for imaging neuronal activity," *Nature*, 2013.

[129] H. Dana, Y. Sun, B. Mohar, B. Hulse, and J. P. Hasseman, "High-performance GFP-based calcium indicators for imaging activity in neuronal populations and microcompartments," *bioRxiv*, 2018.

[130] S. D. Patil, D. G. Rhodes, and D. J. Burgess, "DNA-based therapeutics and DNA delivery systems: A comprehensive review," *AAPS Journal*. 2005.

[131] M. Dezawa, M. Takano, H. Negishi, X. Mo, T. Oshitari, and H. Sawada, "Gene transfer into retinal ganglion cells by in vivo electroporation: A new approach," *Micron*, 2002.

[132] C. Garcia-Frigola, M. I. Carreres, C. Vegar, and E. Herrera, "Gene delivery into mouse retinal ganglion cells by in utero electroporation," *BMC Dev. Biol.*, 2007.

[133] H. A. Zariwala *et al.*, "A Cre-dependent GCaMP3 reporter mouse for neuronal imaging in

vivo," *J. Neurosci.,* 2012.

[134] G. Feng *et al.*, "Imaging neuronal subsets in transgenic mice expressing multiple spectral variants of GFP," *Neuron,* 2000.

[135] B. G. Borghuis *et al.*, "Imaging light responses of targeted neuron populations in the rodent retina," *J. Neurosci.,* 2011.

[136] M. Hellström *et al.*, "Cellular tropism and transduction properties of seven adeno-associated viral vector serotypes in adult retina after intravitreal injection," *Gene Ther.,* 2009.

[137] D. Grimm and M. Kay, "From Virus Evolution to Vector Revolution: Use of Naturally Occurring Serotypes of Adeno-associated Virus (AAV) as Novel Vectors for Human Gene Therapy," *Curr. Gene Ther.,* 2005.

[138] S. Daya and K. I. Berns, "Gene therapy using adeno-associated virus vectors," *Clinical Microbiology Reviews*. 2008.

[139] A. C. Weitz *et al.*, "Imaging the response of the retina to electrical stimulation with genetically encoded calcium indicators," *J. Neurophysiol.,* 2013.

[140] Y. C. Chang, D. H. Ghaffari, R. H. Chow, and J. D. Weiland, "Stimulation strategies for selective activation of retinal ganglion cell soma and threshold reduction," *J. Neural Eng.,* vol. 16, no. 2, p. 026017, 2019.

[141] D. K. Freeman, J. S. Jeng, S. K. Kelly, E. Hartveit, and S. I. Fried, "Calcium channel dynamics limit synaptic release in response to prosthetic stimulation with sinusoidal waveforms," in *Journal of Neural Engineering,* 2011.

[142] A. P. Fornos *et al.*, "Temporal properties of visual perception on electrical stimulation of the retina," *Investig. Ophthalmol. Vis. Sci.,* 2012.

[143] S. I. Fried, H. A. Hsueh, and F. S. Werblin, "A method for generating precise temporal patterns of retinal spiking using prosthetic stimulation," *J. Neurophysiol.,* 2006.

[144] E. Margalit and W. B. Thoreson, "Inner retinal mechanisms engaged by retinal electrical stimulation," *Investig. Ophthalmol. Vis. Sci.,* 2006.

[145] T. Guo *et al.*, "Understanding the retina: A review of computational models of the retina from the single cell to the network level," *Crit. Rev. Biomed. Eng.,* 2014.

[146] S. Usui, A. Ishihara, Y. Kamiyama, and H. Ishii, "Ionic current model of bipolar cells in the lower vertebrate retina," *Vision Res.,* 1996.

[147] J. F. Fohlmeister and R. F. Miller, "Impulse encoding mechanisms of ganglion cells in the tiger salamander retina," *J. Neurophysiol.,* 1997.

[148] Y. Kamiyama, T. Ogura, and S. Usui, "Ionic current model of the vertebrate rod photoreceptor," *Vision Res.,* 1996.

[149] T. Aoyama, Y. Kamiyama, and S. Usui, "Simulation analysis of receptive-field size of retinal horizontal cells by ionic current model," *Vis. Neurosci.,* 2005.

[150] J. F. Fohlmeister, P. A. Coleman, and R. F. Miller, "Modeling the repetitive firing of retinal ganglion cells," *Brain Res.,* 1990.

[151] J. F. Fohlmeister, “A nerve model of greatly increased energy-efficiency and encoding flexibility over the Hodgkin-Huxley model,” *Brain Res.*, 2009.

[152] P. L. Carras, P. A. Coleman, and R. F. Miller, “Site of action potential initiation in amphibian retinal ganglion cells,” *J. Neurophysiol.*, 1992.

[153] M. A. Schiefer and W. M. Grill, “Sites of neuronal excitation by epiretinal electrical stimulation,” *IEEE Trans. Neural Syst. Rehabil. Eng.*, 2006.

[154] T. Flores, G. Goetz, X. Lei, and D. Palanker, “Optimization of return electrodes in neurostimulating arrays,” *J. Neural Eng.*, 2016.

[155] M. I. Maturana *et al.*, “A Simple and Accurate Model to Predict Responses to Multi-electrode Stimulation in the Retina,” *PLoS Comput. Biol.*, 2016.

[156] M. Beyeler, G. Boynton, I. Fine, and A. Rokem, “pulse2percept: A Python-based simulation framework for bionic vision,” 2017.

[157] J. R. Golden *et al.*, “Simulation of visual perception and learning with a retinal prosthesis,” *J. Neural Eng.*, 2019.

[158] C. Sekirnjak, P. Hottowy, A. Sher, W. Dabrowski, a M. Litke, and E. J. Chichilnisky, “Electrical stimulation of mammalian retinal ganglion cells with multielectrode arrays.,” *J. Neurophysiol.*, 2006.

[159] D. Palanker *et al.*, “Migration of retinal cells through a perforated membrane: Implications for a high-resolution prosthesis,” *Investig. Ophthalmol. Vis. Sci.*, vol. 45, no. 9, pp. 3266–3270, 2004.

[160] A. Horsager, G. M. Boynton, R. J. Greenberg, and I. Fine, “Temporal interactions during paired-electrode stimulation in two retinal prosthesis subjects,” *Investig. Ophthalmol. Vis. Sci.*, 2011.

[161] L. H. Jepson *et al.*, “Spatially Patterned Electrical Stimulation to Enhance Resolution of Retinal Prostheses,” *J. Neurosci.*, vol. 34, no. 14, pp. 4871–4881, 2014.

[162] M. N. Shivdasani *et al.*, “Factors affecting perceptual thresholds in a suprachoroidal retinal prosthesis,” *Investig. Ophthalmol. Vis. Sci.*, 2014.

[163] G. D. Field and E. J. Chichilnisky, “Information Processing in the Primate Retina: Circuitry and Coding,” *Annu. Rev. Neurosci.*, 2007.

[164] R. H. Masland, “Neuronal diversity in the retina,” *Current Opinion in Neurobiology*. 2001.

[165] W. Truccolo, L. R. Hochberg, and J. P. Donoghue, “Collective dynamics in human and monkey sensorimotor cortex: predicting single neuron spikes,” *Nat. Neurosci.*, 2009.

[166] J. W. Pillow *et al.*, “Spatio-temporal correlations and visual signalling in a complete neuronal population,” *Nature*, 2008.

[167] T. Guo *et al.*, “Closed-loop efficient searching of optimal electrical stimulation parameters for preferential excitation of retinal ganglion cells,” *Front. Neurosci.*, 2018.

[168] A. K. Ahuja, M. R. Behrend, M. Kuroda, M. S. Humayun, and J. D. Weiland, “An in vitro model of a retinal prosthesis,” *IEEE Trans. Biomed. Eng.*, 2008.

[169] R. D. Jager, W. F. Mieler, and J. W. Miller, “Age-related macular degeneration,” *New England Journal of Medicine*. 2008.

[170] D. T. Hartong, E. L. Berson, and T. P. Dryja, “Retinitis pigmentosa,” *Lancet*. 2006.

[171] J. D. Weiland and M. S. Humayun, “Artificial vision by electrical stimulation of the retina,” in *Proceedings of the International Joint Conference on Neural Networks*, 2005.

[172] A. C. Weitz *et al.*, “Interphase gap as a means to reduce electrical stimulation thresholds for epiretinal prostheses,” *J. Neural Eng.*, 2014.

[173] M. L. Hines and N. T. Carnevale, “The NEURON Simulation Environment,” *Neural Computation*. 1997.

[174] R. N. Weinreb, A. W. Dreher, A. Coleman, H. Quigley, B. Shaw, and K. Reiter, “Histopathologic Validation of Fourier-Ellipsometry Measurements of Retinal Nerve Fiber Layer Thickness,” *Arch. Ophthalmol.*, vol. 108, no. 4, pp. 557–560, 1990.

[175] H. Heynen and D. Van Norren, “Origin of the electroretinogram in the intact macaque eye-II. Current source-density analysis,” *Vision Res.*, 1985.

[176] R. Plonsey and R. C. Barr, *Bioelectricity: A quantitative approach*. 2007.

[177] P. Lukasiewicz and F. Werblin, “A slowly inactivating potassium current truncates spike activity in ganglion cells the tiger salamander retina,” *J. Neurosci.*, vol. 8, no. 12, pp. 4470–4481, 1988.

[178] S. A. Lipton and D. L. Tauck, “Voltage-dependent conductances of solitary ganglion cells dissociated from the rat retina.,” *J. Physiol.*, 1987.

[179] K. N. Ahn *et al.*, “Effect of stimulus waveform of biphasic current pulse on retinal ganglion cell responses in retinal degeneration (rd1) mice,” *Korean J. Physiol. Pharmacol.*, 2015.

[180] R. K. Shepherd and E. Javel, “Electrical stimulation of the auditory nerve: II. Effect of stimulus waveshape on single fibre response properties,” *Hear. Res.*, vol. 130, no. 1–2, pp. 171–188, 1999.

[181] C. M. McKay and K. R. Henshall, “The perceptual effects of interphase gap duration in cochlear implant stimulation,” *Hear. Res.*, 2003.

[182] R. J. Greenberg, T. J. Velte, M. S. Humayun, G. N. Scarlatis, and E. de Juan, “A computational model of electrical stimulation of the retinal ganglion cell. TL - 46,” *IEEE Trans. Biomed. Eng.*, 1999.

[183] J. Paknahad, P. Kosta, J.-M. C. Bouteiller, M. S. Humayun, and G. Lazzi, “The Sensitivity of Retinal Bipolar Cells Response to Long Stimulus Pulse Durations in Epiretinal Prostheses,” *ARVO Meet. Abstr.*, vol. 62, 2021.

[184] T. B. Esler, M. I. Maturana, R. R. Kerr, D. B. Grayden, A. N. Burkitt, and H. Meffin, “Biophysical basis of the linear electrical receptive fields of retinal ganglion cells,” *J. Neural Eng.*, 2018.

[185] P. Werginz, H. Benav, E. Zrenner, and F. Rattay, “Modeling the response of ON and OFF retinal bipolar cells during electric stimulation,” *Vision Res.*, 2015.

[186] E. J. Chichilnisky and R. S. Kalmar, “Functional Asymmetries in ON and OFF Ganglion Cells of Primate Retina,” *J. Neurosci.,* 2002.

[187] H. Kasi, W. Hasenkamp, G. Cosendai, A. Bertsch, and P. Renaud, “Simulation of epiretinal prostheses - Evaluation of geometrical factors affecting stimulation thresholds,” *J. Neuroeng. Rehabil.,* 2011.

[188] D. Haji Ghaffari *et al.*, “The effect of waveform asymmetry on perception with epiretinal prostheses,” *J. Neural Eng.*, 2020.

[189] R. H. Byrd, M. E. Hribar, and J. Nocedal, “An interior point algorithm for large-scale nonlinear programming,” *SIAM J. Optim.*, 1999.

[190] R. A. Waltz, J. L. Morales, J. Nocedal, and D. Orban, “An interior algorithm for nonlinear optimization that combines line search and trust region steps,” *Math. Program.,* 2006.

[191] Thomas Z. Lauritzen, D. Nanduri, J. Weiland, J. D. Dorn, K. McClure, and R. Greenberg;, “Inter-electrode Discriminability Correlates With Spatial Visual Performance In ArgusTM II Subjects,” *IOVS*, vol. 52, no. 14, p. 4927, 2011.

[192] I. D. Bogdan, T. van Laar, D. L. M. Oterdoom, G. Drost, J. M. C. van Dijk, and M. Beudel, “Optimal Parameters of Deep Brain Stimulation in Essential Tremor: A Meta-Analysis and Novel Programming Strategy,” *J. Clin. Med.,* 2020.

[193] A. Auricchio *et al.*, “Exchange of surface proteins impacts on viral vector cellular specificity and transduction characteristics: The retina as a model,” *Hum. Mol. Genet.*, 2001.

[194] K. R. G. Martin, R. L. Klein, and H. A. Quigley, “Gene delivery to the eye using adeno-associated viral vectors,” *Methods,* 2002.

[195] D. Haji Ghaffari, Y.-C. Chang, E. Mirzakhalili, and J. D. Weiland, “Closed-loop Optimization of Retinal Ganglion Cell Responses to Epiretinal Stimulation: A Computational Study,” *NER*, 2021.

[196] D. P. Kingma and J. L. Ba, “Adam: A method for stochastic optimization,” in *3rd International Conference on Learning Representations, ICLR 2015 - Conference Track Proceedings*, 2015.

[197] Y. Lu *et al.*, “Optimization of stimulation parameters for epi-retinal implant based on biosafety consideration,” *PLoS One,* 2020.

[198] A. E. Hadjinicolaou *et al.*, “Optimizing the Electrical Stimulation of Retinal Ganglion Cells,” *IEEE Trans. Neural Syst. Rehabil. Eng.,* 2015.

[199] Y. LeCun, L. Bottou, Y. Bengio, and P. Haffner, “Gradient-based learning applied to document recognition,” *Proc. IEEE,* 1998.

[200] A. Krizhevsky, I. Sutskever, and G. E. Hinton, “ImageNet classification with deep convolutional neural networks,” *Commun. ACM*, 2017.

[201] A. Wongsarnpigoon and W. M. Grill, “Genetic algorithm reveals energy-efficient waveforms for neural stimulation,” in *Proceedings of the 31st Annual International Conference of the IEEE Engineering in Medicine and Biology Society: Engineering the Future of Biomedicine, EMBC 2009*, 2009.

[202] E. Peña, S. Zhang, S. Deyo, Y. Xiao, and M. D. Johnson, “Particle swarm optimization for programming deep brain stimulation arrays,” *J. Neural Eng.*, 2017.

[203] A. Cho, C. Ratliff, A. Sampath, and J. Weiland, “Changes in ganglion cell physiology during retinal degeneration influence excitability by prosthetic electrodes,” *J. Neural Eng.*, vol. 13, no. 2, 2016.

[204] K. E. Finn, H. J. Zander, R. D. Graham, S. F. Lempka, and J. D. Weiland, “A Patient-Specific Computational Framework for the Argus II Implant,” *IEEE Open J. Eng. Med. Biol.*, 2020.

[205] V. Sarthy, H. Hoshi, S. Mills, and V. J. Dudley, “Characterization of green fluorescent protein-expressing retinal cells in CD 44-transgenic mice,” *Neuroscience*, 2007.

[206] M. I. Seider and P. Hahn, “Argus II retinal prosthesis malrotation and repositioning with intraoperative optical coherence tomography in a posterior staphyloma,” *Clinical Ophthalmology*. 2015.

[207] A. Gonzalez-Calle and J. D. Weiland, “Evaluation of effects of electrical stimulation in the retina with optical coherence tomography,” in *Proceedings of the Annual International Conference of the IEEE Engineering in Medicine and Biology Society, EMBS*, 2016.

[208] E. Cohen, A. Agrawal, M. Connors, B. Hansen, H. Charkhkar, and J. Pfefer, “Optical coherence tomography imaging of retinal damage in real time under a stimulus electrode,” *J. Neural Eng.*, 2011.

[209] L. Colodetti *et al.*, “Pathology of damaging electrical stimulation in the retina,” *Exp. Eye Res.*, 2007.

[210] Z. Qin *et al.*, “Adaptive optics two-photon microscopy enables near-diffraction-limited and functional retinal imaging in vivo,” *Light Sci. Appl.*, 2020.

[211] A. S. Bar-Noam, N. Farah, and S. Shoham, “Correction-free remotely scanned two-photon in vivo mouse retinal imaging,” *Light Sci. Appl.*, 2016.